Tomographic Phase Reconstruction using a Tilted Laue Analyser Crystal

By Mitchell Chalmers

Supervisors: Dr K.M Pavlov & Dr M.J Kitchen

Submitted in partial fulfillment of the requirements for the degree of Masters of Science in Medical Physics

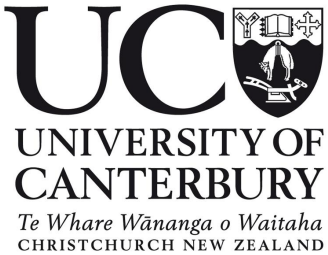

Te Whare Wananga O Waitaha, University of Canterbury
1st March 2020

Chapter 1

Abstract

Analyser-Based Phase Contrast Imaging (ABPCI) is a promising phase contrast method due to its high image resolution of soft tissues and high signal to noise ratio with its biggest downside being the experimental setup complexity. One of the main drawbacks of ABPCI is that its two-dimensional (2-D) images only provide 1-D phase sensitivity [1]. The aim of the work is to apply the methodology of inclined geometry proposed by Rutishauser et al [2] to ABPCI to significantly improve the image quality of the reconstructed ABPCI images for quantitative analysis.

We employed a Laue analyser crystal to perform analyser-based based phase contrast imaging and took tomographic datasets over 360° of rotation similar to [3] with the detector and sample tilted by 8° clockwise following the propagation direction of the x-ray wavefield. We measured the refractive coefficient δ to be approximately a factor of 2 off the reference values with the β values in agreement for media in the perspex phantom. This is probably due to underestimation of the phase gradients due to the application of the geometric optics approximation and misalignment of the transmitted and diffracted projections as well as the $\Delta\theta$ and $\Delta\theta_{180}$ maps. These errors are then integrated which amplifies the low frequency noise.

Acknowledgements

I would like to thank my supervisors Dr Konstantin M. Pavlov and Dr Marcus J. Kitchen, for their patience, support and extensive assistance throughout this theiss. Both of them helped me immensely by concisively explaining the theory, code and what to do next over the period of this thesis. Special thanks to Dr Marcus J. Kitchen for allowing me to use and adapt his code for this thesis and to Dr Konstantin M. Pavlov for deriving, helping me understand and implement the inclined geometry methodology from grating interferometry to ABPCI.

Extended thanks goes out to, M.J. Kitchen, K. Uesugi, D.M. Paganin, T.E. Gureyev, I.M. Young, G. Falzon, P. Quin, K.M. Pavlov who were the team involved in acquiring the data used in this thesis.
The synchrotron radiation experiments were performed at beamline BL20B2 of SPring-8 with the approval of the Japan Synchrotron Radiation Research Institute (JASRI) (Proposal 2012B1315)
We acknowledge travel funding provided by the International Synchrotron Access Program (ISAP) managed by the Australian Synchrotron, part of ANSTO (AS/IA124/6149).

I would also like to thank my parents for both supporting me and encouraging me throughout this thesis.

Contents

List of Figures

List of Tables

Chapter 2

Introduction

In this chapter we will discuss the motivation behind this thesis before discussing the fundamental properties of x-rays and their production from laboratory and synchrotron sources. We will also discuss properties of image quality as there will be alot of images presented in this paper. After this we will derive the fundamental wave equations with assumptions that extract phase contrast information. Followed by introducing the properties and theory behind Phase Contrast Imaging (PCI), while comparing it to conventional radiography. Then finally discussing the methods of phase contrast imaging focusing on ABPCI and grating interferometry.

2.1 Motivation

Phase contrast x-ray imaging provides superior soft tissue contrast compared to traditional absorption-based radiography especially, in the high energy regimes [11]. This has the potential to enable greater image quality with less radiation dose delivered to the patient in a clinical setting [9]. ABI is a promising phase contrast imaging technique that utilizes the Bragg condition for an analyser crystal. The analyser crystal is highly sensitive to phase gradients along the vertical axis. This means it can pick up small refractive discrepancies with high image resolution and signal to noise ratio. ABPCI's major downfalls are its complex experimental setup that requires multiple components that have to be precisely aligned in order to generate phase contrast images [19]. Furthermore, ABI is only sensitive to phase changes in the vertical direction meaning it has 1-D phase sensitivity [1]. This problem also exists in other phase contrast methods such as grating interferometry [20]. For that technique, Rutishauser [2] developed a method to overcome the problem by utilizing an inclined geometry for the two 1-D gratings to pro-

duce a 2-D phase gradient. The aim of the work is to apply the methodology of inclined geometry proposal in [2] to ABI to significantly improve the image quality of the reconstructed ABI images for quantitative analysis. We do this by rotating the detector and sample by 8° clockwise following the x-ray wavefield, while using Laue geometry. Laue geometry allows two images diffracted and transmitted to be gathered for each projection giving us a method to calculate the intensity contrast using either the transmitted or diffracted images and the phase contrast using the ratio of diffracted over transmitted. We take a projection and its respective 180° projection then flip the 180° projection and align the two projections so they precisely overlap. From this we now have two images with 1-D phase information in perpendicular directions that can be integrated (discussed in Section 2.4) to give a quantitative 2-D phase map (discussed in Chapter 5) and perform 180° tomographic reconstruction (discussed in Chapter 3) to obtain δ and β maps (discussed in Section 5.3).

2.2 X-ray Sources

Electromagnetic waves such as x-rays are resultant from the radiative loss during the change in velocity of charge carriers such as electrons [21]. Conventional x-ray sources achieve this by bombarding an anode, a material of high atomic number commonly tungsten, with an accelerated beam of electrons generated by thermionic emission [22]. These electrons can interact with the target in two ways (1) Incident electron interaction with an orbital electron of a target atom resulting mainly in a collision impact loss and ionization of the target due to the photoelectric effect. This is then followed the by emission of characteristic x-rays and/or Auger electrons. Auger electrons are orbital electrons that absorb the energy emitted as a characteristic x-ray and are ejected from the atom [23]. (2) Radiative collision Coulomb interaction between the incident electron and nucleus as the negative electron's trajectory bends towards the positive nucleus causing energy and momentum to be lost in the form of a photon. The probability of this interaction increases with electron energy E and atomic number squared Z^2. Conventional X-ray source issues are the heating of the anode causing a drift in the Bremsstrahlung spectrum over the exposure time, additionally the anode could crack under the prolonged high thermal flux. This would require the anode to be replaced. However, this issue can be fixed by rotating and applying a coolant to the anode, which distributes the thermal flux over a larger surface area of the anode and maintains acceptable anode temperature, respectively. One other major downfall with a conventional x-ray source

is the Heel effect shown in Figure 2.1, which is dependent on the anode angle.

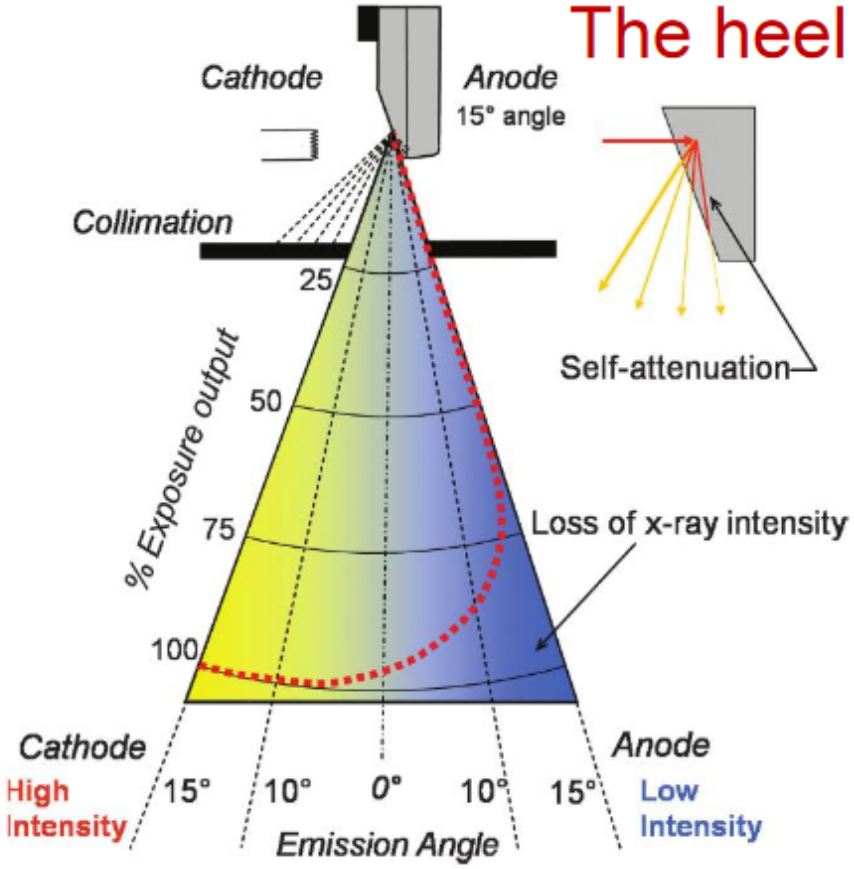

Figure 2.1: The Heel effect is a result of the electron wavefield propagating through the surface of the anode undergoing electron-atom interactions primarily the photoelectric effect and Bremsstrahlung radiation. The resultant characteristic and x-ray spectrum is self attenuated by the anode. The magnitude of the effect depends on how far it must propagate through the anode. This causes the intensity to decrease as moving closer to the anode along the horizontal axis. This uneven intensity distribution of the x-ray spectrum can cause significant issues when imaging a sample. this effect could be reduced by increasing the anode angle or compensated for by filtering the x-ray spectrum. The Heel effect could also be utilized to image a sample whose thickness is small on one side and large on the other (such as the breast) as the thin side will absorb less photons than the thicker. This effect is fixed in some modern conventional x-ray sources. Adapted from [4].

Synchrotrons are another source of x-rays, where a continuous source of electrons are accelerated using a linear accelerator before being injected into a booster ring. This further accelerates the electrons to the energy of electrons already present in this main storage ring through the use of an array of magnets [24]. As the electrons are deflected through the magnetic field, they produce magnetobremsstrahlung radiation commonly reffered to as synchrotron radiation due to their changing velocity [25]. The synchrotron radiation is channeled down beamlines present tangentially around the main ring to experimental workstations [24]. In Phase Contrast imaging (PCI) the coherence of an x-ray wavefield is a crucial property of the x-ray effect as the phase effects are blurred if incident x-rays are not monochromatic. The coherence of an x-ray beam is described in two parts; temporal coherence describes how monochromatic the wavefield produced by the source is. Spatial coherence is a measure of the correlation between the phases of a light wavefield at different points transverse to the direction of propagation, which tells us how uniform the phase of the wavefront is [26]. Synchrotrons can produce x-ray wavefields with much higher spatial and temporal coherence (using monochromators) and intensity [10] [27] than laboratory x-ray sources.

However, both these x-ray sources, namely x-ray tubes and synchrotrons produce polychromatic x-ray wavefields that are generally unsuitable for most PCI methods including our ABPCI method. This is because PCI relies on the diffraction of the x-ray wavefield, which produces distinct patterns in the image. However, polychromatic x-ray wavefields cause these patterns to interfere with each other causing blurring rendering the phase patterns indistinguishable. We can generate a monochromatic x-ray wavefield by filtering the polychromatic x-ray wavefield with a monochromator (as shown in Figure 2.2) consisting of two Si(1 1 1) crystals. We can set an output monochromatic x-ray energy by changing the incidence angle θ_1 following the Bragg law, Eqn (2.48) to obtain a wavelength λ. This will give us the desired energy E of the resultant wavefield from the relation below [28]

$$E = \frac{hc}{\lambda}, \tag{2.1}$$

where c is the speed of light in a vacuum and h is Planck's constant. Following Figure 2.2 and beginning with 1, we have the polychromatic x-ray wavefield that is incident on a slit 2. Parts of the x-ray wavefield are either absorbed by the slit or pass through the gap depending on their direction of propagation 3. X-ray wavefields that pass through the slit are then incident on the first Si(1 1 1) crystal 4 before being diffracted following the Bragg law Eqn (2.48) and incident on the second Si(1 1 1) crystal 5. The resultant beam

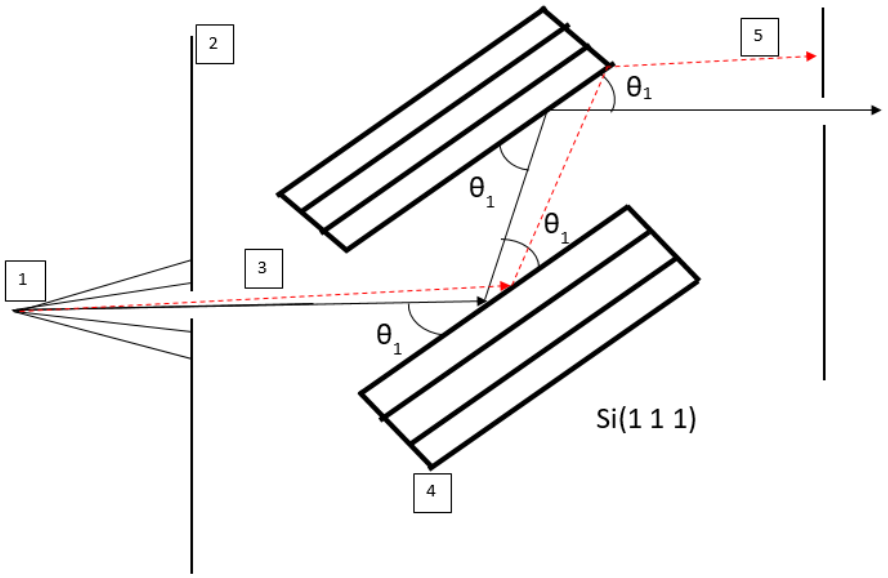

Figure 2.2: Schematic of monochromator setup used to filter the polychromatic x-ray wavefield into a monochromatic x-ray wavefield whose energy we can set by changing the incidence angle θ_1 following the Bragg law Eqn (2.48). Beginning with 1 we have the polychromatic x-ray wavefield, which is incident on a slit 2. Parts of the x-ray wavefield are either absorbed by the slit or pass through the gap depending on their direction of propagation. 3. X-ray wavefields that pass through the slit are then incident on the first Si(1 1 1) crystal 4. before being diffracted following the Bragg law, Eqn (2.48) and incident on the second Si(1 1 1) crystal 5. The resultant beam is then incident upon another slit. This is designed so that only wavefields such as the black arrow that are incident upon the crystal at angle θ_1 pass through while other beams such as the red line are absorbed by the slit [5].

is then incident upon another slit. This is designed so that only wavefields such as the black arrow that are incident upon the crystal at an angle θ_1 pass through. Other beams such as the red line are absorbed by the slit [5].
The monochromator works in the following two separate RCs produced by the bottom and top Si(1 1 1) crystals in Figure 2.2 (red and blue Rocking Curve (RC) respectively shown in Figure 2.3) following the Bragg law Eqn (2.48). The multiplication of these two RCs produces the observed purple RC in Figure 2.4. This is the resultant rocking curve, which is broader and smaller than the rocking curves of each crystal.

The major downside to applying a monochromator is the major loss of wave-

Figure 2.3: Two separate Rocking Curves (RCs) produced by the bottom and top Si(1 1 1) crystals in Figure 2.2 (red and blue RC respectively) following the Bragg law, Eqn (2.48). The RC's are separated due to a slight misalignment between the two crystals. However, through rotating the top crystal about the plane so that it is in the position shown in Figure 2.2. The blue RC is shifted to the left so that it significantly overlaps with the red RC.

field intensity due to the strict filtering conditions of the monochromator. This problem can be fixed by applying a longer exposure time however, longer exposure time may cause motion artefacts.

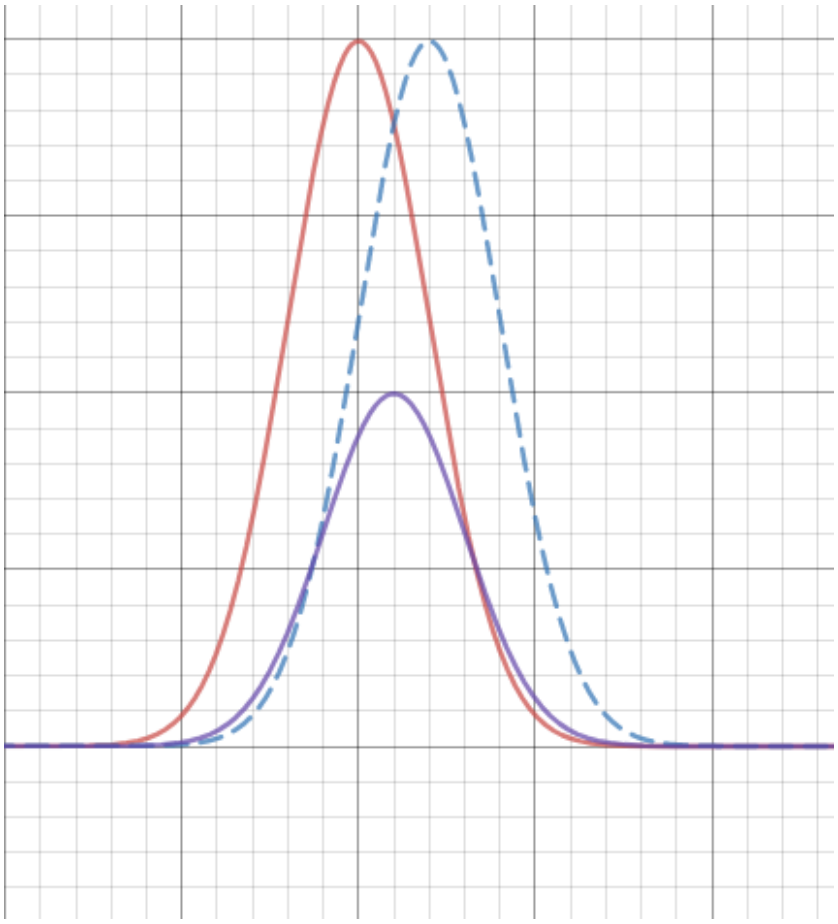

Figure 2.4: Two overlapping RC's produced by the two Si (1 1 1) crystals, from multiplication of these two rocking curves produces the observed purple rocking curve. This is the resultant rocking curve, which is broader and smaller than the rocking curves of each crystal.

2.3 Image Properties

This section discusses the basic properties of images as there will be a number of images presented in this thesis, of which we will analyse them qualitatively and quantitatively. Qualitative analysis focuses on how the image looks i.e. does it look as expected, is there good contrast in the image, are the boundaries well defined and is the image of high resolution. Quantitative analysis focuses on the values of the data in the image. Contrast in images manifests from the difference in grayscale values among pixels in the image [4]

and can be expressed as

$$Contrast = \frac{I_{max} - I_{min}}{I_{max} + I_{min}}, \tag{2.2}$$

where I_{max} and I_{min} are the maximum and minimum intensity detected by the detector. This means that in an image with high contrast there are sharp transitions between light (high grayscale) and dark (low grayscale) gray, while a uniformly gray image has no contrast. For phase contrast and CT imaging we are concerned with spatial resolution. Spatial resolution refers to the ability to see small details in the imaged samples. Hence, an imaging system that has a higher spatial resolution will be able to detect and reproduce the presence of smaller objects in the image [4]. These parameters of an image such as resolution are influenced by the parameters of the wavefield e.g. monochromaticity. Two wavefields are perfectly coherent if they possess constant phase difference with identical frequency and waveform [29].

We now need to discuss the effects that degrade image quality in the form of unsharpness, blurring and noise. These effects partially result from the specifications and setup of the detector used to gather data. Geometric blur/unsharpness for an laboratory x-ray source is given by the equation

$$\frac{f_1}{SOD} = \frac{f_2}{ODD}, \tag{2.3}$$

and is seen in the images as edges appearing ill defined (unsharp/blurred). Where f_1 and f_2 are the focal spot size of the source and its projection at the detector respectively and SOD and ODD are defined as the source to object distance and the object to detector distance. Focal spot - area on target surface that receives the beam of electrons as seen by the observer.

Noise are external signals that cause random variation of brightness in images causing contrast resolution to decrease. Some sources of noise are grain noise - darkening of grains randomly with a random distribution, electronic noise - detector current always on, which can produce readings in the pixels, structured noise - most pixelated detectors have a number of parallel channels for reading out the array of detector elements and this reduces readout time. Each channel uses its own amplifier circuits and these circuits cannot be perfectly tuned with respect to each other. As a result, groups of detector elements that are read out may have different offset noise and gain characteristics, and these cause structured or fixed pattern noise in digital detector systems. The key to correcting for structured noise is utilizing that it is spatially constant for a period of time. Anatomical noise - is the pattern

on the image that is generated by patient anatomy that is always present but not important for the diagnosis. Noise also highly depends on photon statistics of the imaging setup this is commonly based on the Signal-to-Noise Ratio (SNR) as the chance of a given photon striking a particular detector is given by Poisson statistics.

$$SNR = m/\sqrt{m} = \sqrt{m}, \tag{2.4}$$

Where m is the mean number of counts in each pixel in the detector. Most of these effects that degrade image quality can be fixed by increasing exposure time as well as changing some properties of the detector such as the; Bit depth - larger sets of data for each pixel i.e 1 bit/pixel, 2 bit/pixel etc, which will improve photon statistics and reduce noise caused from low pixel counts. Pixel size can be increased, bigger pixels means less pixels in the detector, which means less spatial resolution but more photons counted in each pixel. This results in better efficiency, better photon statistics and less exposure time required. Number of pixels can be increased as well, more pixels of smaller size present a better image but this requires longer scans and image reconstruction time, and larger image storage size. This is typically used for large Field Of View (FOV) images to insure sufficient spatial resolution and contrast is present in the image. Minimising exposure time is crucial as this reduces the dose delivered to the patient. The incident x-ray energy also matters as low energy photons are more easily absorbed and thus less are detected in the detector than higher energy photons.

2.4 2-D Integration

The purpose of this thesis is to apply the inclined geometry proposed by Rutishauser et al. [2] to ABPCI in order to have 2-D phase sensitivity and obtain a 2-D phase gradient. This phase gradient will need to be integrated in our case using a 2-D Fourier integration method proposed by [30]. After phase retrieval is performed, we have components of the phase gradients in the horizontal and vertical direction denoted by g_h and g_v, respectively. We can defined these as the complex field $h(x, y)$ as follows

$$h(x,y) = g_h(x,y) + ig_v(x,y) = \frac{\partial G_h}{\partial x}(x,y) + i\frac{\partial G_v}{\partial y}(x,y), \tag{2.5}$$

where in this case the spatial coordinates (x, y) are the horizontal and vertical axis, respectively. From this we can apply the 2-D Fourier transform [31] to

this to obtain the equation below using the Fourier derivative theorem [31].

$$\mathcal{F}[h(x,y)](k,l) = \iint_{-\infty}^{\infty} h(x,y)\cdot e^{-2\pi i(kx+ly)}dxdy = 2\pi i(k+il)\cdot\mathcal{F}[G(x,y)](k,l). \tag{2.6}$$

Where (k,l) are the reciprocal (Fourier) space coordinates of spatial coordinates (x,y) and $\mathcal{F}$ is the Fourier transform [32]. From this we can apply the inverse Fourier transform $\mathcal{F}^{-1}$ [32] to Eqn (2.6) to obtain

$$G(x,y) = \mathcal{F}^{-1}\left[\frac{\mathcal{F}[g_h + ig_v](k,l)}{2\pi i(k+il)}\right](x,y), \tag{2.7}$$

where $G(x,y)$ is the desired phase map.

2.5 Wave Equations

The propagation of scalar wavefields is the basic tool of electromagnetic theory that will be utilized to describe the fundamentals and foundation of x-ray phase contrast imaging. This section will follow through the derivation of the principles of phase contrast imaging and the underlying key assumptions applied.

2.5.1 Wavefunction and the Helmholtz equation

In this section we will discuss the optical formalism of a propagating wave and incorporate the paraxial field approximation, which is commonly applied to simplify the explanation of x-ray wavefield propagation. First we begin with a scalar wavefield function of the form $\Psi(x,y,z,t)$ with three spatial coordinates for each spatial dimension given by x, y and z respectively, and time t. $\Psi(x,y,z,t)$ is set such that it is the solution of the d'Alembert equation [33] in a vacuum of the form

$$\left(\frac{1}{c^2}\frac{\partial^2}{\partial t^2} - \nabla^2\right)\Psi(x,y,z,t) = 0, \tag{2.8}$$

where $\nabla^2 = \frac{\partial^2}{\partial x^2} + \frac{\partial^2}{\partial y^2} + \frac{\partial^2}{\partial z^2}$ is the Laplacian operator, c is the speed of light in a vacuum. The speed of light in a vacuum c can be expressed as $c = \frac{1}{\sqrt{\mu_0\epsilon_0}}$, where μ_0 and ϵ_0 are the permeability and permittivity of free space, respectively. We take an approach discussed by [34] involving the

spectral decomposition of $\Psi(x, y, z, t)$ into monochromatic components using the Fourier integral

$$\Psi(x, y, z, t) = \frac{1}{\sqrt{2\pi}} \int_0^\infty \psi_\omega(x, y, z) e^{-i\omega t} d\omega. \tag{2.9}$$

Each monochromatic component of the wavefield with angular frequency ω is written as the product of the spatial wavefield $\psi_\omega(x, y, z)$ and the harmonic time-dependent term $e^{-i\omega t}$. We substitute Eqn (2.8) into Eqn (2.9) to verify that each of these monochromatic time independent spatial wavefunctions $\psi_\omega(x, y, z)$ satisfy the Helmholtz equation of the form

$$(\nabla^2 + k^2)\psi_\omega(x, y, z) = 0, \tag{2.10}$$

where $k = \omega/c$ is the wavenumber. The Helmholtz equation can be used to describe an imaging process under the condition of a monochromatic x-ray wavefield that is commonly achieved using a monochromator with a synchrotron x-ray wavefield source. Unfortunately most radiological imaging especially in the clinical setting, is done using a polychromatic x-ray wavefield from a laboratory x-ray source with non-trivial spectral properties. Spectral decomposition of the wavefield into its monochromatic components enables imaging processes with a time independent approach for each component to be described. These components can then be combined to acquire a complete description of the polychromatic x-ray imaging process.

2.5.2 Paraxial Fields

We cannot generate an x-ray wavefield with no angular spread. We can however, impose certain conditions, which enables the generation of wavefields with small angular spread [35]. Under this condition the electromagnetic energy in the wavefield is concentrated within a small region about the wavefield axis with small spread. An electromagnetic field with these properties is referred to a paraxial field [36]. X-ray wavefields applied in phase contrast imaging also behave as paraxial fields. This enables the mathematical application of paraxial field to to phase contrast imaging, which simplifies the fundamental theoretical equation describing PCI. Thus, simpler algorithms are applicable to perform phase retrieval. To introduce the mathematical formalism and implicit approximations of paraxial wavefields, we consider the solution to the Helmholtz equation, Eqn (2.10) $\psi_\omega(x, y, z)$. For the following equations we drop the subscript ω under the assumption of a monochromatic wavefield. This wavefield is paraxial when

$$\psi(x, y, z) = \Phi(x, y, z) e^{ikz}, \tag{2.11}$$

where the variations of the complex envelope $\Phi(x, y, z)$ in the longitudinal position z are significantly smaller than the variations in the transverse (x, y) plane. From this $\psi(x, y, z)$ possess paraxial wavefield propagation along the z-axis, in such a manner that its complex envelope $\Phi(x, y, z)$ is modulated by a carrier plane wave e^{ikz} depicted in Figure 2.5. The condition of a near

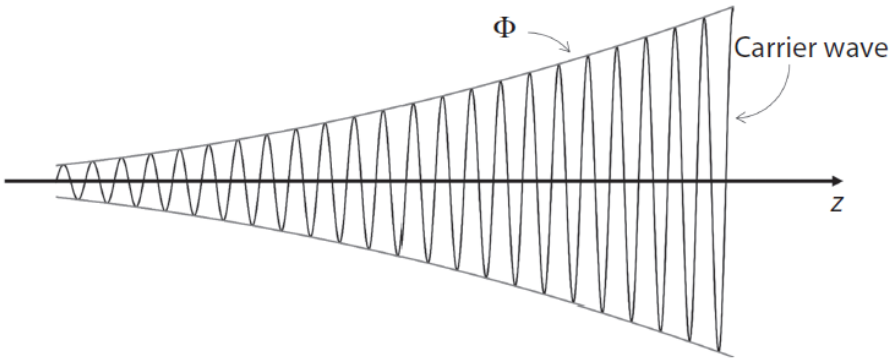

Figure 2.5: Schematic of paraxial wavefield propagating along the longitudinal path z displaying the effect of the oscillating carrier wavefield and the slowly varying complex envelope Φ. Adapted from [6].

longitudinal propagation is defined as the variation $\Delta\Phi(x, y, z)$ within some small longitudinal distance $\delta z = \lambda = 2\pi/k$ must be much smaller than the entire complex envelope such that

$$\frac{\Delta\Phi(x, y, z)}{\Phi(x, y, z)} << 1. \tag{2.12}$$

We know $\Delta\Phi(x, y, z) = (\partial\Phi(x, y, z)/\partial z)\Delta z = (\partial\Phi(x, y, z)/\partial z)\lambda$ so we can adapt Eqn (2.12) into

$$\frac{\partial\Phi(x, y, z)}{\partial z} << k\Phi(x, y, z). \tag{2.13}$$

Using a similar methodology, the analogous inequality for the second derivative of the complex envelope can be derived as

$$\frac{\partial^2\Phi(x, y, z)}{\partial z^2} << k^2\Phi(x, y, z). \tag{2.14}$$

This condition given in Eqn (2.14) can be used as a formal mathematical definition of a paraxial wavefield. We can then substitute Eqn (2.11) into the Helmholtz equation, Eqn (2.10) and then substitute Eqn (2.14) to neglect the term $\partial^2\Phi/\partial z^2$ with respect to the terms $k\partial\Phi/\partial z$ and $k^2\Phi$. In doing these

substitutions, we acquire the Helmholtz equation under the paraxial wavefield condition, otherwise reffered to the paraxial Helmholtz equation of the form

$$\nabla_T^2 \Phi(x,y,z) + 2ik\frac{\partial \Phi(x,y,z)}{\partial z} = 0. \tag{2.15}$$

Here $\nabla_T^2 = (\partial^2/\partial x^2) + (\partial^2/\partial y^2)$ is the transverse Laplacian. The parabolic x-ray wavefield is a concept heavily used when studying near-field diffraction of x-ray wavefields after propagating through a sample for PCI.

2.6 Inhomogeneous equations and the Refractive index

In the prior section all of the equations were derived with respect to the wavefield propagating through a vacuum. However in practice the wavefield will propagate through a medium in its direction of propagation. This requires the prior equations to be adapted to account for the presence of media along the wavefields propagation. In this section we will introduce fundamental x-ray interactions with matter along with their mathematical expressions and common approximations applied.

2.6.1 Inhomogeneous equations

We generalise the wave propagation equation by applying a macroscopic, position dependent and frequency dependent quantity called the refractive index $n(x,y,z)$. The refractive index is defined as

$$n(x,y,z) = \left(\frac{\epsilon(x,y,z)}{\epsilon_0}\right)^{1/2}, \tag{2.16}$$

where $\epsilon(x,y,z)$ is the electrical permittivity of the material. We can then modify the d'Alembert equation, Eqn (2.8) to account for the presence of nonmagnetic media to give

$$\left(\frac{n^2(x,y,z)}{c^2}\frac{\partial^2}{\partial t^2} - \nabla^2\right)\Phi(x,y,z,t) = 0. \tag{2.17}$$

Eqns (2.16) and (2.17) are valid for scalar wavefields as the wavefunction of wavefields describe the evolution of both electric and magnetic components of the wavefield and how they intertwine.

A single scalar wavefield is not sufficient if polarization effects are taken into consideration. However, this assumption is valid as for most cases of hard x-ray imaging were the variations in the optical density of any media are slowly varying such that the magnetic and electric wavefield components can be considered to be decoupled [6]. Hence, we shall continue to use our initial scalar theory approximation to x-ray wavefield propagation [6]. Returning to our derivations, we can apply a similar process as the prior section involving the complex wavefield, which obeys the d'Alembert equation, Eqn (2.17) being written as a superposition of monochromatic fields. From this we obtain the inhomogeneous Helmholtz equation of the form

$$(\nabla^2 + n^2(x, y, z)k^2)\psi(x, y, z) = 0. \tag{2.18}$$

We can then apply the paraxial approximation to this to obtain the inhomogeneous Helmholtz equation under the paraxial approximation [37] given as

$$\nabla_T^2\Phi(x, y, z) + 2ik\frac{\partial\Phi(x, y, z)}{\partial z} + k^2(n^2(x, y, z) - 1)\Phi(x, y, z) = 0. \tag{2.19}$$

With this we can now study x-ray PCI effects in imaging going into phase retrieval methods.

2.7 The Projection Approximation

In the hard x-ray regime the complex refractive index has magnitude that is close to one. This means that the strength of the interactions of the wavefield with matter is small i.e. most of the x-ray wavefield that propagates through the sample barely interacts with the media in the sample. This produces low contrast in the resulting phase contrast images however, it also allows us to apply some approximations to equations that describe the wavefield. One of these approximations is the projection approximation illustrated in Figure 2.6, where we consider a plane wavefield propagating along a direction z that is incident upon a sample [6].

The wavefield will undergo interactions with media within the sample, which will change the direction of propagation of the wavefield. However, if we assume that these interactions cause a very small change in the direction of propagation of the plane wavefield, we can simply ignore them and assume the wavefield propagates within the sample along the z direction. This assumption is called the projection approximation. Furthermore, all scattering within the sample can then be described via an exit wavefield at point z_0.

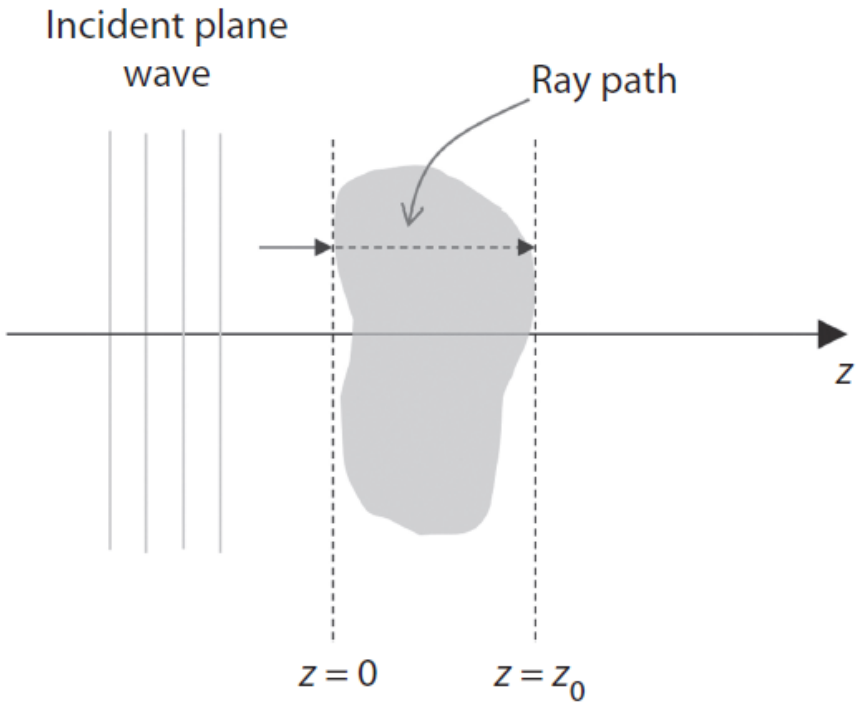

Figure 2.6: Schematic of an ideal path the x-ray wavefield would propagate with no sample present. The projection approximation disregards any change in the x-ray wavefield path induced from interactions of the x-ray wavefield with the sample. This approximation is feasible due to the low magnitude of these interactions. Adapted from [6].

Information concerning the change in amplitude and phase of the wavefield as it propagates through the sample can be recovered from the exit wavefield. Neglecting the inter-sample scattering effects disregards the Laplacian term in the inhomogeneous paraxial Helmholtz equation, Eqn (2.19) such that under the projection approximation we obtain [37] [38]

$$2ik\frac{\partial\Phi(x,y,z)}{\partial z} + (n^2(x,y,z) - 1)\Phi(x,y,z) = 0. \tag{2.20}$$

In summary, the projection approximation describes the propagation of x-ray wavefields through a sample via an exit wavefield immediately after exiting the sample, which contains the transverse phase and amplitude changes of the x-ray wavefield. The projection approximation assumes all scattering that occurs within the sample is completely described by the exit wavefield

by assuming that negligible diffraction occurs within the scattering volume. This condition holds when imaging quasihomogeneous objects but falls apart when a sample contains multiple highly contrasting media. This is because the diffraction occurring at the interfaces between media would need to be accounted for and following the discussed method with exit wavefields for each one of these interactions, which is highly unfeasible.

2.7.1 The Geometrical Optical Approximation

In order to forge a link between wave and ray theories of x-ray radiation the eikonal approximation is utilized for treating the interactions of coherent x-ray waves with matter. For this we need to derive the hydrodynamic formulation of the scalar wave optics of coherent x-ray wavefields. This is achieved by writing the coherent wavefield in terms of its intensity and phase, expanding the Laplacian term in Eqn (2.19), simplifying and separating the imaginary and real parts of the equation. The real part being the eikonal equation and the imaginary being the local conservation of optical energy [34].
The eikonal equation is a hydrodynamic formulation of the inhomogeneous Helmholtz equation, Eqn (2.19) given by [34]

$$|\nabla\phi_\omega(x,y,z)|^2 = k^2 n_\omega^2(x,y,z) + \frac{\nabla^2\sqrt{I_\omega(x,y,z)}}{\sqrt{I_\omega(x,y,z)}}, \tag{2.21}$$

where $\phi_\omega(x,y,z)$ is the phase and $I_\omega(x,y,z)$ is the intensity of the coherent wavefield. The eikonal equation is important as it allows x-ray disturbances that continuously evolve as the ray passes through a medium to be visualised [34]. The Geometrical Optics Approximation (GOA) is defined as the eikonal equation in the geometric optics limit [34].

$$|\nabla\phi_\omega(x,y,z)| = k n_\omega(x,y,z),\ k \to \infty. \tag{2.22}$$

It states that the phase gradient of plane waves passing through an inhomogeneous medium that is sufficiently weakly scattering, has practically the same orientation as the incident wave [34]. As well as the interactions of a pencil ray with matter is assumed to take place in an infinitesimal small volume in the object. This propagation is fully described in the forward diffraction in the object and the diffraction/transmission directions at the analyser crystal.

2.8 Attenuation and Phase

This section will cover how the equations discussed prior can be used to calculate the change in attenuation and phase of the x-ray wavefield and how this change can be visualised. Firstly, we can solve the boundary value differential equation for the inhomogeneous paraxial Helmholtz equation under the projection approximation, Eqn (2.20) [6] to obtain

$$\Phi(x, y, z_0) = \exp\left[\frac{k}{2i}\int_0^{z_0}(1 - n^2(x, y, z))dz\right]\Phi(x, y, z_0), \tag{2.23}$$

of the wavefield at position $z = z_0$. The index of refraction is defined as

$$n = 1 - \delta + i\beta, \tag{2.24}$$

where δ and β are the refractive and absorptive coefficients related to the microscopic scattering coefficients for the x-ray interaction with matter [17]. We can then substitute Eqn (2.24) taking into account that δ, $\beta << 1$ and therefore $n^2 \approx 1 - 2\delta + 2i\beta$ under the Binomial approximation into Eqn (2.23) to obtain

$$\Phi(x, y, z_0) = \exp\left[-ik\int_0^{z_0}(\delta(x, y, z) - i\beta(x, y, z))dz\right]\Phi(x, y, z_0). \tag{2.25}$$

From Eqn (2.25) we can obtain expressions for the phase shift and the attenuation for an x-ray wavefield propagating through a sample under the projection approximation. The phase shift is given by the imaginary exponent in Eqn (2.25)

$$\Delta\phi = -k\int_0^{z_0}\delta(x, y, z)dz, \tag{2.26}$$

while the attenuation is given by the real part of the exponent

$$\mu/2 = -k\int_0^{z_0}\beta(x, y, z)dz. \tag{2.27}$$

To clarify the ideas implemented in the previous expressions lets take an example of a wavefield incident upon a single homogeneous medium. For this case δ and β are independent of position hence the transmitted wavefield can be expressed as

$$\Phi(x, y, z_0) = \exp[-k(i\delta + \beta)t(x, y)]\Phi(x, y, 0), \tag{2.28}$$

where $t(x, y)$ is the projected thickness of the sample along z. From this we can calculate the transmitted intensity of the x-ray wavefield, which is the square modulus of the transmitted complex wavefield

$$I(x, y, z_0) = \exp[-\mu t(x, y)] I(x, y, 0). \tag{2.29}$$

This is the Beer Lambert law of attenuation, where the linear attenuation coefficient is defined as $\mu = 2k\beta = 4\pi\beta/\lambda$

2.8.1 Transport of Intensity Equation

An issue with our derivation of the x-ray wavefields is that any conventional detector will measure the intensity proportional to the square modulus of the complex wavefield. In this process as seen in Eqn (2.29), all information about the phase shift of the x-ray wavefield due to it propagating through the sample is lost. Hence, another direction needs to be undertaken starting with rewriting the complex envelope as

$$\Phi(x, y, z_0) = \sqrt{I(x, y, z_0)} e^{i\phi(x,y,z_0)}, \tag{2.30}$$

including the intensity and phase shift. We then substitute this expression, Eqn (2.30) into the paraxial homogeneous Helmholtz equation, Eqn (2.15) and equate the resultant imaginary component of the expression to be zero to obtain the Transport of Intensity Equation (TIE) [39]

$$\nabla_T \cdot [I(x, y, z_0) \nabla_T \phi(x, y, z)] + k \frac{\partial I(x, y, z_0)}{\partial z} = 0. \tag{2.31}$$

Recalling that traditionally only the intensity was measurable, the TIE proposes a crucial relation between the intensity and phase under the paraxial approximation. From this relation, we can obtain the phase shift caused by the wavefield propagating through the sample by measuring the intensity of the transmitted (measured just after the object) and propagated (measured at some distance after the object) wavefield. However, only derivatives of the phase can be recovered through phase retrieval and then integrated to give the phase shift.

2.9 Phase Retrieval

From observing the TIE, Eqn (2.31) one might conclude that it is sufficient to gain all information about x-ray phase contrast from sample where the paraxial approximation holds. Following the TIE if one lets the wavefield

propagate in free space then phase contrast effects will certainly appear in the image. As mentioned at the end of the previous section only derivatives of the phase are acquired from the TIE. To clarify this we expand the TIE Eqn (2.31), to obtain

$$\nabla_T I(x,y,z_0)\cdot\nabla_T\phi(x,y,z_0)+I(x,y,z_0)\nabla_T^2\phi(x,y,z_0)+k\frac{\partial I(x,y,z_0)}{\partial z}=0. \tag{2.32}$$

Assuming the longitudinal variation of the complex envelope is small compared to the transverse variation, we can approximate the partial derivative with respect to the z coordinate as follows

$$\frac{\partial I(x,y,z_0)}{\partial z}\approx\frac{I(x,y,z)-I(x,y,z_0)}{z-z_0}. \tag{2.33}$$

We can then substitute Eqn (2.33) into Eqn (2.32) and rearranging to give

$$I(x,y,z)=I(x,y,z_0)-\frac{z-z_0}{k}[\nabla_T I(x,y,z_0)\cdot\nabla_T\phi(x,y,z_0)+I(x,y,z_0)\nabla_T^2\phi(x,y,z_0)]. \tag{2.34}$$

This equation incorporates three components that comprise the measurable intensity at position $z > z_0$ beyond the sample along the wavefield direction of propagation. The first contribution contains only the sample attenuation, while the second and third components contain the first and second order derivatives of the phase, respectively. These phase derivatives can be processed through integration to give the phase information of an x-ray wavefield that has propagated through the sample. It is crucial to note that the TIE and the discussed method is just one of several phase retrieval methods for propagation based phase contrast imaging. There are further phase retrieval methods for differential phase contrast imaging methods such as grating and analyser based phase contrast imaging.

2.9.1 Attenuation contrast imaging

Wilhelm Roentgen discovered x-rays in 1895 [40]. Since then countless discoveries have been made describing how x-rays interact with matter. When an x-ray is incident upon a medium it can interact in several ways for instance it can be absorbed and/or scattered by the medium. Absorption contrast imaging has been the dominant imaging technique [41] due to its simple applicability and adaptability through techniques such as Computed Tomography (CT). Attenuation contrast is generated from the variance of the property of attenuation in the materials in the medium. This is achieved through exposure of a medium using x-rays with a detector on the opposing

side of the medium to the x-ray source. The detector over the exposure period will gather the measured intensity in each pixel. This can be displayed in an image conventionally called a radiograph. The measured intensity can then be compared with the known incident intensity distribution in order to calculate the attenuation properties of materials present in the medium. This method, commonly referred to as radiography, is simple to implement, understand and provides good contrast of materials with significant discrepancies in attenuative properties such as bone scans. Furthermore, it can be applied to CT (discussed in Chapter 3) where multiple projections (radiographs) are taken as either the object or source and detector are rotated to produce a 3-D image of the object. However, radiography and CT alike struggle to display contrast between materials or tissues with similar attenuation properties such as soft tissues. This can cause issues in clinical applications such as cancer detection if the malignant tissue has a similar attenuation property to its surroundings.

Now moving onto the theory let us start with the Beer Lambert equation, which describes the intensity change as an x-ray propagates through an object with linear attenuation μ over path length t.

$$I = I_0 \exp(-\mu t). \tag{2.35}$$

This is valid in this form only for monoenergetic photons, where I and I_0 are the final and initial intensities of the x-ray. From this we can use the relation between I and E to give

$$I = |E|^2 = E \cdot E^*, \tag{2.36}$$

where E is the amplitude of the wavefield given by

$$E = E_0 \exp(-ik(\delta - i\beta)t), \tag{2.37}$$

where E_0 is the initial amplitude of the wavefield, k is the wavenumber, δ is the refractive index decrement and β is the imaginary component of the index of refraction related to the linear attenuation coefficient μ by [42]:

$$\beta = \mu/2\kappa, \tag{2.38}$$

where δ and β describe the refractive and absorptive properties of materials and are related to the refractive index n by Eqn (2.24). We can substitute Eqn (2.37) into Eqn (2.36) to obtain

$$I = E_0^2[\exp(-ik(\delta - i\beta)t) \cdot \exp(-ik(\delta + i\beta)t)] = I_0 \exp(-2k\beta t), \tag{2.39}$$

which is the Beer Lambert equation. Attenuation is described as the reduction in intensity of a beam due to the effects of absorption, scattering and pair production [43]. The linear attenuation coefficient of a material μ is the sum of the linear attenuation coefficients for the photoelectric effect, Rayleigh scattering, Compton scattering and pair production (including triplet) denoted by τ, σ_R, σ_C and κ, respectively in Eqn (2.40) below

$$\mu = \sum_i \mu_i = \tau + \sigma_R + \sigma_C + \kappa. \tag{2.40}$$

X-ray interaction with matter depends on the incident x-ray energy E, atomic number Z (the number of protons in each atom of the material) and atomic scattering cross-section (measure of probability that a specific interaction occurs) of the material [43]. At the 10-30 keV energy range for x-rays which is considered in this thesis, only Rayleigh, Thomson scattering, the photoelectric effect and Compton scattering are applicable [44].
Thomson scattering occurs at low photon energies where the incident photon beam is scattered off the free electron [44]. Rayleigh scattering happens when an incident photon scatters off a bound orbital electron. The energy transferred from these two interactions is negligible and the scattered photon has the same initial energy but a different propagation direction [44]. No ionization occurs with energy and momentum being conserved during these interactions, which have higher probability at low energies.
The photoelectric effect occurs when an incident photon interacts with a tightly bound orbital electron (for instance from the K-shell), the photon is completely absorbed by the atom and the electron is ejected from the atom [44]. Electrons from the L and M shells then move down to fill the K-shell vacancy producing characteristic x-rays whose energies are equal to the difference in binding energies between the two involved shells. There is a spike in the attenuation coefficient when the x-ray's energy reaches and just surpasses the binding energy of the K-shell called the K-edge.
The K-edge can be used to discern materials, which appear similar in the image. This is achieved by taking images at the energies just below and above the K-edge and comparing them. However, this requires knowledge of the K-edge of the concerned material. This can be challenging as the K-edges for soft tissues occur at a few keV, which is too low energy to generate a useful image. The probability of the photoelectric effect is proportional to Z^3/E^3 [43]. This means the photoelectric effect dominates for low E and high Z, which makes it ideal in conventional radiography for bone scans. This is because bones are composed of materials with relatively high atomic

number and mass density than the surrounding tissue.
During Compton scattering an incident photon interacts with a loosely bound orbital electron it causes the electron to recoil and be ejected from the atom due to the transfer of energy [44]. Energy and momentum are conserved between the two particles in this interaction but the incident photon loses energy given by the Compton waveshift equation [44].

$$\Delta\lambda = \lambda' - \lambda = \lambda_C(1 - \cos(\theta)). \tag{2.41}$$

Where θ is the scattering angle, $\lambda_C = 2.43 \cdot 10^{-12}$m is the Compton wavelength, while λ and λ' are the wavelengths of the incident and scattered photons, respectively. Compton scattering dominates at diagnostic energies in soft tissue, it is independent of Z, increases with E and density of the material. This leads to a lot of scatter in images especially when moving into high energy imaging. This decreases the contrast in the image.

2.9.2 Phase contrast imaging

We previously introduced phase contrast imaging in Section 2.8.1 and this section will expand on the concept. Phase contrast imaging concerns the reconstruction and measurement of the real part of the wave and refractive index, Eqn (2.24) that details the refractive properties of the material. This offers another method of differentiating materials in medical images, which in the past could be presumed identical if they have similar attenuation coefficients β but possess different refractive coefficients δ. Furthermore, δ is much greater than β in the hard x-ray spectrum for light materials such as water and soft tissues [11] as observed in Figure 2.7.

Phase contrast can be orders of magnitude larger than absorption contrast, meaning it can produce better soft tissue visibility [45] as phase contrast effects decline slower than conventional absorption contrast with the increase of energy of X-rays as observed in Figure 2.7. High energy x-ray imaging is desirable as it results in less radiation dose delivered to the patient [46]. For conventional radiography (absorption-based) this is at the cost of image quality due to the Compton effect becoming dominant at higher energy incident x-rays, causing lower image quality due to the intensity contrast decreasing. This makes phase contrast imaging extremely desirable in clinical applications concerning tissue that is particularly radiosensitive such as mammography (imaging of the breast) [47]. Additionally δ is directly proportional to the electron density, which is another useful property of materials that can be utilized to help differentiate them. It is not possible to directly

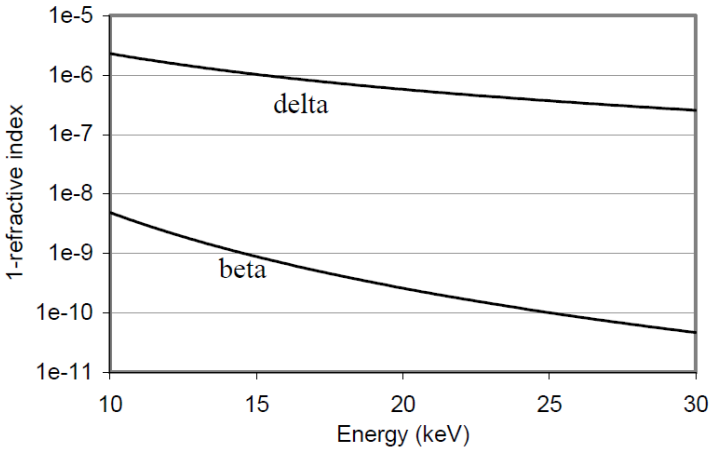

Figure 2.7: Plot of the refractive index components against energy for water showing that even in low diagnostic energies the phase coefficient δ has a larger value than the absorption coefficient β. This means that at this and higher energy ranges phase contrast imaging will be able to produce higher contrast images than absorption based imaging with less delivered dose. Adapted from [7].

obtain the electron density of a material from its attenuative properties μ.

In PCI the near field regime is utilized from Fresnel diffraction, which occurs when a wave transmits through a sample and propagates further in the near field. This causes any diffraction pattern to differ in size and shape depending on the distance between the object and the projection [48]. The near field regime approximation holds for small propagation distances and for slow varying objects [19]. The GOA is valid when the Fresnel number $N_F = h^2/\lambda d$ [49] is larger than unity. Here h is the size of the object detail to be imaged that is limited by detector pixel size, d is the propagation distance. When the Fresnel number $N_F > 1$ Fresnel diffraction applies due to the near field condition. When $N_F < 1$ Fraunhofer diffraction occurs, in which the resultant wavefronts are considered planar rather than spherical as the wavefront has spread out over a large region giving rise to an interference pattern. This will begin to interfere with different parts of the image as observed in Figure 2.8.

r_f is defined as the Fresnel length and given by [8]

$$r_F = \left(\frac{2\pi p}{k}\right)^{1/2} = (\lambda p)^{1/2}, \tag{2.42}$$

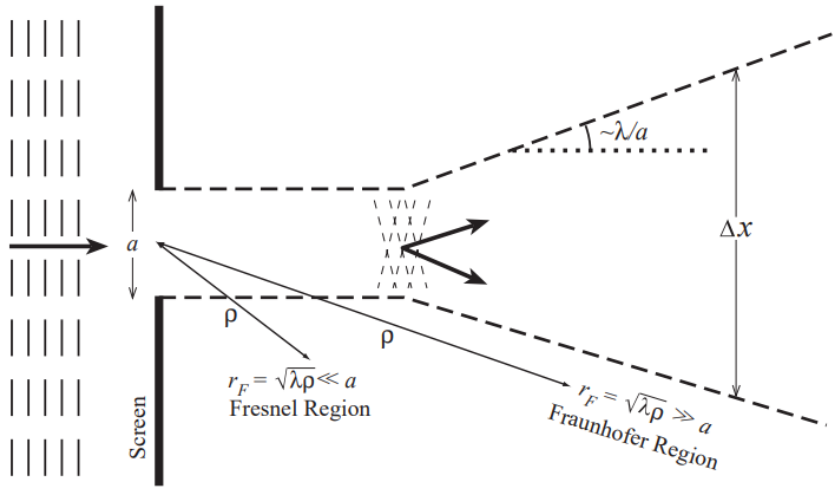

Figure 2.8: Schematic of Fraunhofer and Fresnel diffraction. We see an x-ray wavefield incident upon an aperture with slit size a, which the wavefields are filtered through. After they pass through the aperture slit the spread of the spherical wavefield a is maintained in the Fresnel Region until approximately $r_F/a = 0.5$ where the x-ray wavefield is considered planar and spreads out over a large region Δx in the Fraunhofer region. We use the spherical wavefield in the Fresnel region for PCI to apply the GOA in the phase retrieval process. We can observe this wavefield behaviour change from the plots of the distribution of the x-ray wavefield intensity in Figure 2.9. Adapted from [8].

where p is the distance between the wavefront and the aperture slit. We use the spherical wavefield in the Fresnel region for PCI to apply the GOA in the phase retrieval process. We can observe this wavefield behaviour change from the plots of the distribution of the x-ray wavefield intensity in Figure 2.9.

2.9.3 Propagation based phase contrast imaging

At sufficient object to detector distances Fresnel diffration fringes appear in the projection of the object in the detector that demonstrates the image contrast as shown in Figure 2.10 below. This method is called Propagation Based Phase Contrast Imaging (PBPCI). PBPCI requires no optical elements to render phase shifts as visible phase contrast. This means PBPCI can be achieved through free space propagation [10] [50] and can be described by

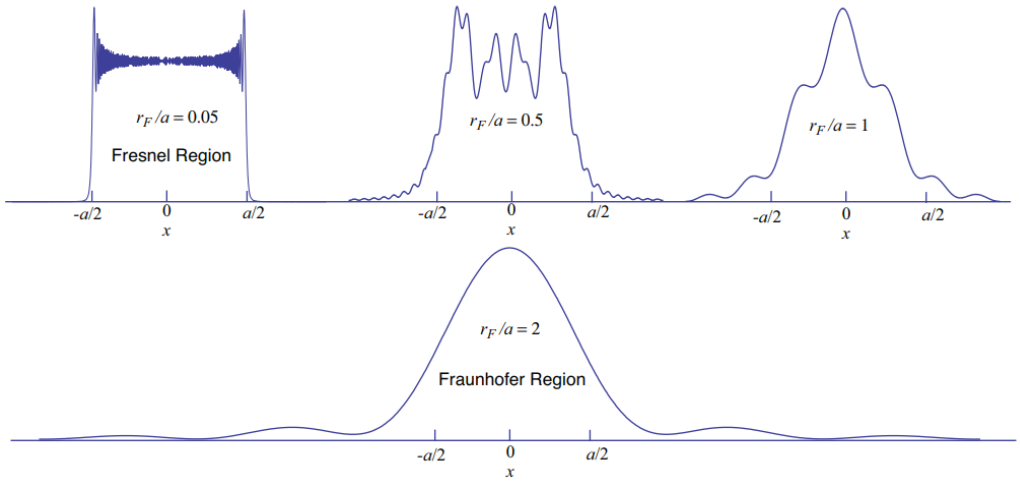

Figure 2.9: Distribution of intensity of the x-ray wavefield as it propagates away from the aperture after undergoing diffraction. We see that at $r_F/a = 0.05$ the intensity distribution resembles the aperture slit with damped oscillations (interference fringes) near the edges caused by the aperture diffraction. As r_F/a increases the diffraction pattern transitions from Fresnel to Fraunhofer region seen by the umbra and penumbra broadening significantly before the interwavefield interference patterns become discernible. Adapted from [8].

the TIE, Eqn (2.31) [39].

The simplicity of its implementation makes it highly desirable in clinical applications. It can acquire bright field (transmitted) phase contrast images providing good contrast for low dose [51]. Its other advantages are its 2D phase gradient sensitivity, easy interpretation and high sensitivity to abrupt phase changes. However, it requires an x-ray beam with high spatial coherence and high spatial resolution of the registration system otherwise interference fringes are rapidly smeared out and provides lower contrast compared to other imaging methods [52]. This is due to PBI being sensitive to the Laplacian (second-order derivative) of the gradient of the phase, while ABI and GI are sensitive to the first derivative of the phase.

PBPCI can be described by the Transport of Intensity Equation (TIE) [39]: Eqn (2.31) in Section 2.8.1. This equation is derived from the imaginary component of the expanded inhomogeneous Helmholtz equation, Eqn (2.19) when considering a coherent paraxial scalar wave-field traveling in the z di-

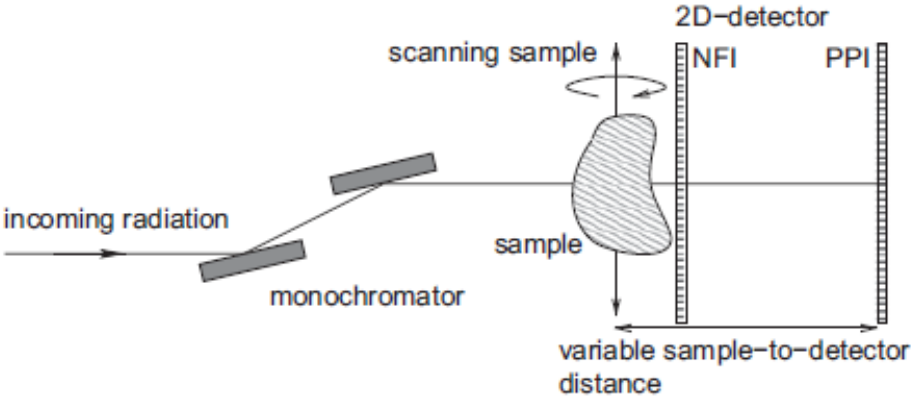

Figure 2.10: Experimental setup of PBI where a monochromatic transversally coherent x-ray fan beam traverses the sample while its rotated. The intensity is then recorded by a 2-D detector at different distances to show the rendering of Fresnel diffraction patterns in the images. PPI - phase propagation x-ray imaging and NFI - near field imaging. Adapted from [9].

rection. This equation expresses the variation of the product of intensity and the gradient of phase along the Poynting vector which represents the directional energy flux of an electromagnetic field. Convergence of the Poynting vector results in an increase in intensity, while divergence results in a decrease in intensity.

Let us consider the scenario of PBPCI of a single material object with projected thickness $T(x, y)$ illuminated by a plane wave of uniform intensity I_0. Then under the projection approximation both the phase and amplitude at the exit surface can both be obtained simultaneously. This means the projected thickness can be reconstructed using a single image as long as the exit wavefield is obtained at a distance from the sample that is sufficiently small for the Fresnel number to be much greater than unity [50]:

$$T(x,y) = -\frac{1}{\mu} log_e \left(\mathcal{F}^{-1} \left\{ \frac{\mathcal{F}[I(x,y,z=\Delta)/I_0]}{1+(\delta\Delta/\mu)(k_x^2+k_y^2)} \right\} \right), \tag{2.43}$$

where $T(x, y)$ is the projected thickness at some position (x, y), $\mathcal{F}$ and $\mathcal{F}^{-1}$ are the Fourier and inverse Fourier transforms, Δ is the propagation distance, $I(x, y, z = \Delta)$ is the intensity at $(x, y, z = \Delta)$, k_x and k_y are the Cartesian coordinates in Fourier space and $\delta = \mathrm{Re}(1 - n)$. Despite its assumptions, this algorithm is simple, fast, has very significant noise robustness and can process time dependent objects frame by frame [53].

2.9.4 Differential Phase Contrast

The term $\nabla_T I(x, y, z_0) \cdot \nabla_T \phi(x, y, z_0)$ of the expanded TIE, Eqn (2.32) can be utilized to measure a different type of phase contrast compared to propagation based phase contrast that is dependent on the first order derivative of the phase. This phase contrast effect typically requires optical elements to be placed along the beam line or a focused x-ray beam in order to produce a phase-contrast image. The relevant terms in the TIE is the dot product between the intensity gradient and phase gradient $\nabla_T I(x, y, z_0) \cdot \nabla_T \psi(x, y, z_0)$.

This implies that when a sufficiently strong intensity gradient is present an optical system can be used to generate the phase gradient which can be retrieved using a phase retrieval method dependent on the applied optical system. We can derive this simply by taking an x-ray plane wave incident on a uniform non-absorbing medium giving the refractive index of the material to be $n = 1 - \delta$. The phase difference between the wave fronts incident at position y and $y + \Delta y$ is $\Delta\phi = \delta k \Delta t$, where Δt is the change in thickness from one position to the other. For small displacements following the projection approximation we have $\Delta t = \alpha \Delta y / \delta$ [42]. α is the refraction angle that is defined as the change in direction of the wavevector after the wave has propagated through the interface. If α is small then it can be approximated from Snell's law as $\alpha = \theta_1 - \theta_2$ to give Snell's law in the form

$$\alpha = \delta \tan \theta_1, \tag{2.44}$$

where θ_1 and θ_2 are the angle of the incident and diffracted wavefield, respectively. Using the relations between Δt and α we can write $\Delta\phi / \Delta y = k\alpha$ which for very small displacements can be written as

$$\frac{\partial \phi}{\partial y} = k\alpha. \tag{2.45}$$

2.9.5 Interferometry

The first interferometry x-ray phase contrast imaging was developed by Bonse & Hart in 1965 utilizing a triple Laue monolithic crystal x-ray interferometry setup as seen in Figure 2.11, that could record thickness fringes from the interference pattern [54].

Interferometry based x-ray phase contrast imaging was further developed by Ando and Hosoya through recording phase changes induced in the wavefront by the sample [55]. X-ray interferometry provides high sensitivity to

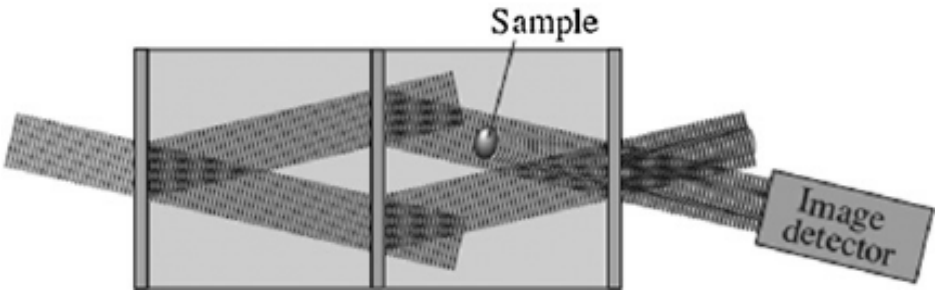

Figure 2.11: Schematic of a crystal x-ray interferometer where the entire interferometer was monolithically cut from a silicon crystal. Within the body are three equally spaced parallel lamellae act as wavefield splitters where the incident x-ray wavefield diffracts off at the Bragg angle following Eqn (2.48). The x-ray wavefield is coherently divided into transmitted and diffracted components which are then incident on the second lamellae. The second lamella causes the beams to split again in the same manner. The two beams that overlap at the third lamella are also divided and interference is observed in the beams outgoing from the third lamella captured by the detector [10]. Adapted from [11].

phase gradients [56] as demonstrated by Momose and Fukuda [11] analysing a slice of rat cerebellum. However, this method requires prior quantitative understanding of the sample such as its shape and composition along with a complex setup, as the alignment mechanism requires extremely high precision [57]. This is so that the optical path lengths are stable within deviations smaller than the x-ray wavelength. However, it is often not possible to obtain this quantitative information about the sample prior to being imaged especially when concerning biological samples. Furthermore, the stability of optical path lengths condition is difficult to satisfy when moving to smaller wavelengths and thus higher energy x-ray beams as these require the condition to be even more strenuous. This is unfortunate as high energy x-ray energy imaging is one of the main benefits of PCI. The perfect large crystals required are also difficult to produce and keep stable during the image acquisition time.

2.9.6 Edge Illumination

Edge Illumination (EI) makes use of two absorbing masks made up of alternating absorbing and transmitting lines, where one mask is placed just before the sample with the other placed in front of the detector as shown in Figure 2.12. The masks create many small beamlets incident on the sam-

ple/detector. These masks are slightly misaligned with respect to one another so that a fraction of photons that pass through the first, pass through the second [58]. Individual apertures in the detector mask are aligned with a line of pixels on the detector, which can measure the transmitted intensity [59]. This configuration observes slight changes in the beamlets direction caused by refraction. This changes the proportion of photons being stopped by the second mask, which subsequently changes the signal in the detector. The masks can then convert refraction caused by the sample into a measurable intensity. The detector is customly designed to render phase effects visible at the detector [60].

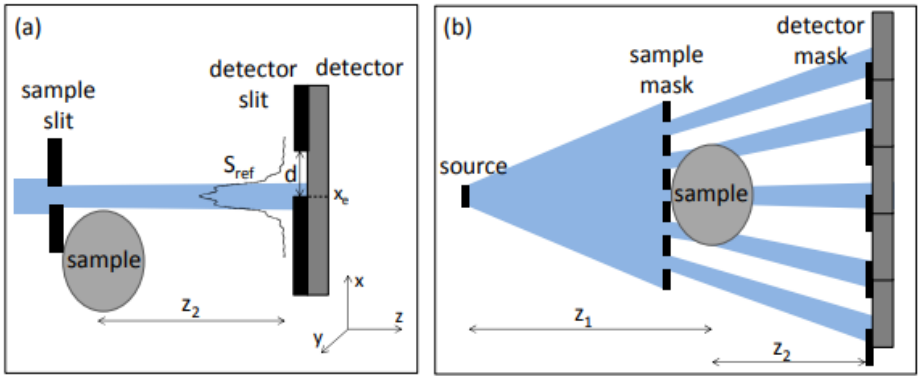

Figure 2.12: Schematic of an edge illumination setup in the case of (a) a laminar wavefield with a sample and detector aperture; (b) a 2-D wavefield from a source incident upon a sample mask followed by the sample in the near-field regime before propagating through the detector aperture into the detector. Where S_{ref} is the wavefield distribution d is the aperture slit width and z_1 and z_2 are the source to sample and sample to detector distances respectively [12]. Adapted from [12].

This method has high angular sensitivity and enables low dose implementations [46]. Previously, this method required two images acquired in different setup configurations. An approach by Diemoz [61] using a single image to retrieve an approximate x-ray phase map is based on the assumption of a quasihomogeneous object. This is an object that has a constant ratio between δ and β components of the index of refraction. EI also assumes the case of a near field regime so that the TIE is valid. However, the EI setup causes noise amplification in the reconstructed image. Only scattered angles that produce an intensity of the refracted wavefield higher than the noise level are effectively detected [12]. Furthermore, EI is compatible with polychromatic

x-ray sources [62] [63] [64].

2.9.7 Speckle Based Imaging

Speckle based phase contrast imaging utilizes a speckle mask placed between the source and object. It assumes that (1) the sample is an optically thin x-ray transparent object that geometrically distorts the reference x-ray speckles (2) the geometric distortion conserves the integrated intensity of the reference speckle image. The speckle object generates an intensity pattern in the near field domain caused by mutual interference of scattered waves. The near field domain used as the speckle pattern is determined by the wavefront transmission upon propagation in the Fresnel zone [65].

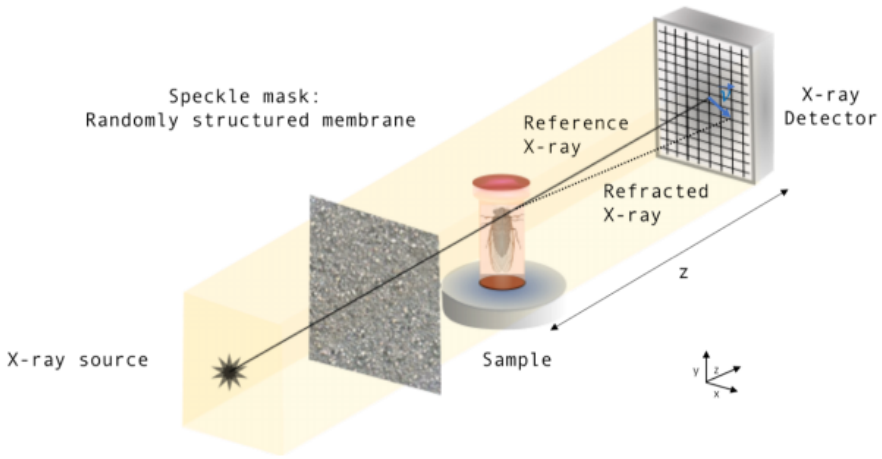

Figure 2.13: Speckle based x-ray tracking imaging setup where an x-ray source produces x-ray wavefields, which propagate through a speckle mask before propagating through a sample and being detected by the detector. In this example setup the reference pattern can be the high x-ray speckle pattern [13] created by illuminating a piece of sandpaper [14]. Adapted from [15].

Speckle based methods are compatible with low coherence x-ray sources [66] making them more applicable in clinical settings. Unfortunately it requires several exposures to achieve high resolution leaving it vulnerable to artefacts. This is to due sample or setup displacements (mechanical instability) and unfit for imaging moving samples (living creatures) especially due to its high sensitivity [15]. Image resolution has limitations due to the speckle grain

size and artefacts appear in the reconstructed image for the case of complex objects due to the underlying assumption of a quasihomogeneous object [15].

2.9.8 Grating Interferometry

X-ray grating interferometry is a method for hard x-ray wavefront sensing and phase contrast imaging. It is sensitive to small deviations of the local propagating wavefront but does not require high x-ray monochromaticity meaning it can be applied with a conventional x-ray source [67]. It instead requires precise alignment of the gratings with small periods and high aspect ratio that are sufficiently separated from each other to produce the interference effect [52]. Two 2-D grids are used as shown in Figure 2.14, where the first grating (G1) is used as a beam splitter to diffract the beam and the second grating (G2) is used as an analyser[61]. These two grids analyse the phase and intensity of the refracted beam [52]. In order to create a pattern of period T at the G_2, G_1 will have a period of $2T$. Recent projects utilize Talbot interferometry that achieves second order differential phase contrast [68]. This technique is based on the observation of self imaging from diffraction grating described as Fresnel diffraction in a periodic grating first observed for visible light [69]. Interference from a pure phase grating produces an interference pattern at multiples of the Talbot distance d_T, which is defined as

$$d_T = 2p^2/\lambda, \tag{2.46}$$

where p is the period of the grating. However, intensity modulation is observed at fractional distances after the grating [10]. In first Talbot geometry the intensity varies sinusoidally as described [10] by

$$I(X_g) = a_0 + a_1 \cos(2\pi x_g/p_2 + \phi_1), \tag{2.47}$$

where x_g is the displacement of the grating, ϕ_1 is the phase shift, $p_2 = p/2$ is the period of the absorption grating and a_0, a_1 are coefficients that described the average intensity including background and the amplitude change in intensity respectively [10]. When an object is placed in the beam either in front or behind the phase grating the wavefront is deviated and the intensity pattern is shifted, which can be measured [10].

Data collection proceeds by translating G_1 vertically (horizontally with respect to Figure 2.14) in steps through a full period of the grating (at least 5 images must be acquired for each projection) [70] with and without the sample present in the x-ray wavefield. Quantitative measurement of the wavefield scattering, attenuating and diffracting as it propagates through the sample

can be acquired by observing the intensity in each pixel as a function of the position of G_2 [6]. Grating interferometry previously could not achieve 2-D phase gradient sensitivity, which Rutishauser et al [2] achieved by tilting the two grids by an angle $\pi/4$ with respect to the optical axis as observed in Figure 2.14. This was achieved by comparing data gathered from a flipped

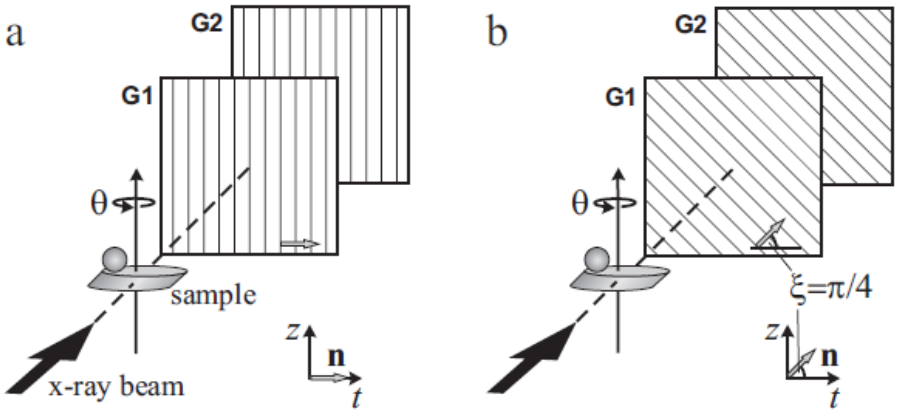

Figure 2.14: Schematic of grating phase contrast imaging setup using two 1-D grating interferometers. A sample is mounted on a rotation axis θ to allow for tomographic scans. Beyond the sample are the beam splitter phase grating G1 and absorbing analyser grating G2. Setup (a) depicts a conventional arrangement with the grating lines parallel to the rotation axis of the sample and (b) the grating lines are rotated by $\pi/4$ anticlockwise with respect to the optical axis. By doing this and comparing the flipped and non-flipped projection images a full 2-D gradient can be determined. Adapted from [2].

tomographic projection at angles θ and $\theta + \pi$ in order to determine a full 2-D gradient of the phase to generate a better reconstructed phase image. Thus the flipped projection has reversed t (spatial) direction and gradient component along t (see Figure 2.14). This is fixed by flipping the t direction of the $\theta + \pi$ projection so that the measured directional derivatives overlap and can be analysed [2].

2.9.9 Analyser Based Imaging

ABPCI traditionally referred as Diffraction Enhanced Imaging (DEI) [71], is a technique where a wave illuminates a sample with a near-perfect analyser crystal placed after the sample as observed in Figure 2.15. In ABPCI the first crystal (or crystals) acts as the monochromator and the second crystal (or crystals) acts as a spatial frequency filter (analyser) [1]. The analyser

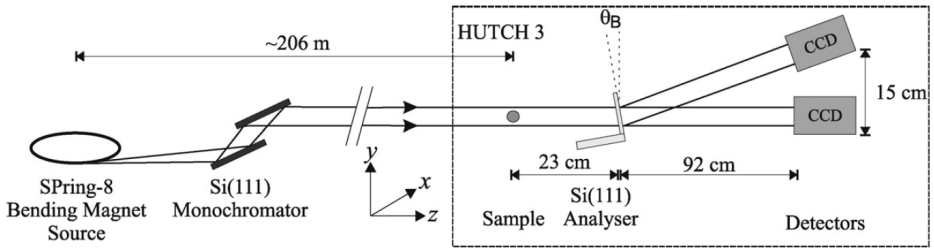

Figure 2.15: Schematic setup of Laue geometry ABPCI, where x-rays from the synchrotron source are filtered through the monochromator to become a single energy (monochromatic) beam before incident on the sample. The x-ray wavefield then interacts with the Si(1 1 1) analyser crystal allowing only parts of the wavefield that satisfy the Bragg condition, Eqn (2.48) to be diffracted, while the rest are transmitted through the analyser crystal. The diffracted and transmitted wavefields are then captured by the CCD detector. Adapted from [3].

crystal achieves this through utilization of the Bragg law, which is defined by the equation

$$2d_{hkl}\sin(\theta_B) = \lambda, \tag{2.48}$$

where hkl are Miller indices of the crystallographic planes of the analyser crystal, d is the separation of the crystallographic planes, θ_B is the Bragg angle and λ is the wavelength of the incident beam [34]. The Bragg law is used to impose Bragg condition on incident wavefields using an analyser crystal. This places a range of accepted values around the Bragg angle in the microradian scale. This filters out x-rays that are outside the Bragg condition range and produces a rocking curve that requires dynamical theory to model the diffraction in thick ideal crystals [34].

Another way of defining the Bragg law and visualising the effects is in the context of kinematical x-ray diffraction under the Born approximation (scattering field small compared to the incident wavefield) from a crystal. The geometrical x-ray diffraction condition holds when scattered waves are only observed in the $\hat{x}$ direction such that $\vec{g}_{hkl} - k\hat{x} + \vec{k}_0 = 0$ that can be rewritten into [34]

$$k\hat{x} - \vec{k}_0 = \Delta\vec{k} = \vec{g}_{hkl}, \tag{2.49}$$

where the incident and scattered wave vectors are given by $\vec{k}_0$ and $k\hat{x}$, respectively and $\vec{g}_{hkl}$ is the reciprocal lattice vector. This can be shown to be equivalent to the Bragg law, Eqn (2.48) and allows kinematical x-ray diffraction to be visualised in terms of a Ewald sphere [72].

When a wavefield is incident upon the crystal at an angle θ_B, it is diffracted at the Bragg angle θ_B, some of the wavefield is instead transmitted through the crystal. In Bragg geometry it is often assumed that the crystal is sufficiently thick as observed in Figure 2.17 to negate the transmitted wavefield as it is not utilized and could potentially cause unwanted noise in the image [45]. Laue geometry as shown in Figure 2.18 uses a thin crystal that allows the transmitted wavefield to pass without being completely absorbed by the crystal [34]. However, thin crystals are vulnerable to the Pendellosung effect, which is the exchange in energy between the incident and diffracted interfering wavefields in the crystal [16]. In the case of a thin Laue crystal such as Figure 2.18, the transmitted and diffracted intensity can be loosely described as a sine and cosine function, respectively as shown in Figure 2.16.

Figure 2.16: Standard sine and cosine curves (blue and red lines respectively) with amplitude 1 showing the relation between the diffracted and transmitted wavefield intensities, respectively. If we chose a thickness of the Laue crystal z such that $Az = \pi/4$, where A is some arbitrary constant we will have no diffracted wavefield intensity and maximum transmitted wavefield intensity as $\sin(\pi/4) = 1$ and $\cos(\pi/4)$. This relation is known as the Pendellosung effect, hence we have to be careful about our Laue crystal thickness in order to avoid it having an unwanted effect [16].

We observe from Figure 2.16 where A is some arbitrary value and z is the thickness of the crystal, that at certain values of z there is little or no transmitted beam and vice versa. This means that the selection of crystal thickness is crucial to initially obtain relatively even intensity of diffracted and transmitted [16]. The effects behaviour is similar to the transfer of energy between two coupled pendulums [73]. This causes the resultant rocking curve to be highly oscillatory where the period of oscillation depends upon the thickness of the crystal [6]. The transmitted beam is compromised of two

components, one component is zeroth order diffracted under the Bragg condition, while the other component simply propagates through the thin crystal unchanged [74]. A thin crystal reduces blurring caused from doubling imaging in the transmitted beam due to its two components experiencing different refractive properties. The Laue geometry utilizes a thin crystal as in Figure 2.19 allows simultaneous dual phase contrast imaging [75] [76] using the transmitted and refracted x-ray wavefield [77].

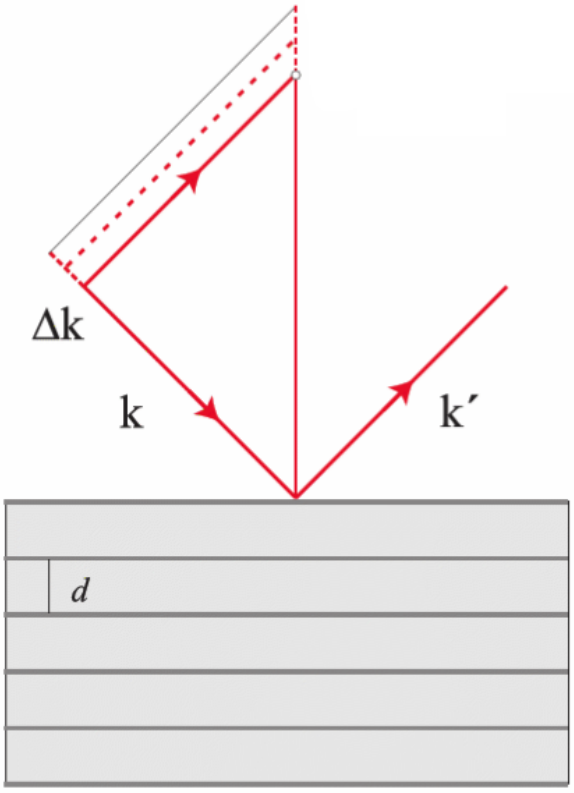

Figure 2.17: Diffraction by a crystal with a lattice spacing of d in Bragg reflection in symmetric case, the exit and entrance beam have the same angle with the entrance surface. The large thickness of the crystal means that there will be no transmitted beam that exits the crystal. The crystal reflects a spread of wavelengths given by Δk that are diffracted by the Bragg condition with the rest being rejected. Where k and k' are the incident and diffracted scattering wave vectors. Adapted from [17].

Images are acquired by sampling the angular intensity profile of an x-ray wavefield that has passed through a sample at different angular positions

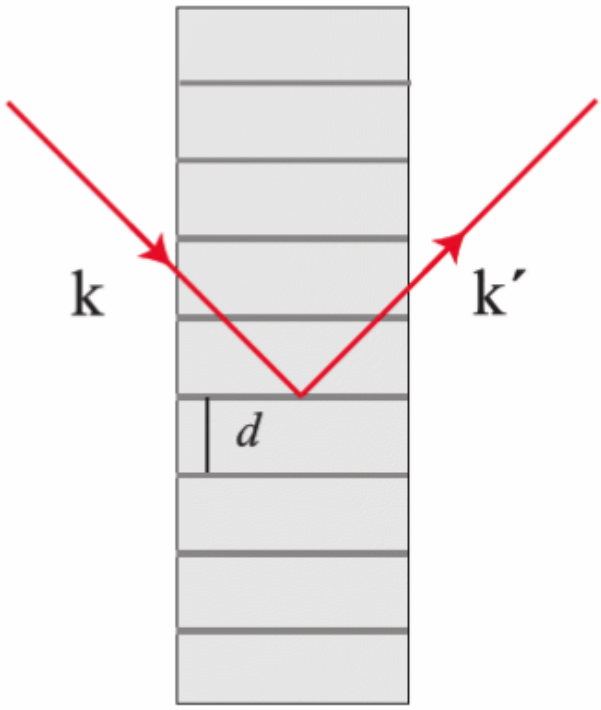

Figure 2.18: Diffraction by a crystal with a lattice spacing of d in the Laue transmission geometry. In the symmetric case the incident and exit beams form the same angle with respect to the external surface of the crystal. This setup allows the transmitted wavefield to exit the crystal. Adapted from [17].

of the analyser crystal [78]. By rotating the analyser crystal and recording the diffracted and transmitted intensities, the angular dependent diffractivity and transmissivity of the crystal (the rocking curve) can be produced [79] as seen in Figure 2.20. The shape of the rocking curve depends on the type, thickness and orientations of the analyser crystal as well as the divergence and spectrum of the incident beam.

Ultra Small Angle Axis Scattering (USAXS) provides an important contribution to generation of the image contrast in ABPCI [80], where its effect is utilized when analysing scattered x-ray wavefield angle on the microradian scale. USAXS partially falls within the acceptance of the analyser crystal under the Bragg condition and broadens the observed rocking curve [81] [82]. This is due to the scattering curve being convolved with the rocking curve causing any increase in USAXS to further broaden the rocking curve. Similarly, any peak shifts of the rocking curve are due to refraction in the material.

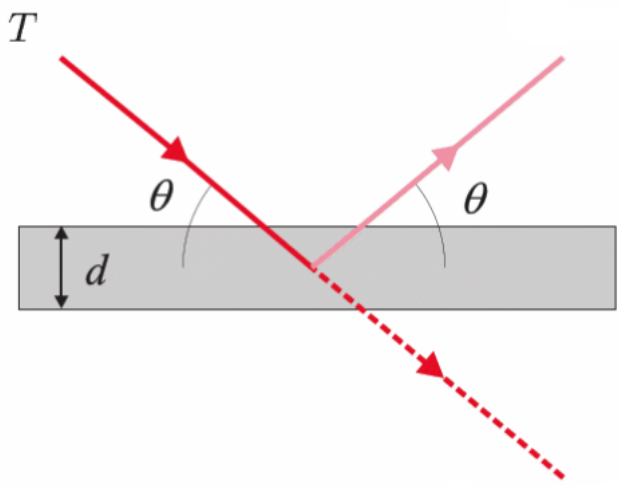

Figure 2.19: Bragg geometry for a thin crystal. Wave T incident on sheet of lattice crystal is partially diffracted and transmitted. This can be used to simultaneously acquire diffracted and transmitted images in ABI helping to reduce scanning time. Where θ is the x-ray wavefield incident and in this case diffraction angle upon the Laue crystal. Adapted from [17].

Absorption, diffraction and scattering images are calculated from the differences in the zeroth, first and second order moments of the RC's [83].

Phase retrieval is generally performed by measuring the rocking curve with and without the sample present. This enables the attenuation, refraction and USAXS distribution to be measured through their respective changes such as the integral, centroid and width of the curve [6]. These effects are what produces the contrast in ABI. However, they require several images to be taken at multiple orientations in order to gather the necessary information about the object. This methodology applies the Bragg geometry and is known a Multiple Image Radiography (MIR). This typically requires about 8 sets of data in order to accurately model the USAXS distribution [80]. MIR does produce high contrast images of inhomogeneous mediums at the cost of long experimental and exposure times to account for the multiple data sets and low photon counts in the detector, respectively.

An alternative to the Bragg geometry is to employ the Laue geometry and detect the diffracted and transmitted x-ray wavefield simultaneously [75] [76]. These two images can be used to separate the absorption and phase infor-

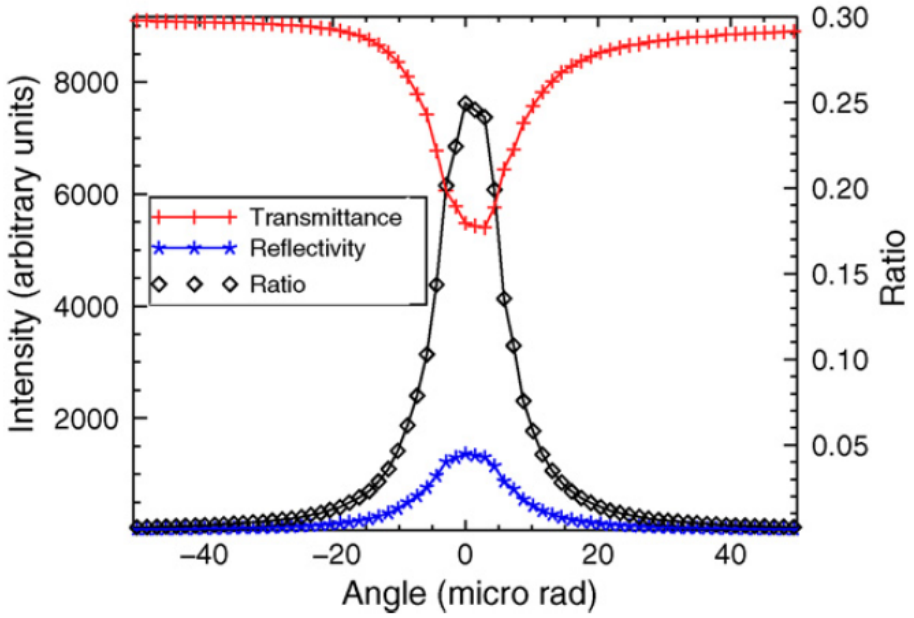

Figure 2.20: Measured diffracted and transmitted rocking curves and their ratio. Noise is alleviated by smoothing the rocking curves. This can be done by fitting a model of the curve such as Lorentzian, Gaussian, Pearson VII or Voitigan functions. Adapted from [3].

mation. If the USAXS effect is significant in the recorded images, then a simultaneous two-image reconstruction will result in significant artefacts in the reconstructed image as USAXS is not taken into account in this method. This problem is alleviated by employing an iterative phase retrieval procedure that separates the absorption, phase and USAXS. The GOA can be applied to the Laue geometry to approximate the transmitted and diffracted intensities as

$$I_D = I_0 \cdot D(\theta), \tag{2.50}$$

$$I_T = I_0 \cdot T(\theta), \tag{2.51}$$

where I_0, I_D and I_T are the initial, diffracted and transmitted intensities of the wavefield. Furthermore, $D(\theta)$ and $T(\theta)$ are angularly dependent diffractivity and transmissivity of the rocking curve. The GOA assumes that only small angle axis scattering occurs when an x-ray propagates through a medium. The GOA holds when the Takagi number $N_T = (h/\Lambda_x \sin(\theta))^2$ is much larger than unity [49]. Where h is the size of the object detail to be imaged, Λ_x is the extinction length of the crystal (the crystal volume within

the extinction length that considerably contributes to diffraction) and θ is the wavefield angle of incidence.

Phase retrieval was initially done by modeling the bell-shaped rocking curve as a triangle using a Taylor series expansion [71] at the angular position corresponding to the half maximum of the curve as this is the most linear part of the rocking curve [71] [84]. This model of the rocking curve can cause significant artefacts in the reconstructed image due to the severe inaccuracy of the model around the peak and tails of the curve. Gaussian functions are commonly used to fit the rocking curve [85] [86] as it accurately models the bell curve shape and some authors argue that it provides the best reconstruction with relatively simple implementation [87].

However, Gaussian functions can fail to properly model the peak and tails of the RC [88] [89] due to the long slit geometry of ABI. This property is caused by scattering being integrated in a direction perpendicular to the diffraction plane, broadening the tails of the rocking curve [90]. This happens because the analyser crystal only filters x-ray wavefields in the vertical plane meaning x-ray wavefields from a broad range of horizontal directions can be accepted by the analyser crystal. To account for this an aperture is applied that filters x-ray wavefields along the horizontal axis but we still integrate over the entrie horizontal axis causing this effect [91]. Pseudo-Voigtian [92] and PearsonVII functions provide superior fitting and thus phase retrieval at the cost of complexity. One of the most successful applications in applying PearsonVII functions to fit RC's was performed by Kitchen et al [79]. This alleviates artefacts using a straightforward method the provides a good fit. Hall et al [93] showed that a Pearson VII function given by

$$y = c\big[1 + (x - \tilde{x})^2/(ma^2)\big]^{-m}, \tag{2.52}$$

can be used to model the rocking curve. Where c defines the amplitude, $\tilde{x}$ is the centroid, m is the rate of decay of the tail and a and m determine the profile of the curve. This function can be adapted to the type of bell curve by modifying the m such as the Lorentzian ($m = 1$), the modified Lorentzian ($m = 2$) and Gaussian ($m \to \infty$). ABI can yield high contrast images of soft tissue with low background noise due to the high angular selectivity of scattering from the sample. However, its three major downsides are (1) the need for high mechanical stability of the crystals otherwise this will result in errors in the reconstructed data (2) significant loss of intensity due to the filtering of the x-ray wavefield from the monochromator and analyser crystal. This is a significant limitation especially on conventional x-ray sources for ABPCI

as they produce a broader polychromatic beam. (3) Limited FOV, which is determined by the maximum size of the crystals and the Bragg diffraction condition, Eqn (2.48). This limits the size of the object ABPCI can image.

The Rocking curve intensities under the GOA are given by the expressions

$$I_D = I \cdot D(\Delta\theta + \Delta\theta') \tag{2.53}$$

$$I_T = I \cdot T(\Delta\theta + \Delta\theta') \tag{2.54}$$

where I_D and I_T are the diffracted and transmitted intensities, I is the intensity of the beam incident on the crystal, $\Delta\theta$ is the deviation from the Bragg angle and $\Delta\theta'$ is the shift caused by diffraction in the object as seen in Figure 2.21. These equations are only valid as the object is approximately quasihomogeneous meaning that USAXS, which causes the rocking curves to broaden is negligible [81] [83]. These rocking curves are produced for every pixel in images to mitigate the imperfections of the analyser crystal and the deviations of the incident beam from a plane wave that could cause an observable shift in the rocking curve. By dividing the diffracted intensity, Eqn (2.53) by the transmitted intensity, Eqn (2.54) we can obtain an expression

$$\frac{I_D}{I_T} = \frac{D(\Delta\theta + \Delta\theta')}{T(\Delta\theta + \Delta\theta')}, \tag{2.55}$$

which indepentent of the intital intensity I making it an ideal RC to model and perform phase retrieval. We can use Eqns (2.53) and (2.54) to give expressions for the ratio and initial intensity I

$$I = \frac{I_D}{D(\Delta\theta + \Delta\theta')}, \tag{2.56}$$

$$I = \frac{I_T}{T(\Delta\theta + \Delta\theta')}. \tag{2.57}$$

This gives us a relation to calculate the intensity contrast as the x-ray wavefield passes through an object. However, we normally obtain the intensity contrast map of the x-ray wavefield by fitting an inverse PearsonVII function of the form $f - d[1 + \theta^2/(nb^2)]^{-n}$ to obtain for instance, the transmitted intensity as

$$I_T = IT(\theta) = I\{f - d[1 + \theta^2/(nb^2)]^{-n}\}. \tag{2.58}$$

The PearsonVII coefficients b, d, and n are equivalent to a, c and m in Eqn (2.59) and applied to avoid confusion between the two fitted RCs with f

being the only unique coefficient. We use the ratio of the transmitted and diffracted images in order to remove the variable I, making it easy to fit a Gaussian or PearsonVII function to the curve to measure $\Delta\theta'$. We apply a Pearson VII function rocking curve given by Eqn (2.52) to the ratio RC to adapt Eqn (2.55) into

$$\frac{I_D}{I_T} = c[1 + (\Delta\theta + \Delta\theta')^2/(ma^2)]^{-m}, \tag{2.59}$$

where the centroid $\tilde{x}$ has been set to 0 for simplicity. We can rearrange Eqn (2.59) for $\Delta\theta + \Delta\theta'$ to give

$$\Delta\theta + \Delta\theta' = \pm a\sqrt{m[(cI_T/I_D)^{1/m} - 1]}, \tag{2.60}$$

which is an expression for the angular deviation of the wavefield incident upon the analyser crystal. The ratio RC has to be fitted as there is no simple analytic solution that can be found for $\Delta\theta+\Delta\theta'$ given the term $\frac{D(\Delta\theta+\Delta\theta')}{T(\Delta\theta+\Delta\theta')}$ when both $D(\Delta\theta+\Delta\theta')$ and $T(\Delta\theta+\Delta\theta')$ are expressed as PearsonVII functions [79]. The phase shift of the wave can be expressed in the form of

$$\Psi = -\int k\delta(x, y, z)dz. \tag{2.61}$$

We can measure the change in the phase gradient by looking at the angular shift in the rocking curve caused by the object in the beam.

$$\frac{\partial\Psi}{\partial x} = -k\left[\frac{\partial}{\partial x}\int \delta(x, y, z)dz\right]. \tag{2.62}$$

From this we make the important deduction that the change the phase gradient results in a change in angle $\Delta\theta'$. Therefore we can equate for $\Delta\theta'$ to get

$$\Delta\theta' = \left[\frac{\partial}{\partial x}\int \delta(x, y, z)dz\right]. \tag{2.63}$$

Knowing this we can numerically integrate the function $\frac{\partial\Psi}{\partial x}$ using a numerical method such as Euler's or Newton's method to calculate the phase Ψ.

In this thesis we are testing a theory discussed in Rutishauser et al. 2011 paper [2], where by 8° rotation of the object and detector clockwise following the x-ray propagation direction, a two dimensional phase gradient can be reconstructed. This is done through differential phase images from opposing

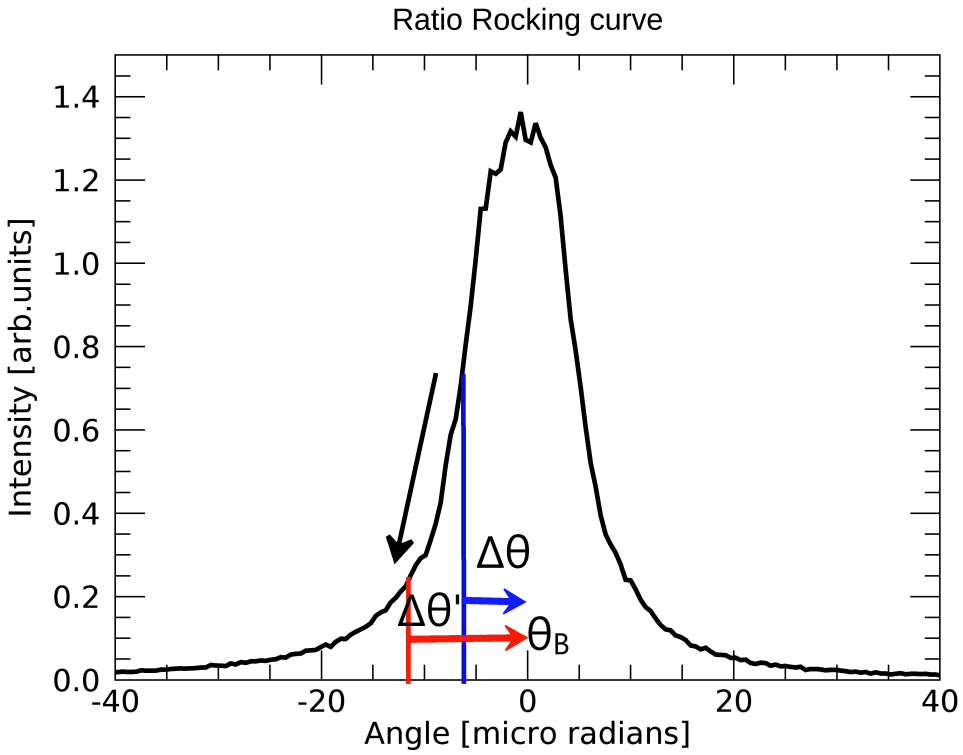

Figure 2.21: Ratio RC of the diffracted RC divided by transmitted Rc with no sample present. The analyser crystal was positioned at the blue line on the RC through rotating it about the horizontal axis to achieve an angular shift $\Delta\theta$, shown as the blue arrows from the Bragg angle θ_B, which is set to zero. When an object is placed in the path of the wavefield it will cause refraction and attenuation in the wavefield propagated through the object. This changes the incident angle of the wavefield entering the analyser crystal and thus shifts it to a new position on the RC shown as the red line with an angular shift $\Delta\theta'$ shown as the red arrows from θ_B. We can calculate this shift in intensity and incident angle of the wavefield entering the analyser crystal caused by the phantom from the acquired transmitted and diffracted projections. These calculations will generate an intensity and two $\Delta\theta$ maps for every projection as observed in Figures 5.11, 5.13 and 5.15, respectively.

projections being combined that will produce both components of the phase gradient vector $\frac{\partial\Psi}{\partial x}$ and $\frac{\partial\Psi}{\partial y}$ by retrieving two $\Delta\theta'$'s. The equations for these

two $\Delta\theta'$'s will be of the form

$$\Delta\theta' = \kappa_1 \frac{\partial}{\partial x}\left[\int \delta(x,y,z)dz\right] + \kappa_2 \frac{\partial}{\partial y}\left[\int \delta(x,y,z)dz\right], \tag{2.64}$$

$$\Delta\hat{\theta}' = \kappa_3 \frac{\partial}{\partial x}\left[\int \delta(x,y,z)dz\right] + \kappa_4 \frac{\partial}{\partial y}\left[\int \delta(x,y,z)dz\right]. \tag{2.65}$$

Where $\Delta\hat{\theta}'$ is the rocking curve shift at the $\theta + 180°$ projection and κ_1, κ_2, κ_3 and κ_4 are constants accounting for the rotation of the detector and sample at both projections. To calculate these values we need to consider the effect of 8° inclination to the object and detector by looking at both the non-inclined and inclined geometry as seen in Figures 2.22 and 2.23 respectively.

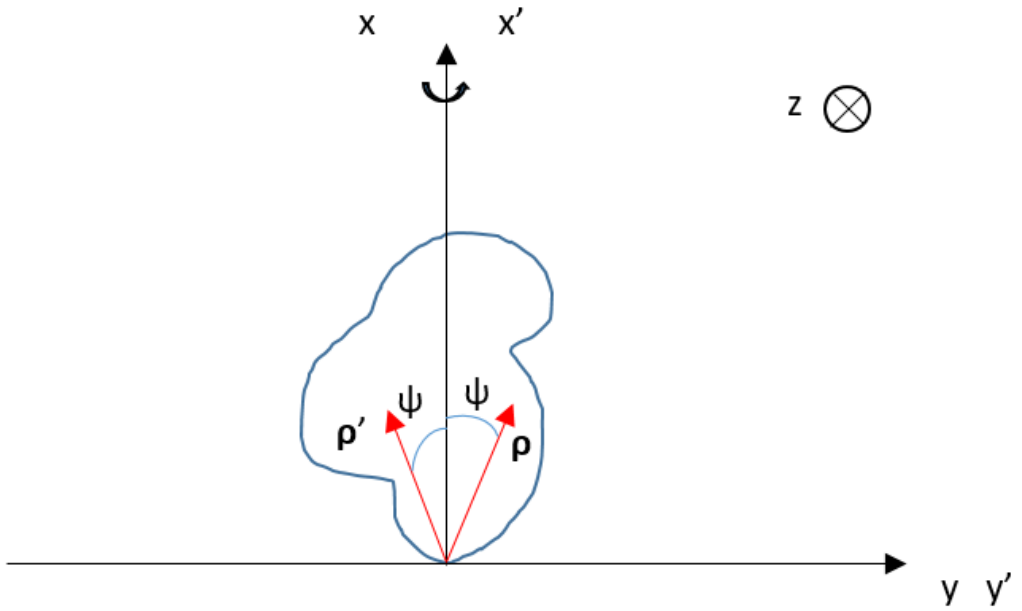

Figure 2.22: Non-inclined geometry of vector $\boldsymbol{\rho}$ with its corresponding 180^0 projection $\boldsymbol{\rho}'$ where the two coordinate systems x', y' and x, y for the object detector and analyser crystal, respectively are equivalent and z is the propagation direction of the x-ray wavefield going into the page. In this setup the analyser crystal is only sensitive to variations in the x direction.

Consider we have a projection vector $\boldsymbol{\rho}$ and its respective 180° projection $\boldsymbol{\rho}'$ for the non-inclined geometry we can derive a simple expression for the x,

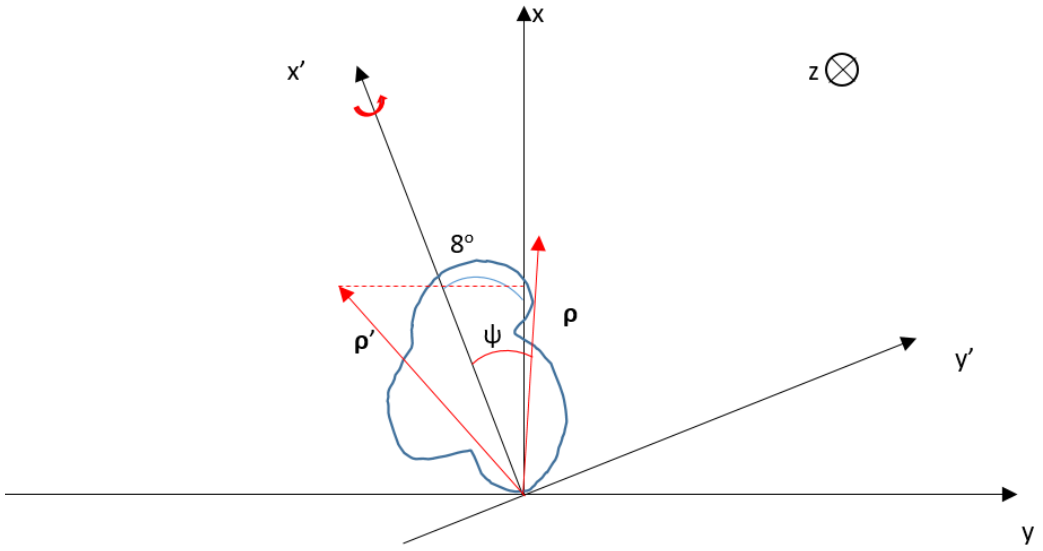

Figure 2.23: Inclined geometry where the object, detector and therefore (x', y') coordinate system has been rotated 8° anticlockwise with respect to the (x, y) coordinate system about the optical axis z. While the analyser crystal is still only sensitive to the x direction in the (x, y) coordinate system, it is sensitive to both the x' and y' components of the gradient of phase. This allows a 2-D phase gradient to be reconstructed from comparison of the two projections $\boldsymbol{\rho}$ and $\boldsymbol{\rho}'$ as they provide unique information in the inclined geometry setup.

x' and y, y' components of $\boldsymbol{\rho}$ using simple trigonometry

$$\boldsymbol{\rho}_x = |\boldsymbol{\rho}| \cos\psi = \boldsymbol{\rho}_{x'}, \tag{2.66}$$

$$\boldsymbol{\rho}_y = |\boldsymbol{\rho}| \sin\psi = \boldsymbol{\rho}_{y'}. \tag{2.67}$$

Where $|\boldsymbol{\rho}|$ is the magnitude of vector $\boldsymbol{\rho}$, x' and y' are the axes for the object and detector, x and y are the axes for the analyser crystal, which is only sensitive to variations in the x direction and ψ is the angle between the vector and the x' axis. The scalar components for the two coordinate systems are equivalent as in this case (Figure 2.22) the coordinates systems are identical. However, if we rotate the detector and sample by 8° clockwise along the path of the wavefield the x', y' coordinates and the orientation of the object will change with respect to coordinates x, y as seen in Figure 2.23. We can again derive expressions for components of $\boldsymbol{\rho}$ and utilize the cosine law

$\cos(A+B) = \cos A \cos B - \sin A \sin B$ to give

$$\boldsymbol{\rho}_x = |\boldsymbol{\rho}| \cos(\psi - 8) = |\boldsymbol{\rho}|[\cos\psi \cos 8 + \sin\psi \sin 8] = \delta\theta', \tag{2.68}$$

$$\boldsymbol{\rho}'_x = |\boldsymbol{\rho}| \cos(\psi + 8) = |\boldsymbol{\rho}|[\cos\psi \cos 8 - \sin\psi \sin 8] = \delta\hat{\theta}', \tag{2.69}$$

from Eqn (2.63). From here we can add Eqns (2.68) and (2.69) to obtain

$$\delta\theta' + \delta\hat{\theta}' = 2|\boldsymbol{\rho}| \cos\psi \cos 8. \tag{2.70}$$

We then substitute Eqn (2.66) and rearrange to give

$$\boldsymbol{\rho}_{x'} = \frac{\delta\theta' + \delta\hat{\theta}'}{2\cos 8}. \tag{2.71}$$

Similarly for subtracting Eqns (2.68) and (2.69) we get

$$\delta\theta' - \delta\hat{\theta}' = 2|\boldsymbol{\rho}| \sin\psi \sin 8. \tag{2.72}$$

Once again substituting Eqn (2.67) to give

$$\boldsymbol{\rho}_{y'} = \frac{\delta\theta' - \delta\hat{\theta}'}{2\sin 8}. \tag{2.73}$$

Therefore going back to Eqns (2.64) and (2.65) the expression for the κ's is given by

$$\kappa_1 = \cos(8), \tag{2.74}$$

$$\kappa_2 = \sin(8), \tag{2.75}$$

$$\kappa_3 = \cos(8), \tag{2.76}$$

$$\kappa_4 = -\sin(8). \tag{2.77}$$

This method will allow the derivation of a 2-D phase gradient and produce a higher quality and more detailed image. This is achieved by flipping one of the 180° opposing plane by 180° so that it matches with its opposing plane. These planes will tell different information about the object that can be extracted and used in tomographic reconstruction. However, because of the small 8° inclination angle this setup will still be dominantly sensitive in the x direction.

Chapter 3

Computed Tomography

Conventional absorption based radiogrpahy's fundamental problem is that it measures a projection of three dimensional object into a two dimensional plane with a concomitant loss of spatial information because of this. This was overcome by employing Computed Tomography(CT), which takes radiographic projections of a sample over a wide range of projection angles. It then reconstructs an image of the object as a 3-D image. This is important to discuss as most phase contrast techniques employ tomography in the image acquisition and reconstruction. For standard radiography the intensity recorded in a detector behind the sample is given by Beer's law of attenuation, Eqn (2.35) [17]. Using Eqn (2.35), line integrals of the attenuation coefficient of the object can be obtained. From this process an intensity distribution can be constructed in the form of a Radon function $R(\theta, x')$ where θ is the viewing angle and x' is the coordinate perpendicular to the direction of the performed line integral. The Radon transforms can be reconstructed into a two dimensional object algebraically or using Fourier analysis, which utilizes the Fourier slice theorem. The latter is computationally efficient but also gives more artefacts that arise due to interpolation error. The Fourier slice theorem is given by [17]

$$F(q_x, q_y = 0) = \int p(x) e^{iq_x x} dx = P(q_x), \tag{3.1}$$

where $p(x)$ is the projection of a 2-D function, q_x and q_y are the x and y coordinates in Fourier space. This implies "the Fourier transform of the projection along a particular line of a two-dimensional function $f(x, y)$ is equal to a slice through the Fourier transform of $f(x, y)$ taken along a line passing through the origin in the propagation direction" [17].

Utilizing the Fourier slice theorem CT scanning consists of three steps as

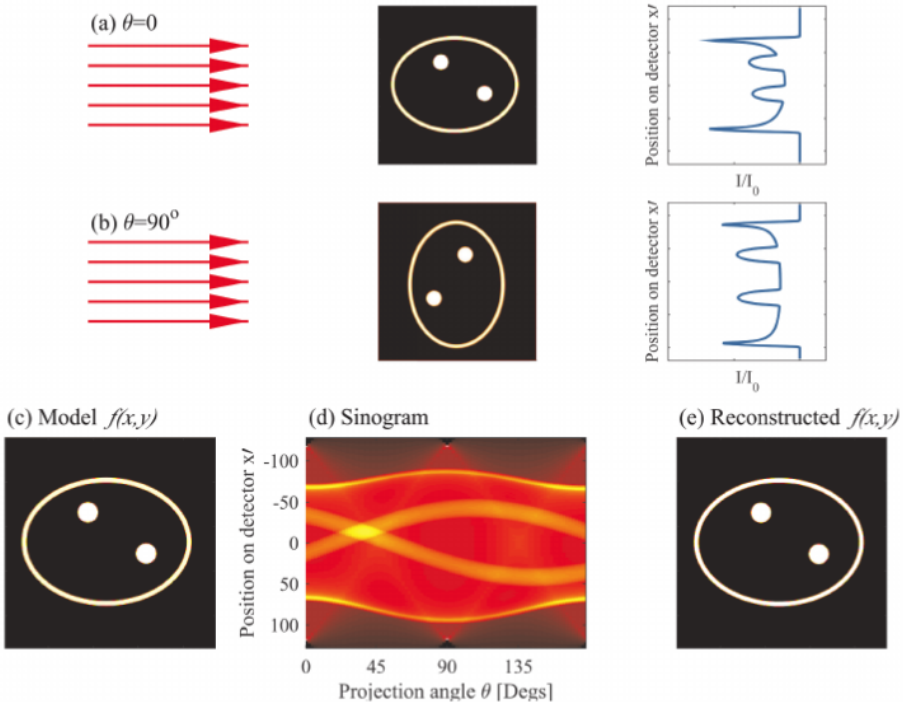

Figure 3.1: Reconstruction of a 2-D object from its Radon transform. (a)(b) Projectional data (Radon transforms) of the object at angles $\theta = 0°$ and $90°$ respectively has been recorded and plotted in the respective right diagrams. (d) The sinograms for the projections. (c) The model is used to improve reconstruction time of the final image (e). Adapted from [17].

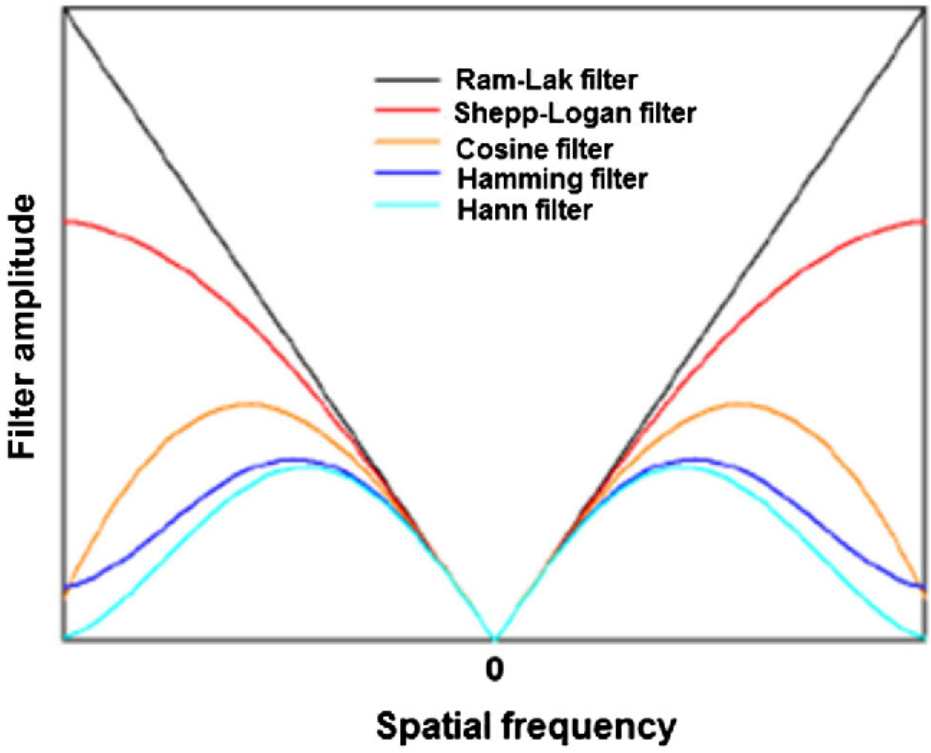

Figure 3.2: Plot of filters applied to the interpolation of the image reconstruction to remove noise, blurring and artefacts. Roll off filters (all but Ram-Lak) are applied to stop the amplification of high frequencies and exacerbation of quantum noise that occurs when applying the Ram-Lak filter. All the filters have distinct advantages and disadvantages as seen by their differing curve shape. Adapted from [18].

shown in Figure 3.1. (1) The acquisition of the data in a series of radiographs (projections). (2) The data is Fourier transformed utilizing the Fourier slice theorem, so the Fourier transform of the object can be constructed. (3) An inverse Fourier transform is performed to obtain the reconstruction of the image. Interpolation in the reconstruction process is usually done through backprojection using a stabilized discrete version of the inverse Radon transform. Typically, filters observed in Figure 3.2 are applied in interpolation of the image reconstruction process such as filtered back-projection using a ramp filter to remove artefacts.

The ramp filter compensates blurring occurred in back projection, it also amplifies high frequencies and can exacerbate quantum noise [4] hence, roll

off filters are used to alleviate this issue. Iterative methods are typically used during this reconstruction process as it produces good quality image. This helps diminish noise and artefacts that might appear in the reconstructed image. Models or error matrices of the image can be used to help speed up the reconstruction process as they reduce the assumptions and number of iterations required to generate a high quality image. However, models of the image require quantitative understanding of the object to be imaged, while error matrices can be difficult to implement and can worsen image quality if applied incorrectly. We utilize CT to calculate the δ and β maps by performing 180° CT reconstruction using the acquired phase maps after 2-D Fourier integration (see Section 2.4).

Chapter 4

Experimental Methods

This chapter incorporates the experimental setup to perform inclined geometry ABPCI by rotating the object and CCD detector 8° clockwise about the optical axis following the x-ray wavefield to generate a 2-D phase gradient discussing all of the components used. We will focus on key components such as the monochromator, analyser crystal, object and CCD detector and include relevant details. This includes the distance the components were separated from each other and the importance of aligning each of them before beginning the experimental procedure. The procedure section will go through how the transmitted and diffracted data were taken and adapted by applying corrections for effects that occur during this experiment involving the x-ray wavefield and CCD detector.

4.1 Setup

The experiment was performed at the SPring-8 synchrotron radiation facility in Japan in 2012. An ABPCI experimental setup utilizing tilted Laue geometry as observed in Figure 4.1 in hutch 3 of beamline 20B2 in the Biomedical Imaging Centre was applied. All experimental data for this thesis was acquired using this setup from this hutch. With respect to Figure 4.1, going from left to right, we have the SPring-8 synchrotron, in Japan where this experiment took place, set to produce x-ray wavefields approximately 210m away from the sample. These x-ray wavefields in the optical hutch then interacted with a double-bounce monochromator in a non-dispersive setup consisting of two parallel Si(1 1 1) crystals that filtered the x-ray wavefields to a monochromatic wavefield with energy bandwidth $\Delta E/E \approx 10^{-4}$ keV [94] (discussed in Section 2.2). These x-ray wavefields then interacted with the object that is rotated 8° clockwise following the propagation direction of the

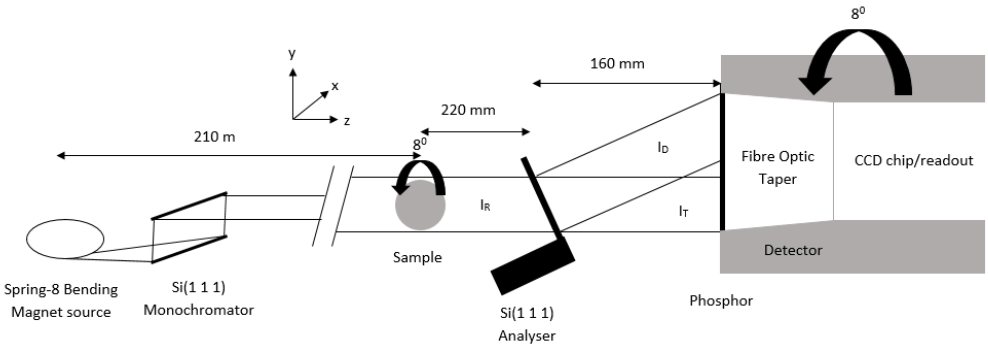

Figure 4.1: Inclined geometry Laue ABPCI experimental setup.

x-ray wavefield. The x-ray wavefield traveled 220 mm from the sample is then incident on the near perfect Si(1 1 1) analyser crystal in the Laue geometry. This consists of a nominally 100 μm thick silicon wafer that is connected at the base to a monolithic silicon slab. This results in an interaction between the x-ray wavefield and the analyser crystal that causes the x-ray wavefield to be diffracted and transmitted by the analyser crystal. The 26 keV diffracted x-ray wavefield then propagates with an angle $2\theta_B = 8.722°$ of arc [95] with respect to the propagation direction of the incident wavefield. The data from these separated beams are then gathered by a 4000×2672 pixel Hamamatsu CCD camera, with a tapered fibre optics bond to the CCD chip and the 20 μm thick gadolinium oxysulfide ($Gd_2O_2S : Tb^+; P43$) phosphor. The CCD detector with native pixel size of 9 μm was converted to an effective pixel size of 16.2 μm by the 1.8:1 taper ratio. The CCD detector is positioned 160 mm away from analyser crystal and is also rotated 8° clockwise following the propagation direction of the x-ray wavefield.

Pictures of the experimental setup with explanations are shown in Figures 4.2 and 4.3 below, which display some of the components used in the experimental procedure.

The application of the 8° clockwise inclination to the object stage and CCD detector about the optical axis parallel to the wavefield propagation direction is observed in Figure 4.3 of the experimental setup looking into the wavefield. These figures help emphasise the complex experimental setup applied to achieve the required precision for ABPCI to produce high quality phase contrast images.

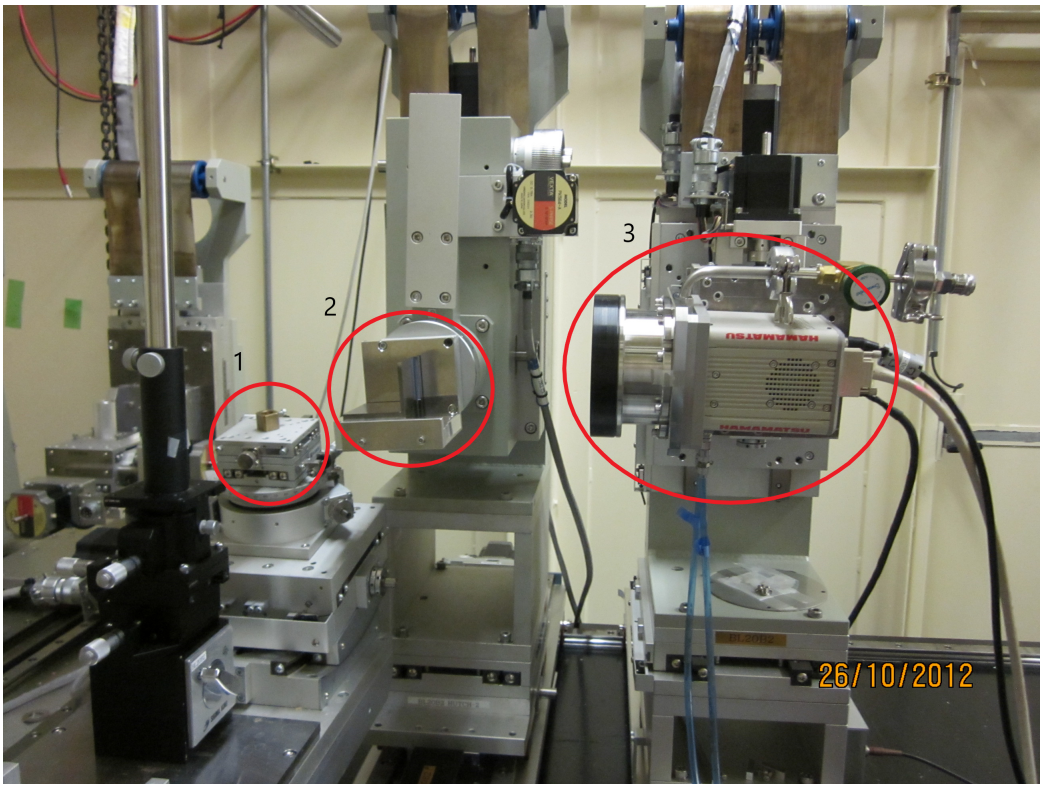

Figure 4.2: Picture showing some key components in the experimental setup displayed in Figure 4.1. Moving from left to right; beginning with 1 we have the object stage, which holds the object in place and allows rotation about the horizontal and vertical axes in order to acquire tomographic projections and apply the inclined geometry, respectively. In 2 we have the analyser crystal stage, which holds the analyser crystal tightly in place (importance of this is emphasised in the Analysis section, Section 5.4) and also allows rotation about the horizontal axis. Finally, in 3 the CCD detector that acquires the transmitted and diffracted data produced by the analyser crystal to be used to reconstruct the δ and β map of the imaged object. We can observe the inclination of the these stages in Figure 4.3.

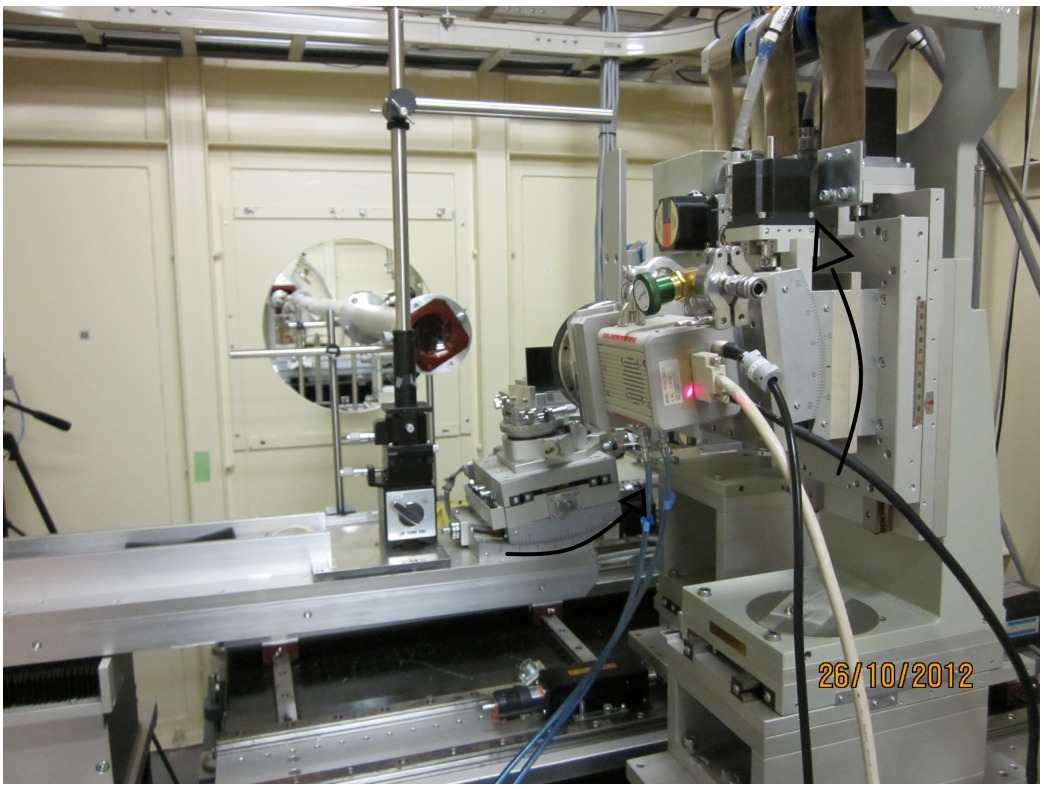

Figure 4.3: Picture displays the optical hutch leading to the monochromator and synchrotron as well as the 8° clockwise inclination about the optical axis parallel to the wavefield propagation direction applied to the object stage and the CCD detector to achieve 2-D phase sensitivity. We apply the inclined geometry method to a Laue ABPCI experimental setup to obtain a 2-D phase gradient, which will be used to reconstruct the δ and β map of the object.

4.2 Procedure

This section concerns the process of data acquisition followed by an explanation on how the data is processed and applied to calculate the phase information.

4.2.1 Data Acquisition

We applied an inclined geometry method proposed by Rutishauser et al [2] for grating interferometry to ABPCI by rotating the sample and detector by 8° clockwise about the optical axis following the x-ray wavefield. By doing this we should achieve a 2-D phase sensitivity with a traditionally 1-D phase sensitivity PCI method as discussed in Section 2.9.9 above. If this method is successful, we should qualitatively observe a high contrast image of a 12.75 mm diameter cylindrical perspex phantom with four cylindrical holes in the top of the phantom, two of which are filled with aluminium and teflon each with a cap on the top, while the other two are left empty, discussed in greater detail in Beltran et al [96]. This is important as imaging this phantom would be nearly invisible using a standard ABPCI setup such as [77] due to the 1-D vertical phase sensitivity of traditional ABPCI methods. This is because the diffraction occurring from vertical interfaces in the phantom when the x-ray wavefield is propagating through it will not be acquired by the detector. If we can produce a high contrast image of this phantom, we then want to quantitatively determine the attenuative and refractive properties of materials present in the phantom, namely the β and δ maps, respectively. The exposure time for all the acquired images and projections was 300ms.

First, data is acquired concerning the distortion that occurs from using the CCD detector. Distortion is due to the deviation of the rectilinear projection of the wavefield as it travels through the fibre optic taper into the CCD chip as shown in Figure 4.1. This is corrected by imaging a precision made grid pattern and used triangulated interpolation to dewarp the image of the warped grid back to the rectilinear grid [97]. In order to account for the background inhomogeneity flat field corrections were applied. Flat field images were taken without the object in the wavefield, with the analyser crystal in a set position. Additionally, dark field images are taken while the incident x-ray wavefield is blocked by a shutter to detect effects caused by the fixed pattern of offsets in the detector i.e dark current. Dark current is corrected by subtracting the average of the dark field images from the data projections. Next, 261 images are taken with no object in the wavefield path and the analyser crystal being rotated about the horizontal axis at 0.1 arcsec around the

Bragg position in order to get reference RCs for the diffracted and transmitted components. Flat field images are taken with fiducial markers to be used as reference points between the transmitted and diffracted images so that they could be precisely aligned with each other, as shown in Figure 5.2. The analyser crystal can be fixed at positions when data is acquired with the sample relative to percent peak intensity of the ratio rocking curve, 5%, 25%, 50%, 80% on either side of the curve for a total of 8 points as observed in Figure 4.4. New flat, dark and CT data images are collected for each of

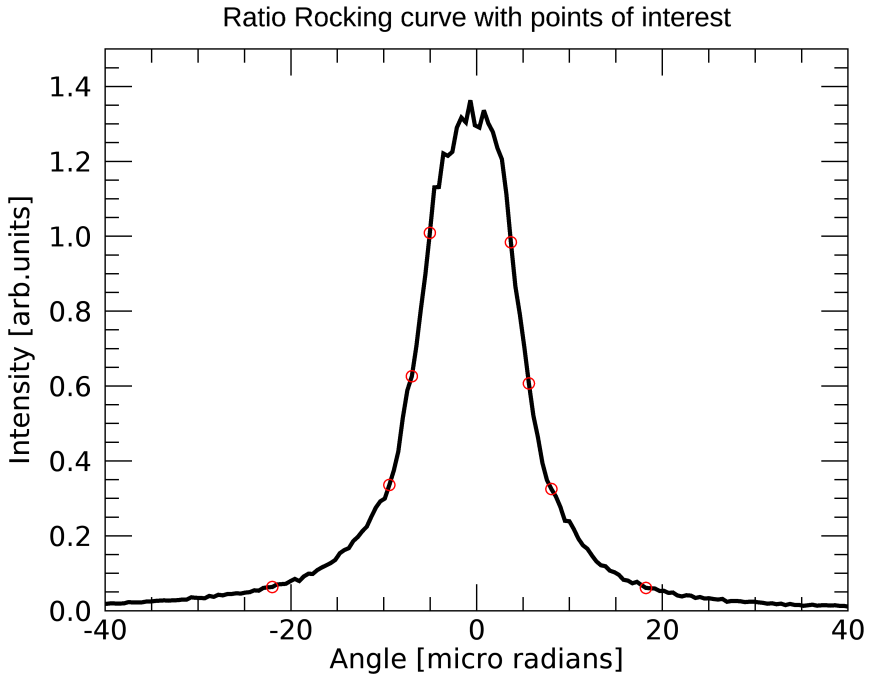

Figure 4.4: Initial points on the ratio rocking curve 5%, 25%, 50%, 80% peak intensity on either side of the curve for a total of 8 red circles where data is collected for each of them. Issues with these initial positions are discussed in Section 6.1

these 8 rocking curve positions mentioned above. We need to collect data from all of these RC positions in order to apply MIR (discussed in Analyser Based Imaging Section 2.9.9), which takes USAXS into consideration. For the applied dual projection Laue geometry method only one data set (i.e., using one fixed position of the analyser crystal) is required, though having multiple means we can choose the data set that gives us the best results.

Chapter 5

Results

This section discusses in detail how the results are obtained from data processing procedures mentioning corrections or any other changes made to the raw data. These include aligning the transmitted and diffracted images using gold foil fiducial markers and fitting the RCs and their ratio with a PearsonVII function (discussed in Section 2.9.9). We then use these fitted RC's to perform phase retrieval using a dual simultaneous inclined Laue geometry method combining methods from [2] and [77]. This will achieve a 2-D phase sensitivity in a traditionally 1-D phase sensitivity method to produce a 2-D phase gradient (discussed in Section 2.9.9). The phase gradient is then integrated using 2-D Fourier integration (discussed in Section 2.4) to produce a phase map. This is then tomographically reconstructed (discussed in Chapter 3) to produce a δ and β maps that allows us to quantitatively reconstruct the refractive index n of materials in the phantom. We also discuss how corrections are determined and applied to the phase retrieval process and how they change qualitatively and quantitatively in the phase, δ and β maps.

5.1 Data Processing

We apply distortion, warping and dark field corrections to the raw data shown in Figure 5.1 and perform alignment of the transmitted and diffracted images. Raw data from the tomographic projections of the perspex phantom have the diffracted image on the left and the transmitted image on the right (see Figure 5.1). The images contain the separation boundary being at an angle due to the 8° inclined geometry. Hence, these images must be carefully separated and aligned, with any Region of Interest (ROI) from one that is not present in the other cut out, otherwise significant errors will arise in later results and procedures.

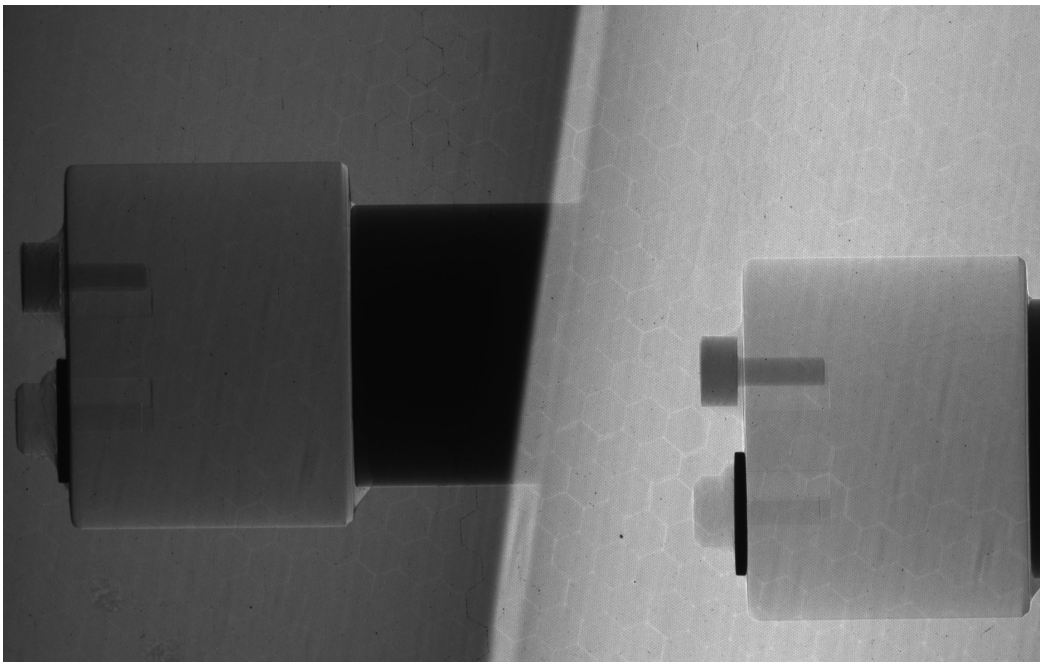

Figure 5.1: Raw data with pixel dimension 2288 × 1448 from the 300th tomographic projection from LHS (Left Hand Side) 50% peak intensity of the RC of the perspex phantom with the diffracted image on the left and the transmitted image on the right. Note how the transmitted image is shifted down and contains less information about the stand, on which the object sat than the diffracted image. The separation boundary is at an 8° angle (due to the 8° inclined geometry). Hence, these images must be carefully separated and aligned, so that for every projection the transmitted and diffracted images precisely overlap.

The next task is separation and alignment of the transmitted and diffracted data for all the gathered projection including when no object was present in the beam. We do this in order to simultaneously compare the two images with each other, in order to apply a Laue phase retrieval method [3] to calculate the phase gradient. This was done by utilizing gold foil fiducial markers as these are materials with high refractive properties and atomic number, meaning they appear dark in all images. The gold foils were placed in set positions shown in Figure 5.2 with no object present in the wavefield. Both the diffracted and transmitted images are present in one image partitioned by a line going through the centre of the image at 8° as observed in Figure 5.3 and thus need to be separated. This was done by finding the middle point

of the image and separating the transmitted and diffracted images into two separate images displayed in Figures 5.4a and 5.4b.

One of the significant merits of using Laue geometry in ABI is to simultaneously produce transmitted and diffracted images. These images can be used to reconstruct the phase gradient using only one set of projections. However, these images must be near perfectly aligned with each other in order to produce an accurate phase gradient map and high quality tomographic reconstructions.

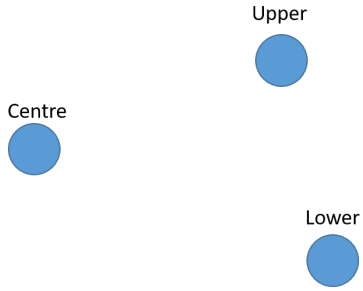

Figure 5.2: The triangular formation of the gold foil circle fiducial markers used to align the transmitted and diffracted images.

In order to accurately align the images the position of the fiducial markers the coordinates of the centre of the circle must be obtained. These have to be precisely determined otherwise artefacts such as smearing and streak artefacts can occur. If these errors are left uncorrected then they will greatly affect further procedures and potentially result in a poor quality reconstructed images. The positions of the fiducial markers in both images were measured in ImageJ [98] by carefully placing a circular ROI over each of the fiducial markers. The positions were then implemented in an adapted IDL code provided by Kitchen et al. [77] (reffered to as Kitchen's method) specifically designed to align the diffracted and transmitted images of Laue geometry ABPCI by stretching, shifting and rotating one of the images to match the other. Once this was done, the transmitted and diffracted images were aligned as seen in Figures 5.5a and 5.5b, respectively. To check that the coordinates of the fiducial markers are accurate and the two images are precisely aligned, the transmitted and diffracted images can be subtracted or divided from each other. This procedure clearly shows any shading or other artefacts caused by the misalignment of the two images as seen in Figures 5.6 and 5.7 below.

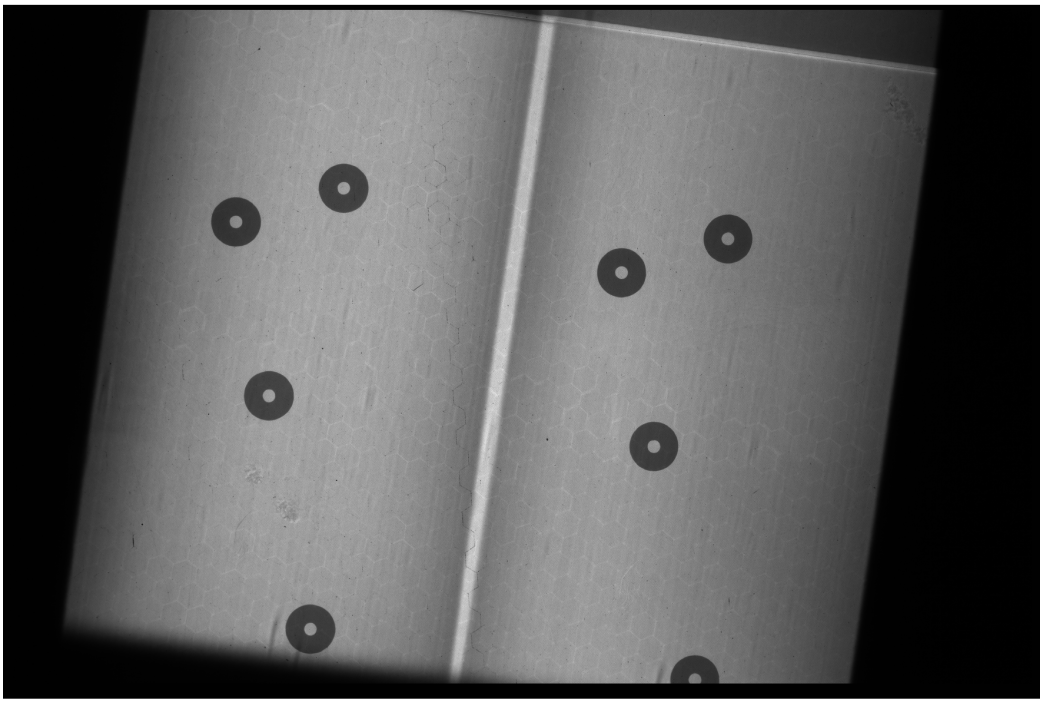

Figure 5.3: Fiducial markers are used for alignment between the transmitted (right) and diffracted (left) sides of the 4000×2672 pixel dimension image.

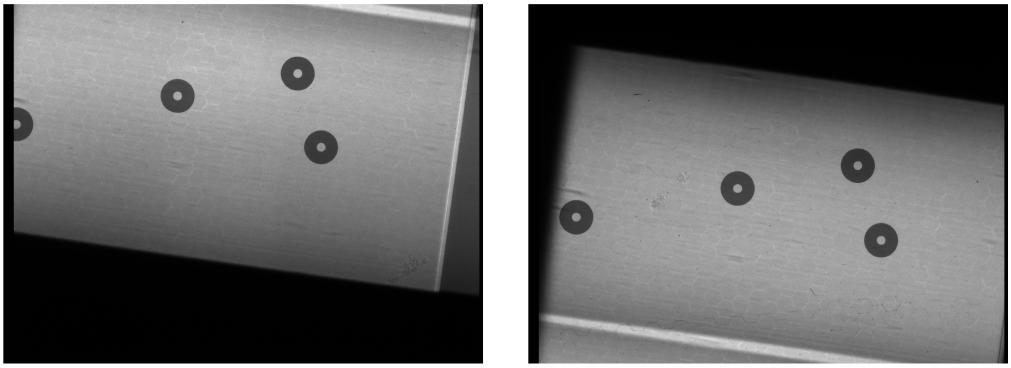

(a) Transmitted image. (b) Diffracted image.

Figure 5.4: Transmitted and diffracted with pixel dimension 2672×2000 images of the fiducial markers whose coordinates in each image must be measured precisely in order to properly align the two images.

The sum of the aligned transmitted and diffracted image helps to check how well the centre points (bright white spots) of the fiducial markers are

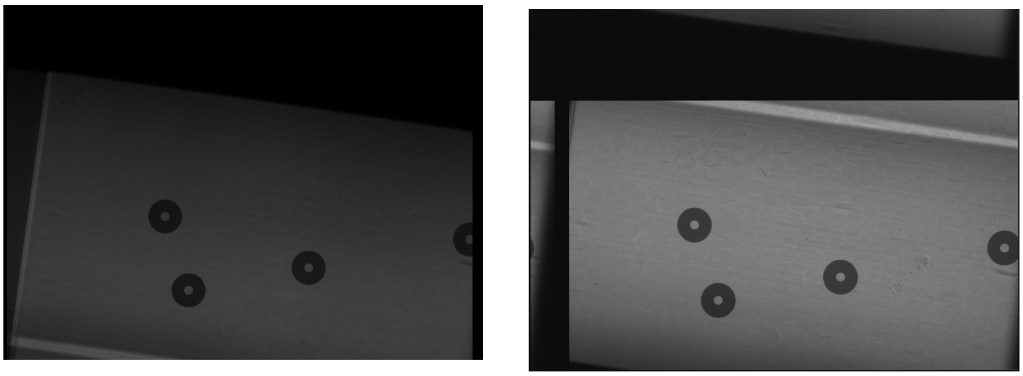

(a) Aligned transmitted image. (b) Aligned diffracted image.

Figure 5.5: Aligned transmitted and diffracted 2672×2000 images of the fiducial markers in order to observe any obvious errors or artifacts caused in the alignment process.

aligned. Ideally they should be on top of each other making only one bright spot visible in each ROI.

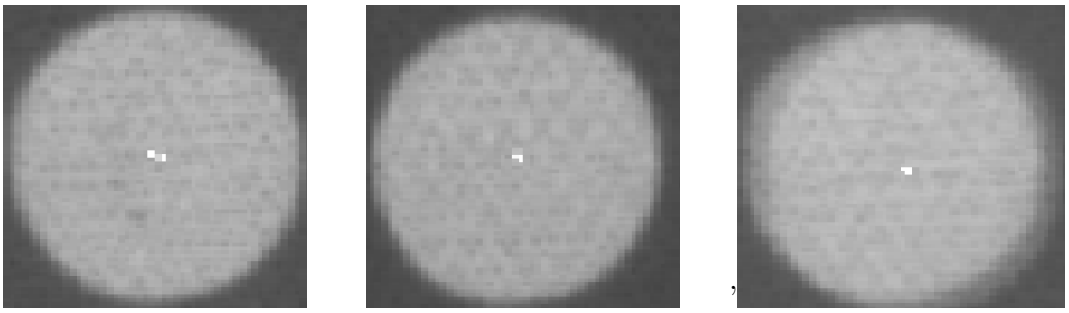

(a) Zoomed in image of upper fiducial marker. (b) Zoomed in image of lower fiducial marker. (c) Zoomed in image of centre fiducial marker.

Figure 5.6: Zoomed in images of the summed aligned diffracted and transmitted images of the fiducial markers with respect to Figure 5.7 looking at how well the centre points are aligned. They ideally should totally overlap each other meaning only one white dot should be observed. Only the centre points in the upper left fiducial marker differ enough to warrant change with the rest being accurately sufficient for this project.

From looking at Figure 5.6, we see that none of them are aligned perfectly with only subfigure 5.6a being sufficiently misaligned to potentially warrant a redo. This process would either require adjusting one of the coordinates

of the diffracted or transmitted images so that they should perfectly overlap with the more centralized point or remeasuring the ROI and adjusting the coordinates in either or both images. One concerning thing is that subfigure 5.6c, we see inner shading within the circle, implying there is a significant mismatch between the two fiducial markers, even though the points look to be perfectly overlapping. This maybe because our alignment process, based on the approach described in Kitchen et al. [77], does not correct for image shearing, like other alignment procedures such as an affine transform.

We can divide the aligned transmitted image by the aligned diffracted image to give a clearer picture of the ROI overlap between the two images as seen in Figure 5.7 below. From this we can observe the clear overlap in the upperleft

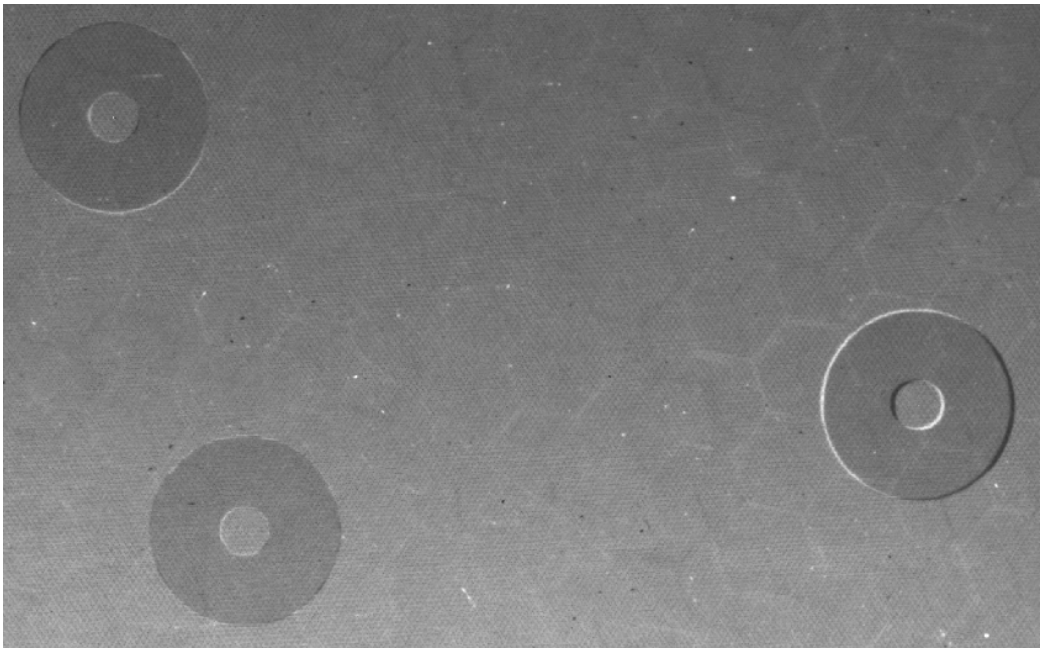

Figure 5.7: Division images of the transmitted and diffracted image showing the overlap of the ROIs as seen by the bright and dark outlines around the upperleft and centre right ROIs. There is a slight mismatch as seen by the banding especially on the RHS (Right Hand Side). This is maybe due to the alignment procedure assuming two points such as the centre points must perfectly overlap with the other points aligned based on this assumption.

and centreright ROIs. Unlike Figure 5.6 here we see that the centre right is the worst aligned as it has the most prominent bright and dark regions around the circle.

5.1.1 Alignment Comparison

As mentioned in the prior section, we can apply a 2-D affine transform to align the transmitted and diffracted images using reference points in the two images such as the fiducial markers. This enables the images to be corrected for shearing, which is not corrected for using the previous method. To see if it is the method causing the misalignment, we trial three different methods using three identical remeasured fiducial marker coordinates in the diffracted and transmitted images. These methods include Kitchen's method applied previously in IDL, an affine transform in Transform Landmark-Correspondence [99] a module for an extension of ImageJ, Fiji [100] and an affine transform using IDL as shown in Figure 5.8 below. The misalignment could also be caused by choosing the wrong centre coordinates of the fiducial markers. This seems more likely as the alignment between the transmitted and diffracted images must be near perfect in order to accurately retrieve a 2-D phase gradient. We can attempt to improve the alignment between the transmitted and diffracted projections by changing the centre points of the fiducial markers in the transmitted and diffracted images. This improvement can be seen in Figure 5.9 when compared to Figure 5.8.
Overall from looking at Figure 5.9 using another set of remeasured coordinates, we see that the fiducial markers blend into the background. This shows that the transmitted and diffracted images are precisely aligned and this is probably the best case we can obtain with our method.

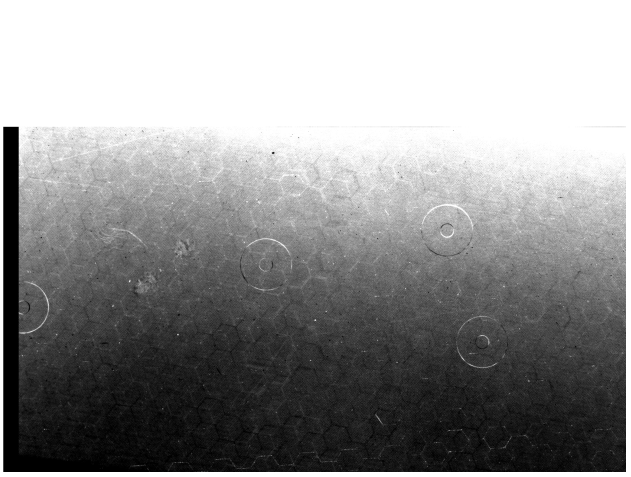

(a) Previously used alignment method designed by Kitchen et al [77] in IDL.

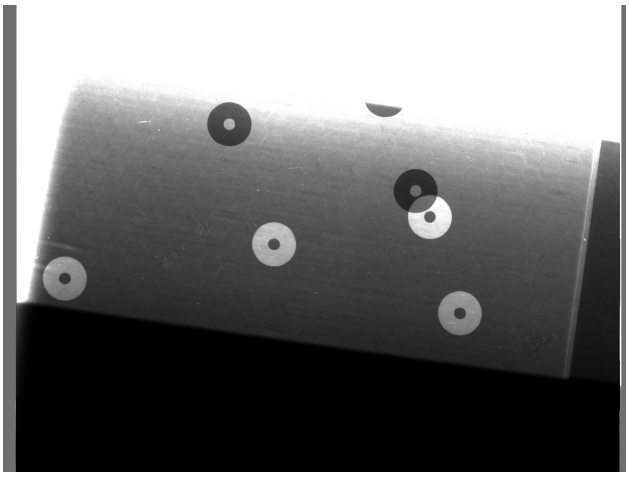

(b) Alignment using an affine transform in IDL.

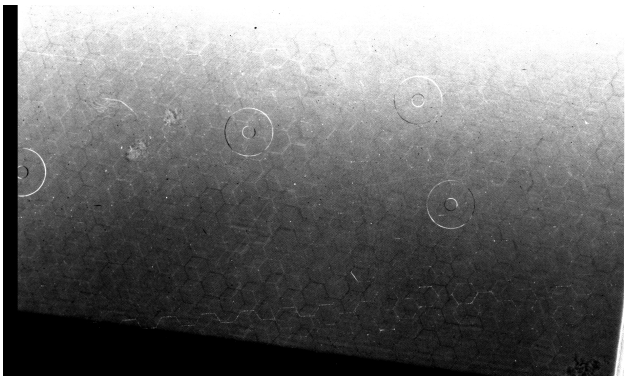

(c) Alignment using an affine transform in Fiji.

Figure 5.8: Alignment using (a) Kitchen's method [77], (b) affine transform in IDL, (c) affine transform in Fiji. Overall the IDL affine transform was extremely unstable while the affine transform using Fiji and the previous method produced similar quality of alignment. Because there is little difference between Kitchen's method and the affine transform using Fiji, we can deduce that there is negligible shearing that has to be corrected for. For simplicity we continue using Kitchens alignment method as there is negligible benefit to changing.

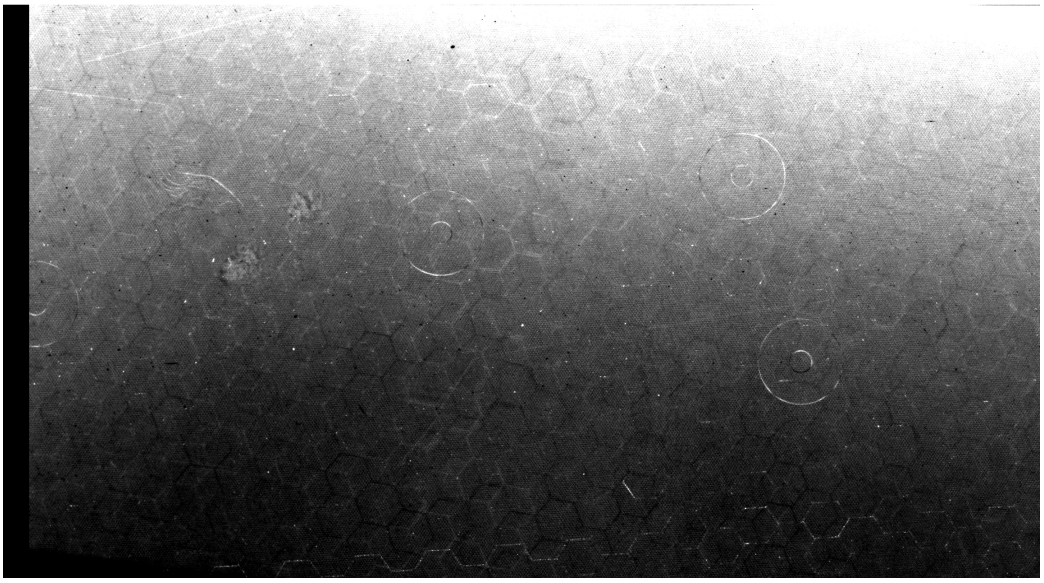

Figure 5.9: Improved alignment of the transmitted and diffracted projections using Kitchens method by adjusting the coordinates of the centres of the fiducial markers in the unaligned transmitted and diffracted images. We can observe the improvement with respect to Figure 5.8 as the markers are less distinct and blend into the background in this image. The markers seem perfectly overlapping with only the lower right fiducial marker looking like it should be adjusted by a pixel in some direction. However, when we attempt to do so the alignment continuously appeared to be worse, which suggests that this is the best alignment we can obtain.

5.2 Fitting the Rocking Curves

The next step was to fit the rocking curves for the diffracted, transmitted and ratio wavefields, whose analytical forms are given by Eqns (2.50), (2.51) and (2.55), respectively. These RCs are fitted for each pixel from the 261 images acquired at the different angular positions of the analyser crystal with no object present in the wavefield propagation path with a Pearson VII function, whose form is given by [93] and shown in Eqn (2.52). As the RCs are

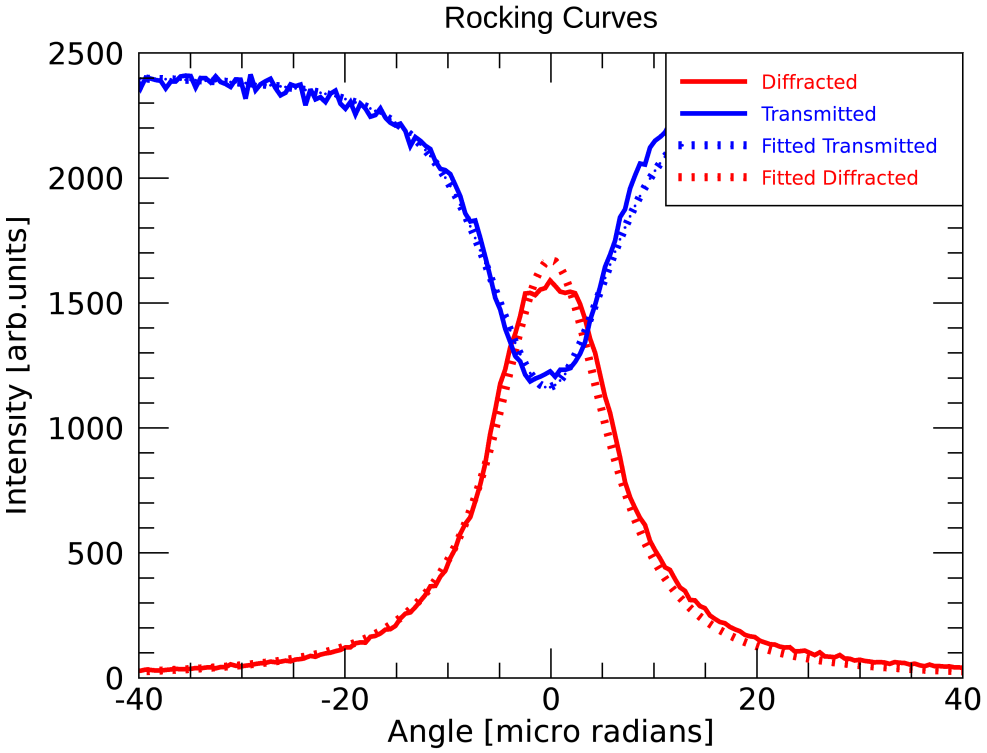

Figure 5.10: Data and fitted transmitted and diffracted single pixel rocking curves that are used to calculate the ratio rocking curve. The ratio RC is defined as the diffracted RC divided by the transmitted RC. The transmitted RC is used to calculate the intensity map, while the ratio RC are used to calculate the $\Delta\theta$ and $\Delta\theta_{180}$ maps whose analytical forms are given by Eqns (2.64) and (2.65), respectively.

fitted for every pixel, the parameters of these fits, discussed in Eqn (2.52), are saved for each pixel in order to be easily accessible for further calculations in other programs. These fitted RCs, shown in Figure 5.10, are used

to measure the change in intensity and angle of incidence upon the analyser crystal of the x-ray wavefield when the object is present in the x-ray wavefield.

After the RCs have been fitted with a PearsonVII function, we performed phase retrieval as observed and discussed in Figure 2.21. These calculations will generate an intensity and two $\Delta\theta$ maps for every projection as observed in Figures 5.11, 5.13 and 5.15, respectively. The intensity maps following

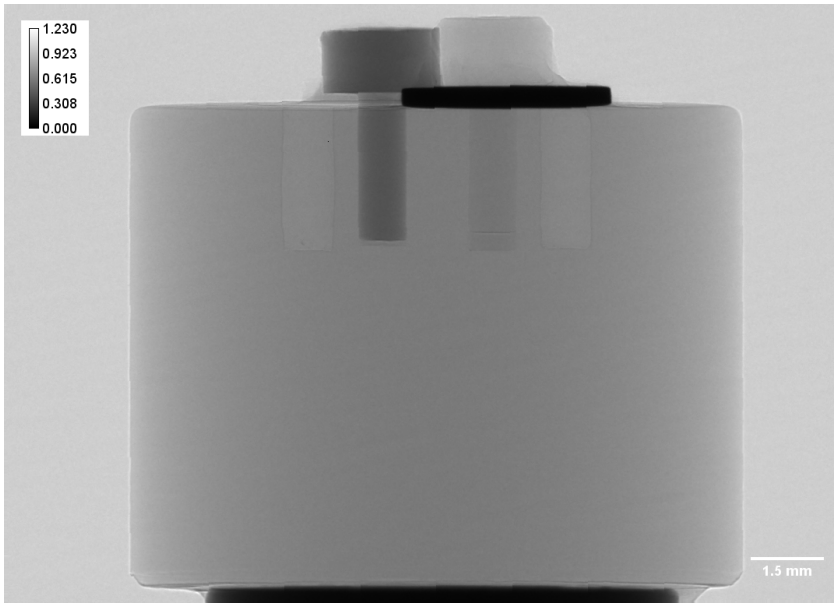

Figure 5.11: Intensity map with pixel dimension 1108×771 and grayscale range [0,1.23] of the perspex phantom calculated from Eqn (2.57) using the transmitted beam as this has a higher intensity. Overall the image shows good contrast with clear distinctions and boundaries between materials in the phantom.

Eqns (2.56) or (2.57) can then be tomographically reconstructed to give the β (absorption) maps as shown in Figure 5.12.

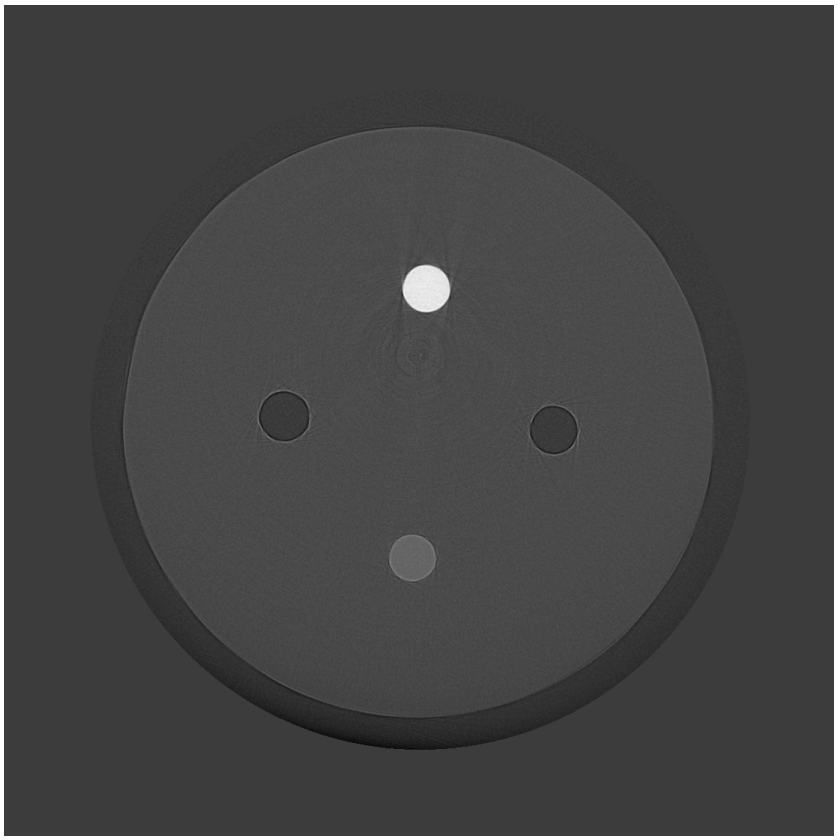

Figure 5.12: Map of calculated β values of the perspex phantom with pixel dimension 1108×1108 and grayscale range $[-5.66 \cdot 10^{-10}, 1.86 \cdot 10^{-9}]$. β values for unique media are shown in Table 5.1. Overall the reconstruction is high quality with high contrast between the perspex (centre circle), aluminium (upper circle), teflon (lower circle) and air (the left, right and outer circles). There are some streak artefacts around the aluminium sample due it possessing a significantly larger (factor of 10) absorption coefficient β than the perspex. The outer circle that is observed in every β and δ map including this one is the air surrounding the phantom.

5.3 Phase Retrieval

First we calculate the shift of the incident angle of the wavefield to obtain $\Delta\theta$ and $\Delta\theta_{180}$ maps from the PearsonVII fit of the ratio RCs by using Eqn (2.60). $\Delta\theta$ and $\Delta\theta_{180}$ are defined as the change in the angle of incidence of the x-ray wavefield upon the analyser crystal for the ϕ and $\phi + 180^0$ projections, respectively, where ϕ is the angular position of the sample about the vertical rotation axis in degrees. Note that $\Delta\theta_{180}$ is referred to as $\Delta\hat{\theta}'$

in the referenced equations. $\Delta\theta$ and $\Delta\theta_{180}$ are given by Eqns (2.64) and (2.65), respectively, with relation to the phase gradient given by Eqns (2.62) and (2.63) for the ϕ and $\phi + 180°$. We then flip the $\phi + 180°$ projection about the vertical axis and shift it so that it precisely overlaps with the ϕ projection prior to calculating $\Delta\theta_{180}$ to obtain Figures 5.13 and 5.15 of the calculated $\Delta\theta$ and $\Delta\theta_{180}$ maps, respectively. The application of inclined geometry, discussed in Figure 2.23, allowed us to combine the two $\Delta\theta$ images from opposing directions to produce both components of the phase gradient vector Eqns (2.71) and (2.73) (discussed in Section 2.9.9), which is integrated into the phase map. We then shift both of these images so that they are in the centre of the image to make truncation easier.

It is important to note looking at Figures 5.13 and 5.15 that the bright areas show a shift up the ratio RC, while the dark areas show a shift down, respectively, from our chosen starting point on the ratio RC. The change in magnitude tells one how much it is refracted in the diffraction plane governed by the refractive index decrement and shape of the object.
To quantitatively check the $\Delta\theta$ and $\Delta\theta_{180}$ maps, we plot the yellow ROI going through the phantom measuring the $\Delta\theta$ values observed in Figures 5.14 and 5.16, respectively.
At this point we carry on to see if the underestimation of the positive phase gradients negatively impacts the resultant images of the δ function, as it could be that our theoretical starting point on the rocking curve does not coincide with the experimental one (discussed in Section 5.4).

We then calculate the vertical and horizontal phase gradient components g_y and g_x, respectively, shown in Figures 5.17 and 5.19. g_y and g_x are given by Eqns (2.71) and (2.73), respectively. The yellow line in Figures 5.17 and 5.19 are ROIs plotted in Figures 5.18 and 5.20, respectively.
Figure 5.17 should be near invisible as the phase gradients from the vertical interfaces cancel as the yellow line travels across the phantom through the media present in the holes of the phantom. This due to how g_x is calculated following Eqn (2.55), because the phase gradients on the vertical edges of the phantom have opposing magnitudes for $\Delta\theta$ and $\Delta\theta_{180}$ as shown in Figures 5.14 and 5.16, respectively. Hence when the vertical edges of the phantom in the $\Delta\theta$ maps are added they cancel. This is desired as to obtain the phase gradient in one direction the orthogonal components must cancel. We see that the values are close to zero with some discrepancies, most notably interface of the far right edge of the phantom. These discrepancies indicate a misalignment between the two $\Delta\theta$ maps during the flip and shift of the $\Delta\theta_{180}$ projection rather than the underestimation of the positive phase gra-

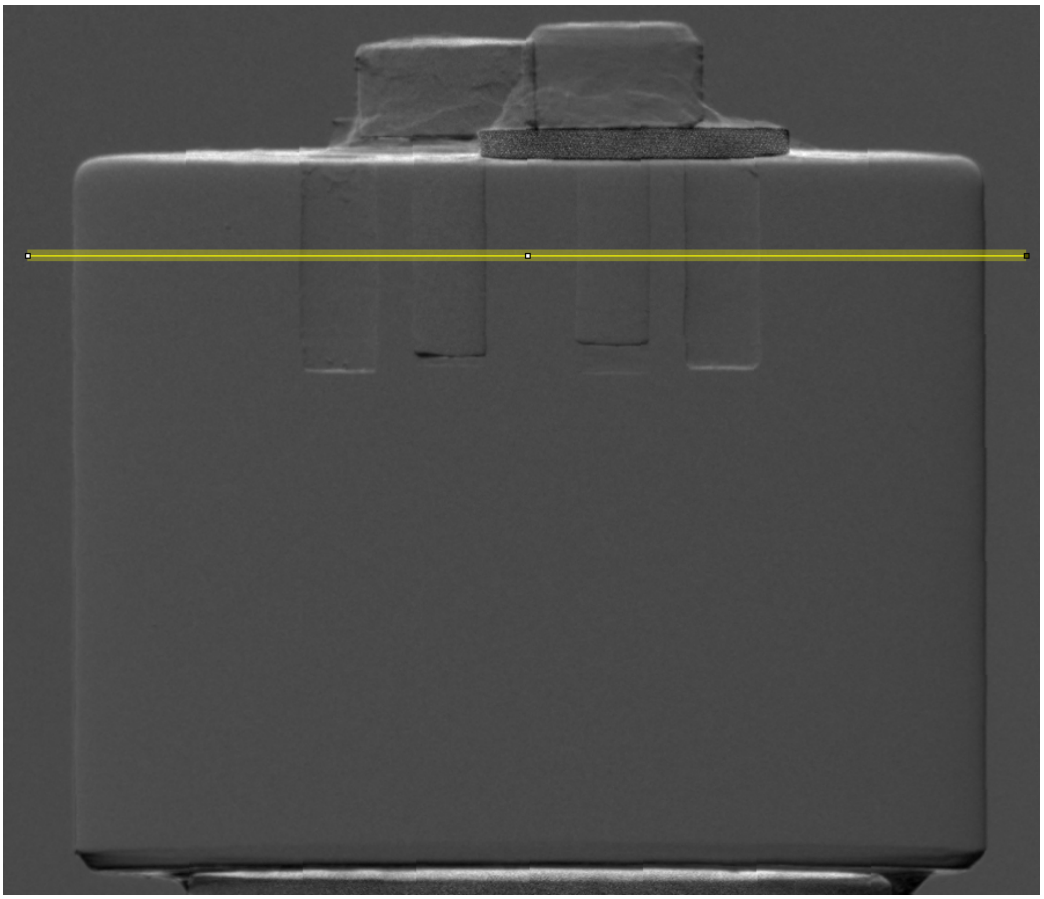

Figure 5.13: $\Delta\theta$ map with pixel dimension 900×771 and grayscale range $[-4.76 \cdot 10^{-6}, 1.23 \cdot 10^{-5}]$ radians of the perspex phantom calculated from the shift in the rocking curve position when an object is placed in the beam. This image shows clear distinction of boundaries and interfaces between materials present in the phantom. It is important to note from looking at this image that the bright areas show a shift up the rocking curve, while the dark shows a shift down the rocking curve. The refractive index of a material is given by the magnitude of the change rather than its direction with respect to the rocking curve. The horizontal yellow line is a ROI that is plotted in Figure 5.14.

dient previously discussed.

The additional information gathered from the g_x and g_y maps (Figures 5.17 and 5.19, respectively) are then integrated using 2-D Fourier integration given by Eqn (2.7) to retrieve the phase map as shown in Figures 5.21.

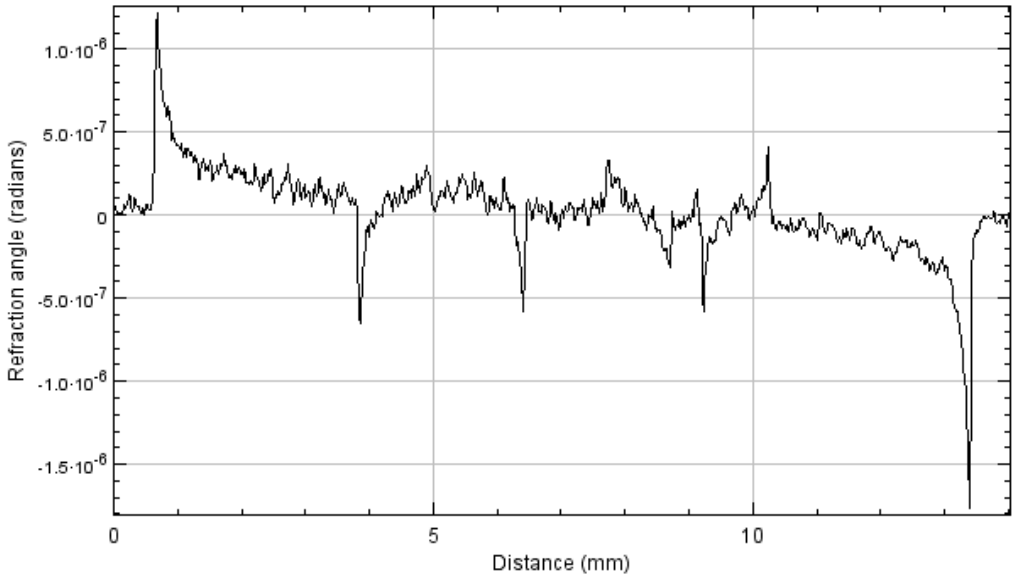

Figure 5.14: Plot of the yellow line through the perspex phantom in Figure 5.13 of the $\Delta\theta$ map showing the $\Delta\theta$ values throughout the phantoms cross section. Most noticeable are the peaks and troughs corresponding to the x-ray wavefield at the left and right sides of the phantom. The one concerning thing is the fact that the magnitude of the positive peak as the x-ray wavefield at the left side of the phantom is approximately 2/3rds the magnitude of the negative peak at the left side of the phantom. At the position on the rocking curve we are working on these should be identical and the underestimation of the phase gradients also appears to occur with the media in the holes of the phantom.

The phase maps then undergoes 180° CT reconstruction to give the δ maps as shown in Figure 5.22.
The application of the inclined geometry to ABI produced high quality phase and intensity images observable in Figures 5.11 and 5.21, respectively. As seen in Table 5.1 below, the computed values for β excluding teflon are close to the theoretical values.

Figure 5.15: $\Delta\theta_{180}$ map with pixel dimension 900×771 and grayscale range $[-4.94 \cdot 10^{-6}, 1.31 \cdot 10^{-5}]$ radians of the perspex phantom calculated from the shift in the rocking curve position when an object is placed in the beam. This is flipped about the vertical axis and aligned with the $\Delta\theta$ map so that they precisely overlap before being shifted into the centre. The horizontal yellow line is a ROI that is plotted in Figure 5.16.

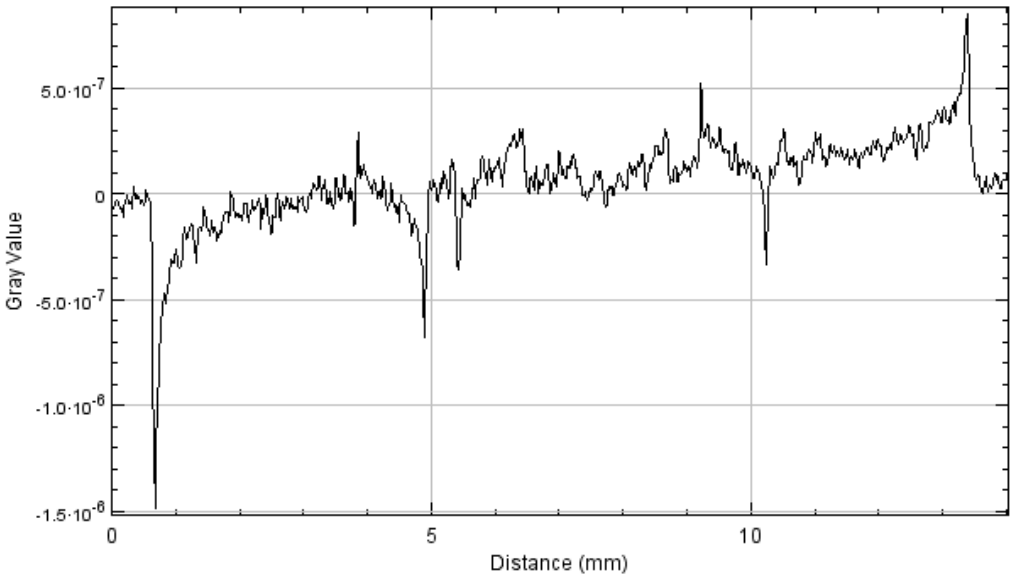

Figure 5.16: Plot of the yellow line through the phantom in Figure 5.15 of the $\Delta\theta_{180}$ map showing the $\Delta\theta$ values throughout the phantom. This is very similar to a reverse of Figure 5.14, bar the behaviour of the media in the holes, which have very sharp and narrow troughs. The underestimation of the positive phase gradient discussed in Figure 5.14 is also present in this image. Interestingly there are only three positive and negative peaks for the holes in this figure but four in Figure 5.14. This is most likely due to the two $\Delta\theta$ maps containing different information but it could also suggest the underestimation of the phase gradients is getting worse as the projections are acquired or in the calculation of the $\Delta\theta_{180}$ map.

Figure 5.17: g_x map with pixel dimension 900×771 and grayscale range $[-1.21 \cdot 10^{-5}, 4.81 \cdot 10^{-6}]$ radians, phase gradient in the vertical (x) direction of the perspex phantom calculated from the two $\Delta\theta$ maps (Figures 5.13 and 5.15) as shown in Eqn (2.71). It is observed that the phantom is nearly invisible in this image with only the horizontal media interfaces being distinct confirmed by the yellow ROI plotted in Figure 5.18. This is the only phase gradient image we would have to calculate the phase map of if we did not apply the inclined geometry to this Laue ABPCI setup.

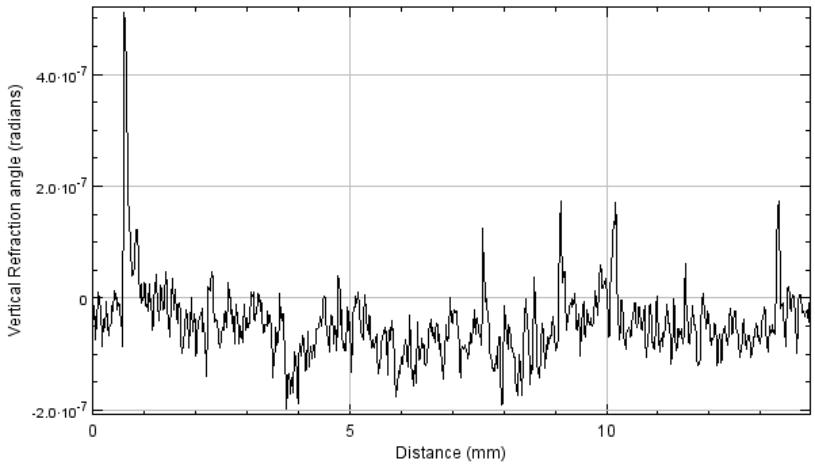

Figure 5.18: Plot of the yellow line travelling across the phantom through the media present in the holes of the phantom in the g_x map. We see that the values are mostly close to zero with some discrepancies most notably the far right edge of the phantom. These discrepancies indicate a misalignment between the two $\Delta\theta$ maps.

	β_{Theo}	β_{Mea}	δ_{Theo}	δ_{Mea}
AL	$1.7 \cdot 10^{-9}$	$1.6 \pm 0.1 \cdot 10^{-9}$	$8.0 \cdot 10^{-7}$	$4.2 \pm 0.1 \cdot 10^{-7}$
Perspex	$1.6 \cdot 10^{-10}$	$1.5 \pm 0.3 \cdot 10^{-10}$	$3.9 \cdot 10^{-7}$	$1.9 \pm 0.1 \cdot 10^{-7}$
PTFE	$2.5 \cdot 10^{-10}$	$4.0 \pm 0.3 \cdot 10^{-10}$	$6.5 \cdot 10^{-7}$	$4.0 \pm 0.1 \cdot 10^{-7}$

Table 5.1: Comparison between the theoretical values obtained from [111] and the measured values obtained from the reconstructions observed in Figures 5.12 and 5.22 for the absorptive and refractive coefficients β and δ respectively. These reconstructions were obtained following the procedure discussed in the previous section. The measured values of δ are approximately a factor of two off the theoretical values. Potential reasons for the poor results are discussed in Section 6.1. The uncertainties of the measured values are the standard deviation when measuring the values over a circular region. These circular regions taken from the slice of the pins for aluminium and teflon, respectively. For perspex a similar size circular region is taken in the centre of the phantom.

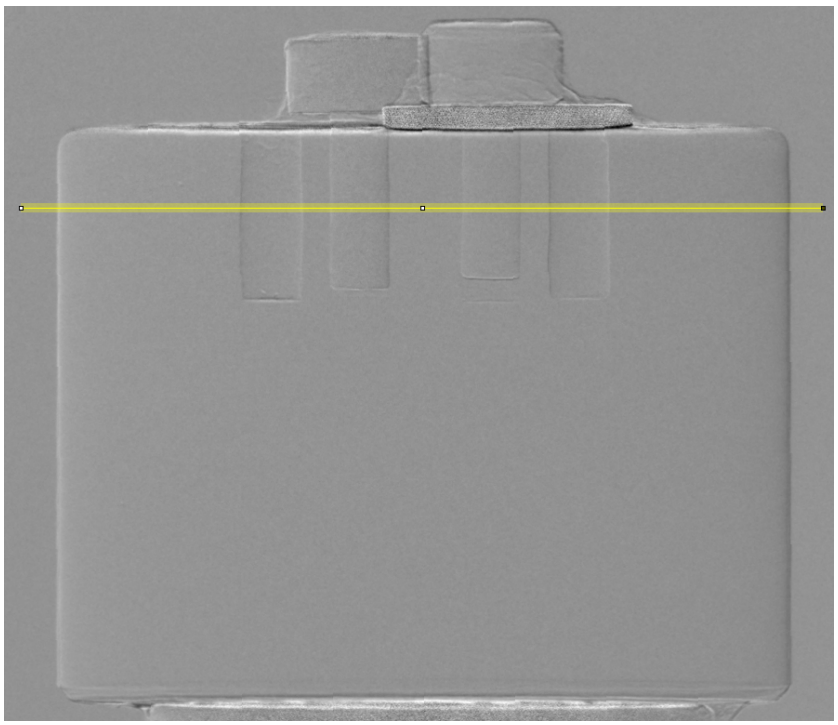

Figure 5.19: g_y map with pixel dimension 900×771 and grayscale range $[-1,77 \cdot 10^{-5}$,$1.29 \cdot 10^{-5}]$ radians, phase gradient in the horizontal (y) direction of the perspex phantom calculated from the two $\Delta\theta$ maps (Figures 5.13 and 5.15) as shown in Eqn (2.73) with a yellow line traveling across the phantom through the holes Figure 5.20. This is the horizontal gradient that we would miss without applying the inclined geometry to the Laue ABPCI setup. We can, using the additional information gathered from this projection and Figure 5.17, apply 2-D integration to retrieve a phase map of the object.

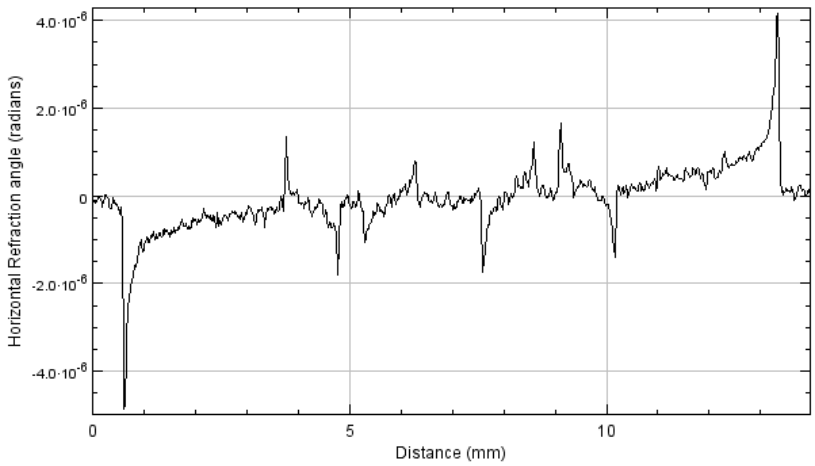

Figure 5.20: Plot of the yellow line travelling across the phantom through the media present in the holes of the phantom in the g_y map. We see relatively even magnitudes of the peaks and troughs along with the expected and stable trend as the x-ray wavefield propagates through the phantom. However, this is because the amplitudes are the result of subtracting the positive gradient with the negative gradient as described by Eqn (2.73). The underestimation of the positive phase gradient observed in Figures 5.14 and 5.16 will result in an underestimation of all the phase gradients present in this image. This could in turn result in underestimation of the phase and δ values of the media present in the phantom.

Figure 5.21: Phase map with pixel dimension 1108×771 and grayscale range $[-314.78, 31.80]$ radians, of the perspex phantom calculated from the 2-D Fourier integration of the horizontal and vertical components of the phase gradient. There is a clear contrast between the interfaces of the different materials in the phantom. However, there is a lot of smearing due to the large contrast in refractive index between some of the materials and air. This smearing is seen and bright and dark shading around interfaces such as the tops of the phantom and around the left and right surface of the phantom.

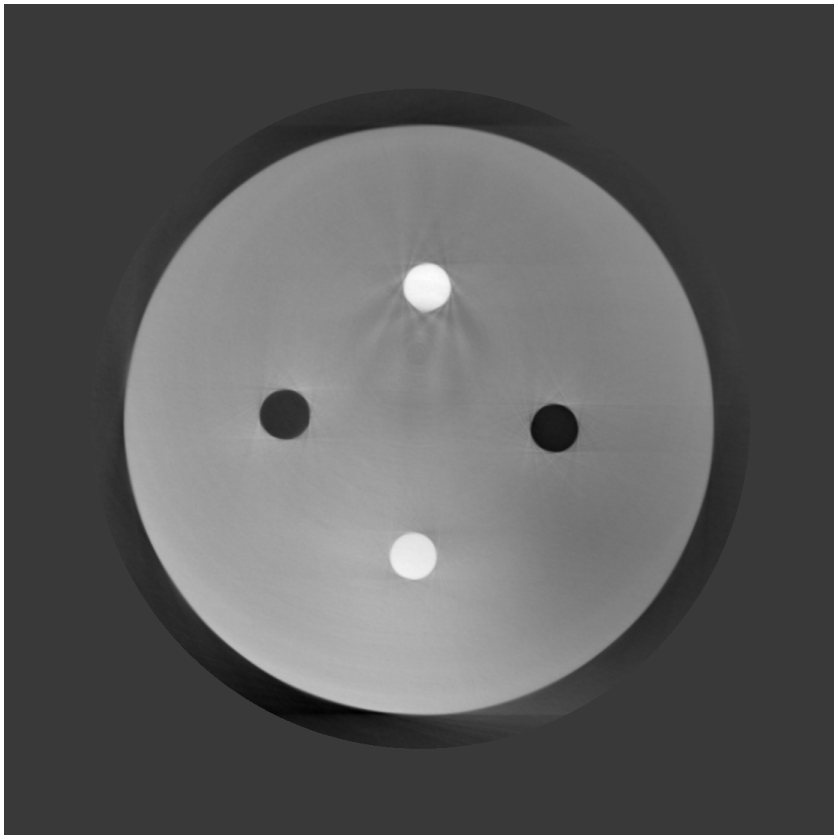

Figure 5.22: Slice of the δ map with pixel dimension 1108×1108 and grayscale range $[-12.52 \cdot 10^{-8}, 4.36 \cdot 10^{-7}]$, calculated from 180° tomographic reconstruction of the phase maps. There is clear contrast between the perspex phantom and the aluminium pin (top white circle), teflon pin (bottom light grey circle) and air (side circles and surroundings, black), encouraging us to take quantitative measurements of the refractive index of the materials displayed in Table 5.1. There are streak artefacts present in the image, especially around the aluminium pin, due to the relatively large difference in refractive index with respect to the perspex phantom. There are bright and dark regions around the sample concentrated around the media interfaces that is most likely due to the bleeding observed in Figure 5.21.

5.4 Analysis

This section covers in detail all of the corrections applied, while performing analysis of raw and processed data. These corrections arise from the GOA, the mechanical and thermal stability of the analyser crystal and the application of inclined geometry to ABPCI.

5.4.1 Shift and Rotation

We mentioned earlier that the object simultaneously shifts and rotates with respect to Figure 5.1 over the 3600 projections for all the measured RC points. We can take a projection of the raw data, as shown in Figure 5.23, and calculate the magnitude of the rotation. The angle between the horizontal line

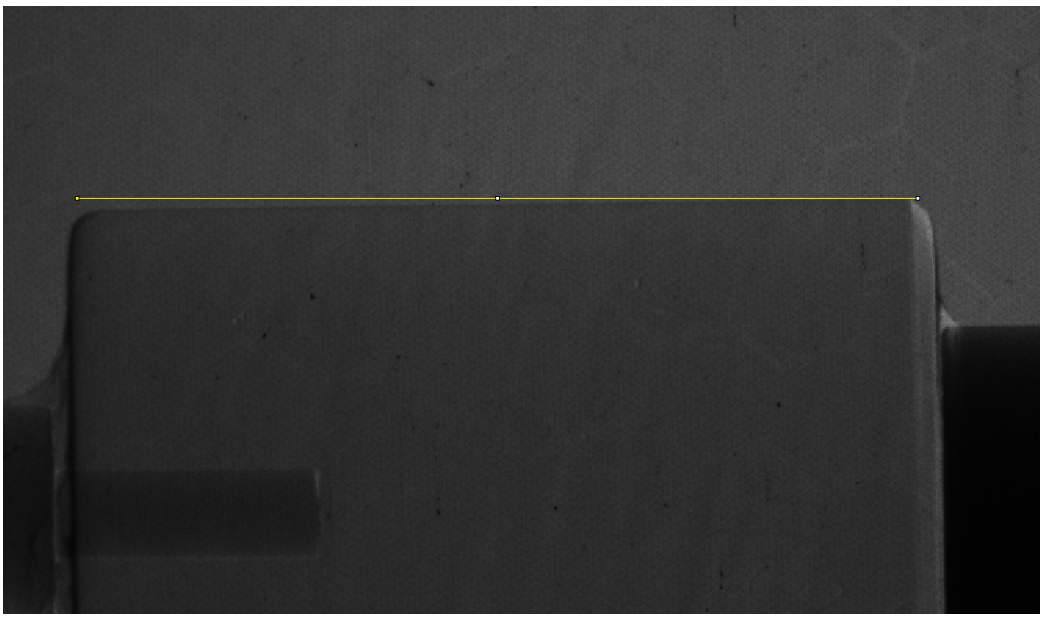

Figure 5.23: Magnified projection of a raw 50% peak intensity position, tomographic projection showing the surface of the phantom at an angle with respect to the yellow horizontal line. We calculated this angle to be 0.752° and we can see in Figures 5.25a and 5.25b that this angle changes throughout the projections.

was calculated to be 0.752°. This angle is small but is quite significant for this type of work and could cause some artefacts occuring in following images. This angle might be due to the object and detector not being aligned precisely and even then this would be corrected by a single rotation for all the projections. We can check for this by taking a point in a projection of

the inclined object and compare it to the same point in its respective 180° projection as shown in Figure 5.24.

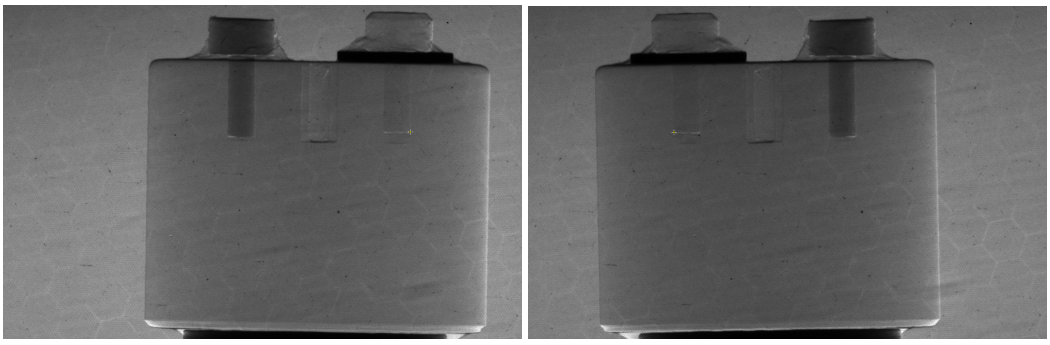

(a) Tomographic projection 61 of the diffracted data.

(b) Tomographic projection 1861 of the diffracted data.

Figure 5.24: Analysing the alignment between the detector and object by taking a point in two opposing projections and observing if its vertical position has changed. In this case the point has the same vertical position in both images of $y = 291$. This means that the detector and object's axis of rotation are precisely aligned.

We also see a shift in the position of the phantom in the raw images as shown in Figures 5.25a and 5.25b. We can measure this shift by using a line as a reference point and measuring the distance between the reference point and a particular point on the phantom for the two extremities projections. Performing this calculation we find that the projections shift 81 pixels either direction due to the centre of the sample not being at the centre of rotation.

Even if the object in the projections shifts and rotates it can still undergo CT reconstruction to produce β and δ maps with minimal impact. The only issue is if the angle of rotation of a projection and its respective flipped 180° projection are different. We can see this is not the case as there would be misalignment between the two $\Delta\theta$ maps, which would be observable in the g_x and g_y maps. CT reconstructions confirm that the two $\Delta\theta$ maps have the same degree of rotation and correcting for this rotation may cause additional errors. This is because it adds another process that has to be done precisely in order for the phase gradients to be accurately obtained. The images are shifted to the centre in order to be easily truncated as this doesn't need to be done precisely so long as the two $\Delta\theta$ maps are already aligned.

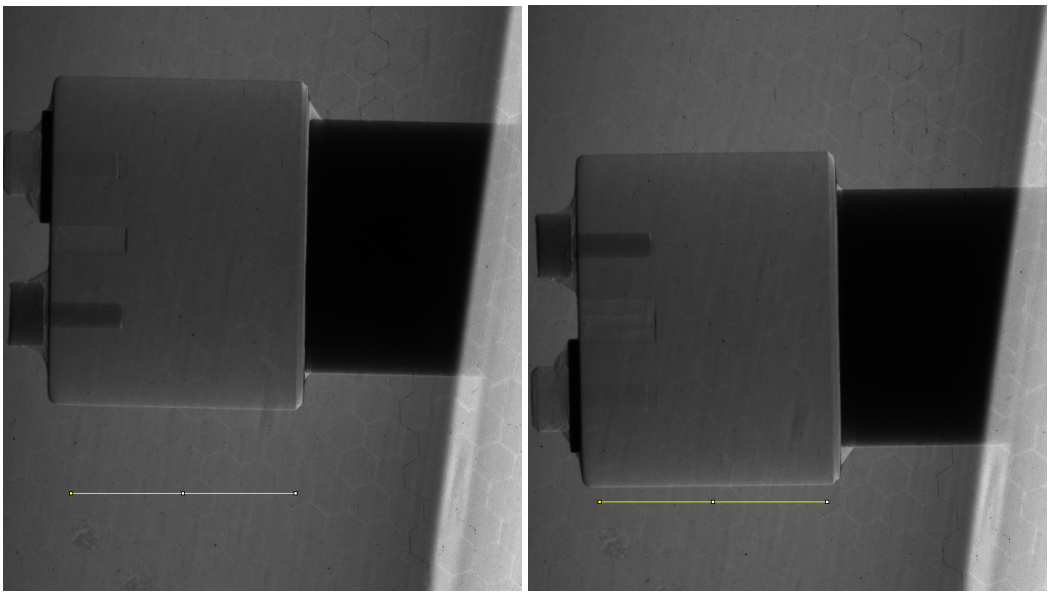

(a) Tomographic projection 343 of the raw data.

(b) Tomographic projection 2143 of the raw data.

Figure 5.25: Projections of the diffracted raw data at tomographic projection number a and $a + 1800$. These two images show the clear change in the position of the phantom as the tomographic projections are gathered.

5.4.2 Analyser Crystal Alignment and Stability

The ABPCI setup requires methodical and precise alignment of all of its components, most crucially the analyser crystal. The Bragg angular window is of the order of 40 microradians either direction when taking phantom data projections with the analyser crystal rotated about the horizontal axis on a starting point on the rocking curve e.g. 50% peak intensity. This very narrow angular window makes the analyser crystal setup very sensitive to any misalignments. Furthermore, any kind of mechanical instability of the stage holding the object or the crystal itself as well as heating of the crystal can cause this angular position of the analyser crystal to drift over time. This drift will cause the phase gradients to be over or underestimated, depending on the direction of the drift and the phase gradients. We need to check what the actual position of the analyser crystal was when the projections were taken. We can achieve this by comparing the values of the ratio flat field image, which is the diffracted flat field image divided by the transmitted flat field image, shown in Figure 5.26a, to the amplitude of the fitted rocking curve, c, defined in Eqn (2.52) and shown in Figure 5.26b.

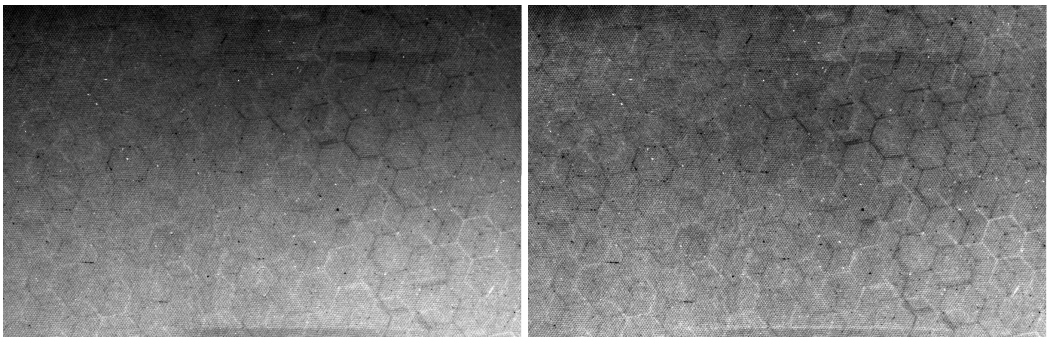

(a) Flat field ratio. (b) Fitted amplitude of the RC c.

Figure 5.26: Ratio flat field and fitted RC amplitude at RC starting point 50% peak intensity. Theoretically the flat field ratio should be half the value of the fitted amplitude, c, for every pixel in the image. This means that they should look identical to each other in their own palette.

For projections taken at the 50% peak intensity of the rocking curve we expect the ratio flat field values to be half the amplitude of the fitted rocking curve. To make this contrast clear we can divide the fitted amplitude, c, by the ratio flat field at the 50% peak intensity. This should result in a uniform image of values approximately equal to two (see Figure 5.27). We see that this is not the case and in fact looking at the area it is on average approximately equal to four meaning that the ratio flat field is half the value, which it should be. This means that the experimental point on the rocking curve is half the theoretically expected one and closer to the 25% peak intensity point. Surprisingly, this should not make much difference as our method utilizes the ratio of the transmitted and diffracted wavefield. This means all of our data including the flat field will start at this point. The only difference it makes is that we are closer to the tails of the curve rather than the straight slope meaning the contrast might be worse due to the smaller change in intensity for the same change in angle.

We can also analyse the mechanical stability of the analyser crystal by taking the mean of an identical air, which is a ROI away from the sample, in the transmitted and diffracted images over the 3600 projections. The data is shown in Figures 5.28a and 5.28b below, where we see that the diffracted beam intensity decreases, while the transmitted beam intensity fluctuates with a square bump around the centre. This is a strange behaviour for the transmitted beam intensity as we expect that if the diffracted beam de-

Figure 5.27: Projection of the amplitude of the fitted RC, c, divided by ratio flat field for the Minus 50% peak intensity point on the rocking curve to determine the actual starting point on the rocking curve. This was achieved by taking a small ROI in air given by the yellow box in the top left corner of the image and measuring the mean, min and max values contained. Theoretically the mean value should be half the peak intensity as desired but as we can see it is closer to 4. This means we are sitting at approximately 25% of the peak intensity.

creases then the transmitted beam will increase. The ratio decreases, which is confirmed in Figure 5.29. This implies that the analyser crystal is moving or under thermal strain causing the ratio to drift over time. This thermal strain maybe caused by heating due to energy imparted by the x-ray wavefield as it interacts with the crystal. This causes the distance between the crystallographic planes of the crystal to increase under significant thermal heating, which in turn shifts the Bragg window following Eqn (2.48). For the monochromator (discussed in Section 2.2), thermal strain due to the large thermal flux from the high intensity x-ray wavefield is a major issue and needs to be cooled using water or another coolant. Once the beam passes through the monochromator the outgoing intensity is mere fraction of the incident one. Hence, the analyser crystal heating up enough to cause this magnitude of ratio drift seems very unlikely. Also the heating of the analyser

crystal would produce a drift in the opposite direction, because the Bragg angle decreases with heating. Thus the entire rocking curve will be shifted to the left, which would increase the diffracted intensity. However, Figure 5.29 clearly shows the decrease of the diffracted intensity.

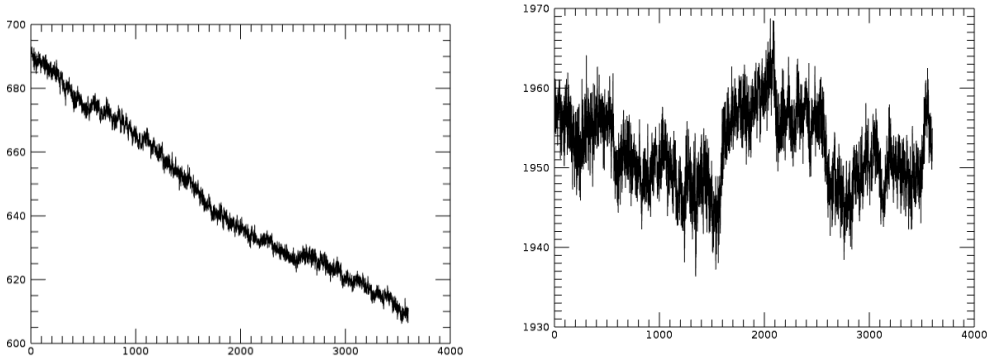

(a) Mean of air ROI in the diffracted beam over 3600 projections.

(b) Mean of air ROI in the transmitted beam over 3600 projections.

Figure 5.28: Mean of an air ROI over the acquired 3600 projections with the sample in the beam shows a steady decrease in the diffracted image while a relatively consistent value in the transmitted image. We would suspect that if the refracted intensity was decreasing, the transmitted intensity would increase to compensate. This would keep the ratio identical and suggest that the analyser crystal is rotating about the vertical and optical axes during the scanning.

We could potentially explain this odd behaviour in the transmitted and diffracted wavefield over 3600 projections observed in Figures 5.28a and 5.28b if the slope of the transmitted and diffracted rocking curves for the same ROI are significantly different. This is examined by plotting the mean transmitted and diffracted rocking curves for the same air ROI in Figure 5.29.

We would expect that the unusual trend from the transmitted wavefield in Figure 5.28b could be due to thickness oscillations but these are not observed in Figure 5.29 of the transmitted RC. From this we can then calculate the trend of the ratio that is the diffracted projection over the transmitted projection as shown in Figure 5.30.
To emphasise the difference this makes, we have Figure 5.31 of the difference between a phase map with and without the ratio shift correction applied to

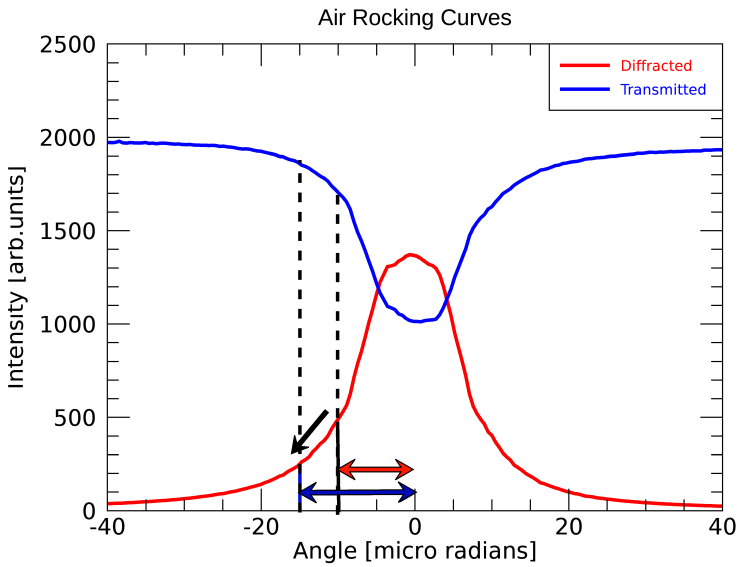

Figure 5.29: Mean transmitted and diffracted rocking curves for an identical air ROI in Figures 5.28a and 5.28b.Our working point is the black line located at 25% peak intensity of the ratio RC. From our working point, we have a shift in the magnitude of the intensity shift appears to be similar for the diffracted and the transmitted. This contradicts with the trends in the diffracted and transmitted intensities observed in Figures 5.28a and 5.28b.

the calculation of the two $\Delta\theta$ maps. The ratio drift is calculated by taking the mean of a small area in air in the flat field ratio and data ratio images and dividing them. This ratio drift is then multiplied to the ratio (I_D/I_T) during the phase retrieval process to calculate the $\Delta\theta$ maps. This is done before calculating the directional phase gradients and performing 2-D Fourier integration.

We can observe from the contrast present in Figure 5.31 the ratio correction changes the phase map inhomogeneously. It has a bright and dark spot at the top left and right corners of the image, respectively with similar gray spots at the bottom corners of the image. These spots seem to smear into the remaining parts of the image changing its grayscale value. We can observe the magnitude of this correction by looking at the plots of the upper and lower yellow line ROI in Figures 5.32 and 5.33, respectively.

We see from Figure 5.32 there is a steady linear trend of the grayscale value decreasing as the line propagates through the air above the phantom. We could predict that in Figure 5.33 this linear trend will be similar but have spikes in the middle from propagating through the media present in the holes

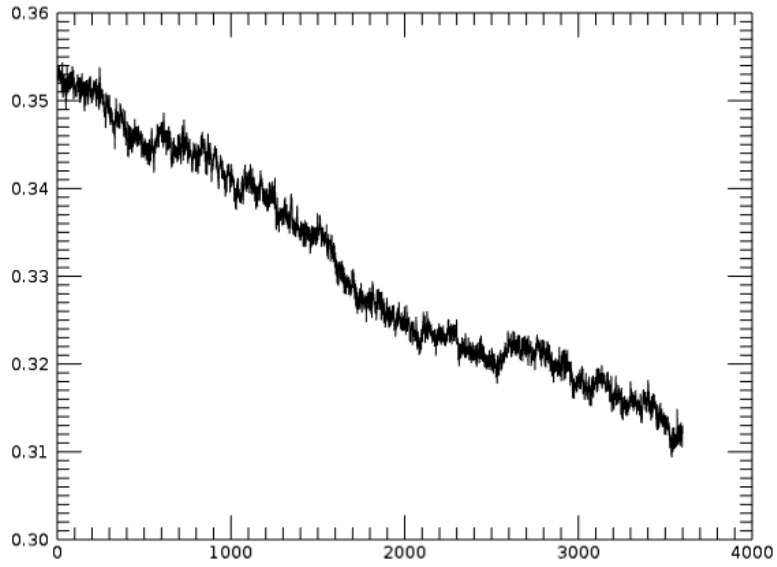

Figure 5.30: Ratio intensity of the air ROI over the scanning of 3600 projections with the sample present in the beam. We see a steady decrease in the ratio intensity, which emphasises that the analyser crystal is moving during the experiment. This is not ideal as this causes the phase gradients moving down the ratio rocking curve to be overestimated, while the phase gradients moving up the ratio rocking curve are underestimated by a factor of $1 - 0.31/0.35 = 0.114 = 11.4\%$ from values in this figure. This could cause significant errors in later images especially when trying to take quantitative measurements such as Table 5.1.

of the phantom. However, it is unlikely as the ratio drift is calculated from the change in the ratio of air surrounding the phantom. If this does occur it suggests an error has occurred most likely with the phantom moving into the ROI set to measure the ratio drift.
We can then perform CT reconstruction on phase maps with the ratio drift correction applied during the phase retrieval process to give the δ map in Figure 5.34, with a yellow ROI, which is plotted in Figure 5.35. We see from Figure 5.35 that the ratio drift has a minor decrease in the measured δ values. As we currently have an overall large source of error that is approximately equal to two, we cannot say if this change is correct or not. In this case because it hinders our results with no clear way to confirm if its correct, we do not apply it in the final results shown in Table 5.2.
We can also take different areas of air in the image and look for the same ratio drift behaviour. We chose to take the areas near the four corners of

Figure 5.31: Calculated map of the difference between a phase map with and without the ratio shift correction applied to the calculation of the two $\Delta\theta$ maps at rocking curve position 50% peak intensity projection 61. As it can be seen from the contrast present in the image, the ratio correction changes the phase map inhomogeneously. It has a bright and dark spot at the top left and right respectively with similar gray spots at the bottom corners of the image. We can observe the magnitude of this correction by looking at the plots of the upper and lower yellow line ROI in Figures 5.32 and 5.33, respectively.

the projection as these areas are sufficiently away from the object that there is minimal risk of it intercepting the selected areas. The mean of four areas were measured in the transmitted and diffracted images in order to calculate the ratio as observed in Figure 5.36.
These differing trends throughout the image will cause unwanted artefacts in the following $\Delta\theta$, phase and δ maps. They are most noticeable in the $\Delta\theta$ and phase maps as vertical gradients going across the image. This could also contribute to the underestimation of the phase gradient. These differing trends could be due to noise in the images, which may explain why the transmitted is most affected as it typically possesses greater noise than the diffracted. This ratio drift will cause the $\Delta\theta$ maps to increase over the projection acquisition due to the phase retrieval process methodology as observed in Figure 5.37.
We assume that the ratio drift acts evenly across the entire image then we

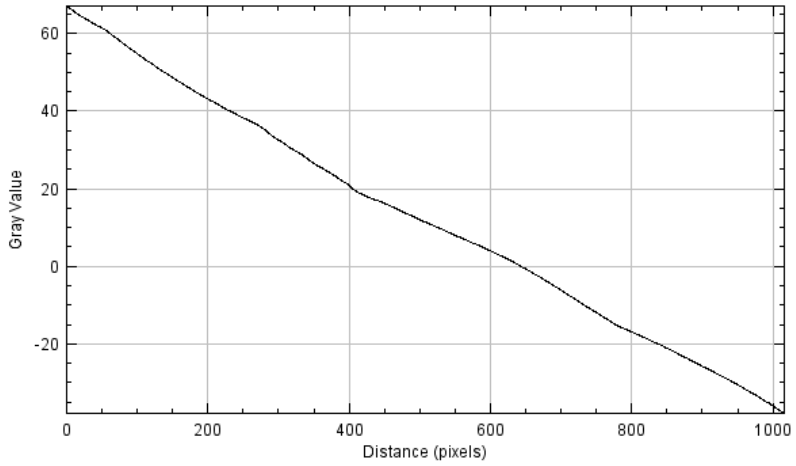

Figure 5.32: Plot of the horizontal yellow lines propagating through the calculated map of the difference between a phase map with and without the application of the ratio shift correction. We can see there is a steady linear trend of the grayscale value decreasing as the line propagates through the air above the phantom. This linear trend is due to the line being dominated by the bright spot on the left and the dark spot on the right.

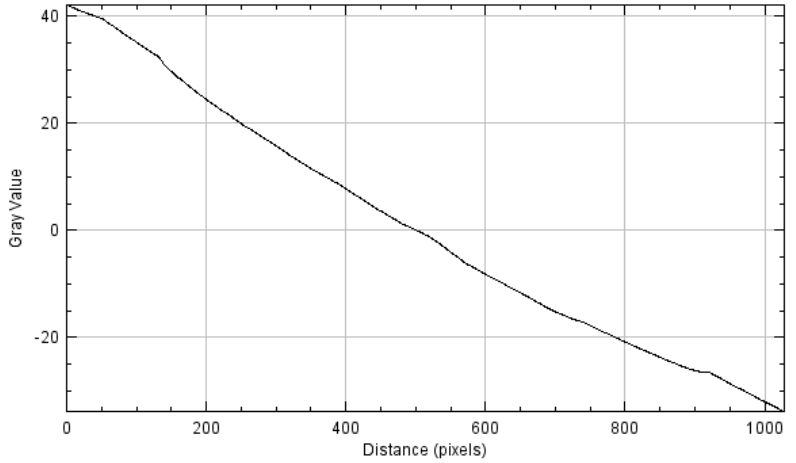

Figure 5.33: We see an near identical plot of the phase map change to Figure 5.32 from the ratio drift correction. It is crucial to note from comparing this plot with Figure 5.32 is that the magnitude of the gradient appears to decrease as the line moves down the phantom. We predict that this ratio drift correction will change once the two bottom corner gray spots begin to dominate then we will see an inverse parabolic trend.

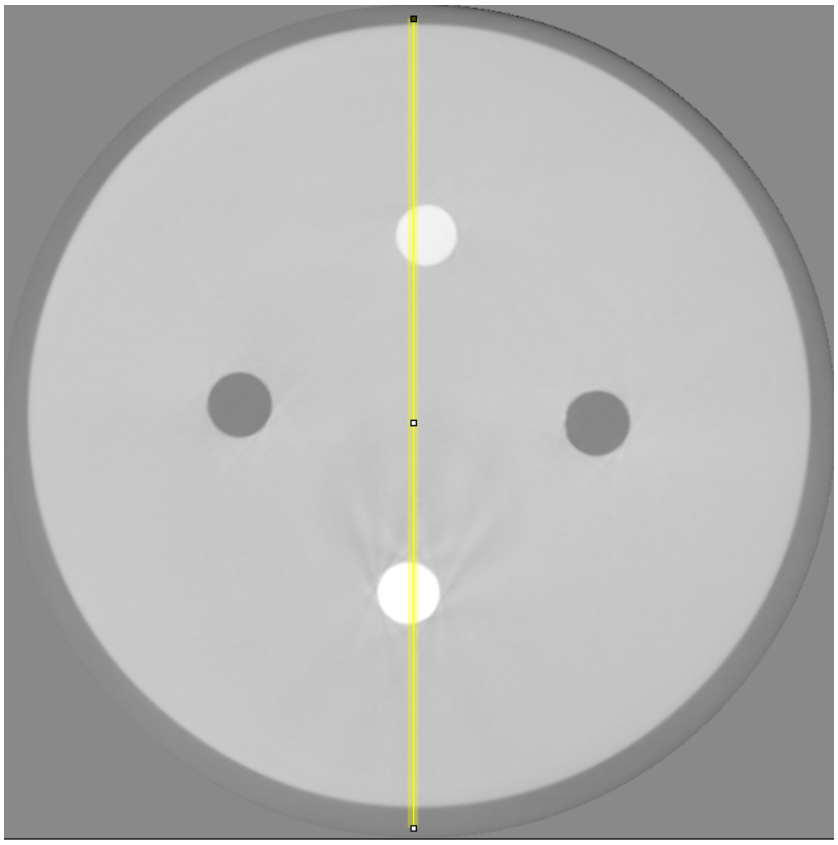

Figure 5.34: δ map with pixel dimension 840×840 and grayscale range $[-3.68 \cdot 10^{-7}, -4.35 \cdot 10^{-7}]$ that has had the ratio drift correction applied in the phase retrieval process. This δ map looks identical to the one shown in Figure 5.47

can simply correct for the ratio drift by background subtracting from air in the $\Delta\theta$ and $\Delta\theta_{180}$ maps.

5.4.3 Rocking Curve

Due to the nature of our phase retrieval method being based on the fitted rocking curve such as Figure 4.4, we can encounter a strong phase gradient in the correct direction, which can shift the working point over the top of the RC onto the opposite side of the rocking curve. When phase retrieval is performed, it is assumed that the resultant point (after the angular shift caused by refraction in the object) is on the same side of the rocking curve. Thus a wrong angular shift will be used to calculate $\Delta\theta$. This may cause a significant underestimation of the phase gradient for this point and cause

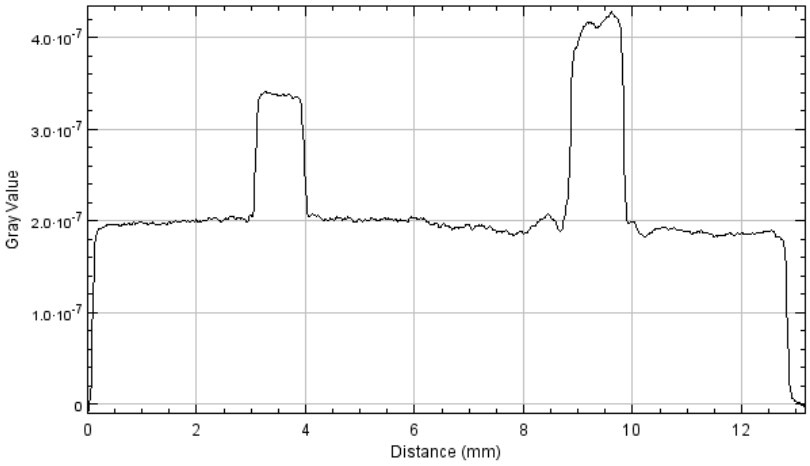

Figure 5.35: Plot of the yellow ROI going down through the perspex phantom with teflon and aluminium holes, respectively. When we compare the values of aluminium and teflon in this δ map to the values in Tables 5.1 and 5.2 we see they are slightly lower. There seems to be no other observable changes in this plot compared to Figure 5.48.

significant errors or artefacts in following images. This could be fixed by either reducing the magnitude of the phase gradient (discussed prior) or by using an initial point that is lower on the rocking curve. Having an initial point lower on the RC especially near the tails of the rocking curve gives low intensity of the diffracted image, which results in poor SNR. Points along the straight slope of the RC are ideal as both the positive and negative phase gradients will have similar magnitude of phase gradients The initial point used in this experiment was found to be Minus 25%, which is low enough to safely assume that there is no phase gradient strong enough to go over the peak of the RCs.

5.4.4 Linear Trend

There is a correction that was applied to all the phase maps in the Results Chapter (Chapter 5) to compensate for a linear trend caused by the under-estimation of the phase gradient on the left hand side of the phantoms edge compared to the right hand side and vice versa. This causes the phase at one of the sides of the phantom to be significantly lower than the other, as shown in Figures 5.39. This can be corrected by applying a linear gradient across the phantom to bring one side of the phantom to be approximately equal to the other. This linear correction can be calculated for each horizontal line

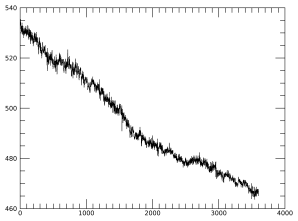

(a) Top left diffracted projection.

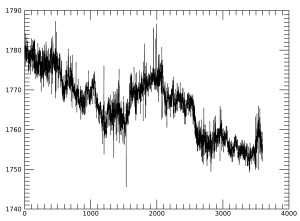

(b) Top left transmitted projection.

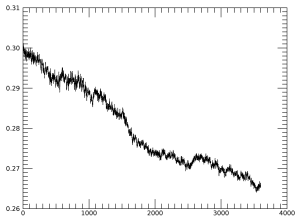

(c) Top left ratio projection.

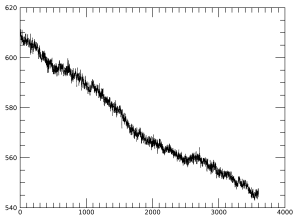

(d) Top right diffracted projection.

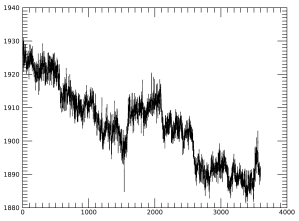

(e) Top right transmitted projection.

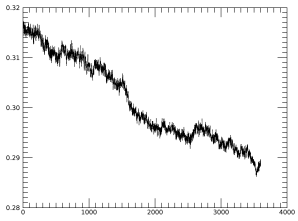

(f) Top right ratio projection.

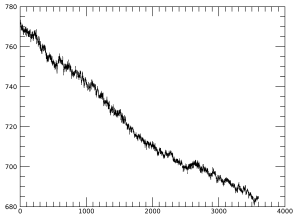

(g) Bottom left diffracted projection.

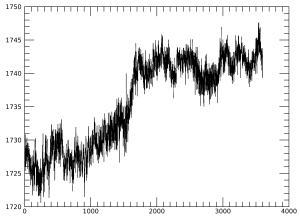

(h) Bottom left transmitted projection.

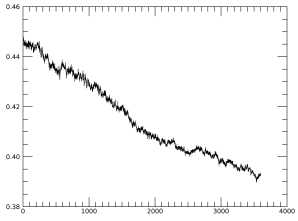

(i) Bottom left ratio projection.

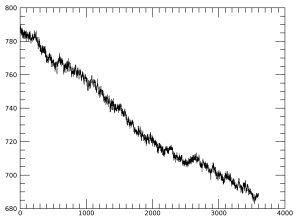

(j) Bottom right diffracted projection.

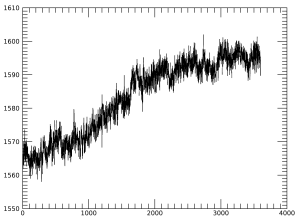

(k) Bottom right transmitted projection.

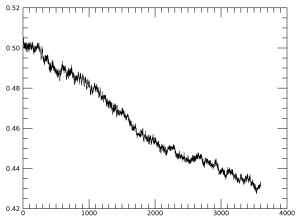

(l) Bottom right ratio projection.

Figure 5.36: Caption on next page.

Figure 5.36: Analysis of the drifting present in the diffracted (1st column), transmitted (2nd column) and ratio (3rd column) images by taking the mean of four small ROI in air for the top left (1st row), top right (2nd row), bottom left (3rd row) and bottom right corners (4th row) in the images. We can observe that the trend of the diffracted drift is similar for all the points with only the vertical intercept and gradient differing. In this case the top corners of the diffracted images have lower intercepts than the bottom this makes the ratio curve more noisy as the transmitted data has more impact. The transmitted trend is similar for the top corners and similar for the bottom corners but completely different to each other. The top corners have the opposite gradient than the bottom corners and all corners but the bottom right have some square shaped bump in the centre. The ratio curves are all dominated by the drift in the diffracted as this is much larger than the drift in the transmitted, thus they all follow a downwards linear trend.

going across the phantom resulting in lines appearing in the phase image. This does not cause artefacts in the individual tomographic slices of the δ map but these lines going across the phase images will appear evident in the fully reconstructed 3-D volume. It can also be calculated for one chosen horizontal line and applied to the entire phase map with the air-phantom interface coordinates found manually or by code if they are distinct. We analysed additional projections with similar angular orientation displayed in Figures 5.38 with their respective plots shown in Figure 5.39.
We know the phase shift should be zero in air, which is not the case in the phase maps. Therefore, we can justify correcting the phase maps accordingly so that the phase shift in air is set to zero. Previously this has been corrected through background subtraction in the two $\Delta\theta$ maps but this might cause the phase gradients to be underestimated and does not correct for the linear trend. The linear trend and non-zero phase values in air might be due to the amplification of low frequency signals and noise during the integration process. Therefore, we can apply a high pass filter to the phase map in Fourier space to remove the lowest frequencies and then apply and offset or a mask so that the air phase values are set to zero in the phase maps. This should remove the linear trend in the phase maps and produce better results. Applying a high pass filter in fourier space to truncated phase maps resulted in phase maps similar to Figure 5.40. The four holes in the phantom are clearly distinguished in Figure 5.40 with the plot of the horizontal line through them shown in Figure 5.41 supporting this. We then perform 180° CT reconstruction using filtered phase maps similar to Figure 5.40 to

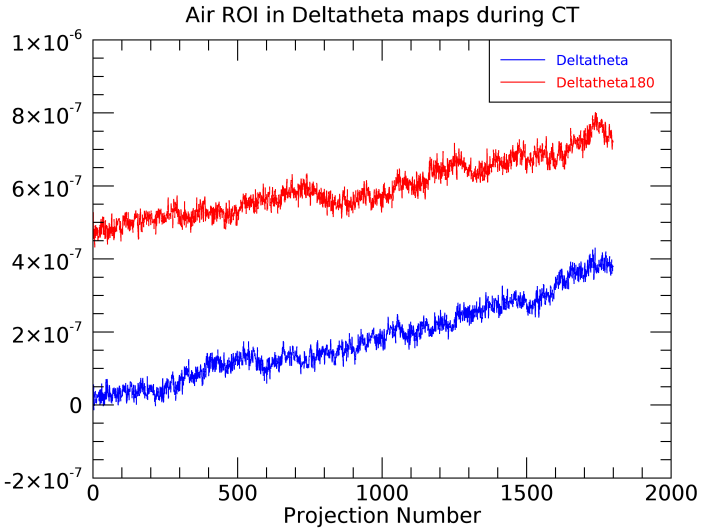

Figure 5.37: A steady increase in intensity of an air region in the $\Delta\theta$ and $\Delta\theta_{180}$ maps from the phase retrieval process due to the ratio drift. This has to be and is corrected by performing background subtraction from air in the entire $\Delta\theta$ and $\Delta\theta_{180}$ maps.

produce δ maps, where a slice is displayed in Figure 5.42. This shows that while filtering the phase maps does indeed remove the linear trend previously observed in the phase maps. It also causes shading in the δ maps and thus errors in the measured δ values of media present in the phantom. We will either need to use a new approach or change the specifications of the high pass filter to remove the linear trend without new errors and artefacts arising.
We can qualitatively check the edges of the $\Delta\theta$ map by focusing in on either side of the phantoms surface and enhancing the contrast as shown in Figures 5.44a and 5.44b. Figure 5.46 shows that the irregular behaviour of the left hand edge in the $\delta\theta$ map is still present even with the alignment of the diffracted and transmitted projections being improved. This irregular behaviour means that the simple stretch applied to the transmitted or diffracted projections will not result in a better alignment.
With these above mentioned considerations, changes and corrections applied to $\Delta\theta$ maps and the phase retrieval process we now produce the new phase and δ maps in Figures 5.49 and 5.47, respectively.

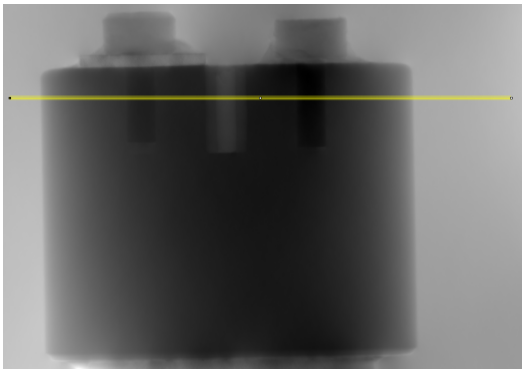

(a) Phase map of the 68th projection.

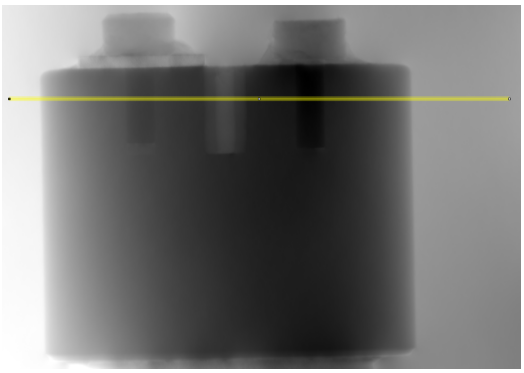

(b) Phase map of the 70th projection.

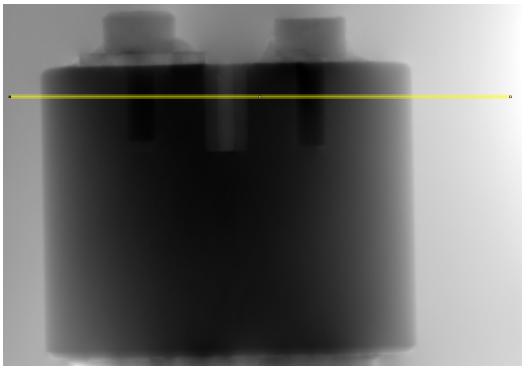

(c) Phase map of the 77th projection.

Figure 5.38: Phase maps of near angle projections with an identical horizontal yellow line through the phantom with their respective plots shown in Figure 5.39.

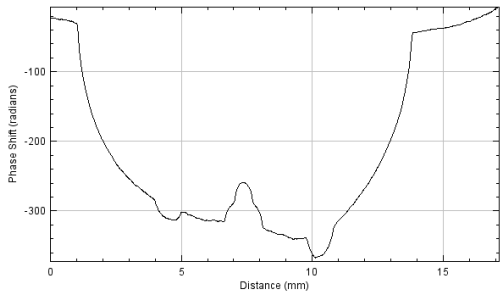

(a) Plot of yellow line ROI in the phase map of the 68th projection.

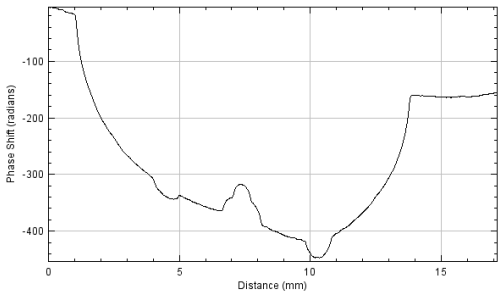

(b) Plot of yellow line ROI in the phase map of the 70th projection.

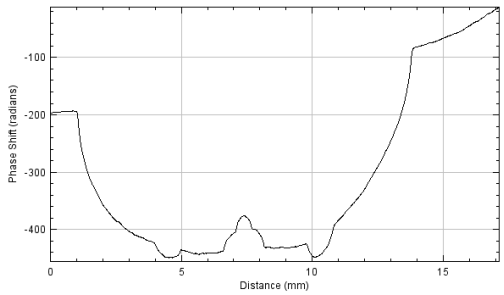

(c) Plot of yellow line ROI in the phase map of the 77th projection.

Figure 5.39: Plot of yellow line ROI in the respective phase maps emphasising the weird behaviour of the linear trend. We can observe the change in the magnitude of the gradient of the linear trend between the 68th and 70th projection where the object has only been rotated 0.2° between the two projections. Crucially we also observe the change in the direction of the linear trend gradient between the 70th and 77th projection. This suggests that the linear trend follows an irregular behaviour that would have to be modeled and corrected for each individual phase map. This also implies that the refraction angle is not always lower on one side. So perhaps it is a combination of the imperfect alignment, sampling of the object by the pixel and all other sources of error. The integration then amplifies the low frequency noise.

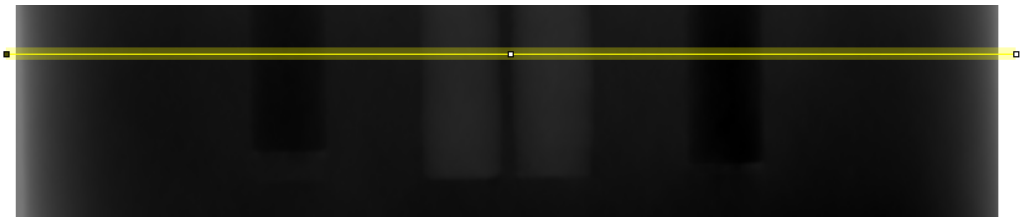

Figure 5.40: Phase map of the perspex phantom after a high pass filter has been applied in Fourier space.

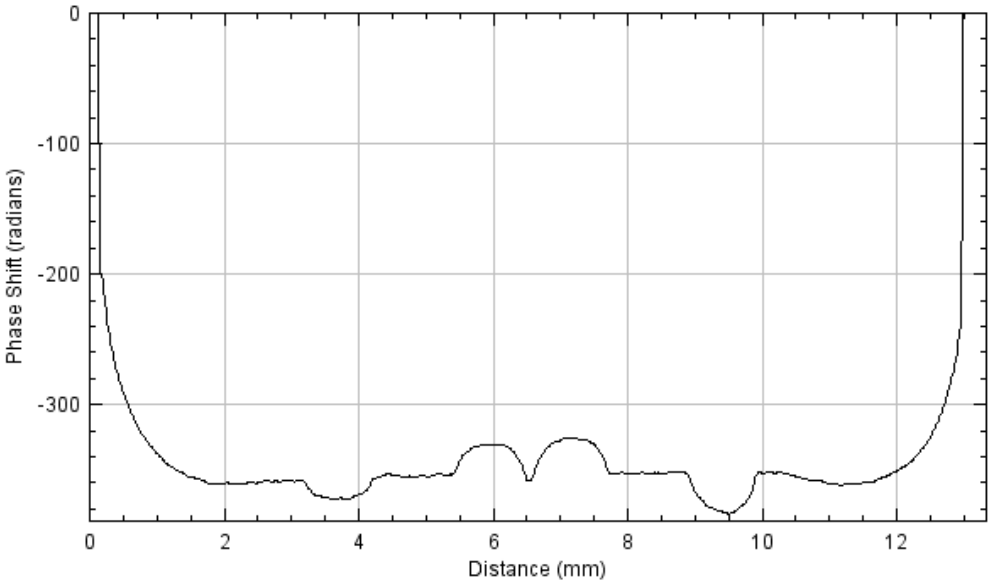

Figure 5.41: Plot of the filtered phase map, from which we can see the distinct four bumps corresponding to the four holes in the perspex phantom. One concerning thing is the upwards curve at the bottom of the profile as this should be flat or downwards. This suggests that the phase maps were over-filtered with key information being removed resulting in errors and artefacts in the phase maps and reconstructed slices.

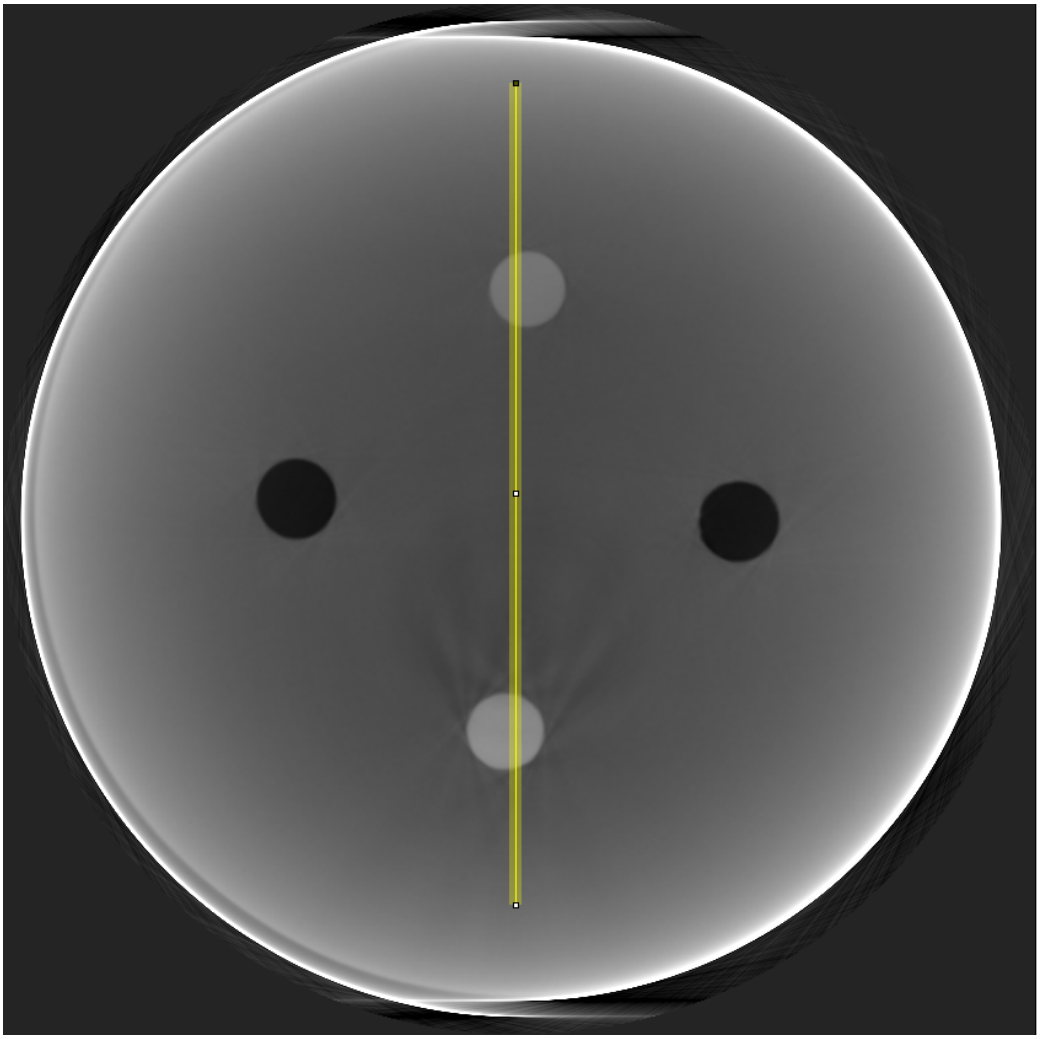

Figure 5.42: Slice of the δ map in of the perspex phantom with clear shading present throughout the perspex media. In theory this should be uniformly grayscale as it is comprised of a single uniform perspex media. This is cause for concern as this suggests a parabolic trend will be seen when a ROI such as the yellow line is plotted as in Figure 5.43 due to the shading likely caused by the filtration of the phase map.

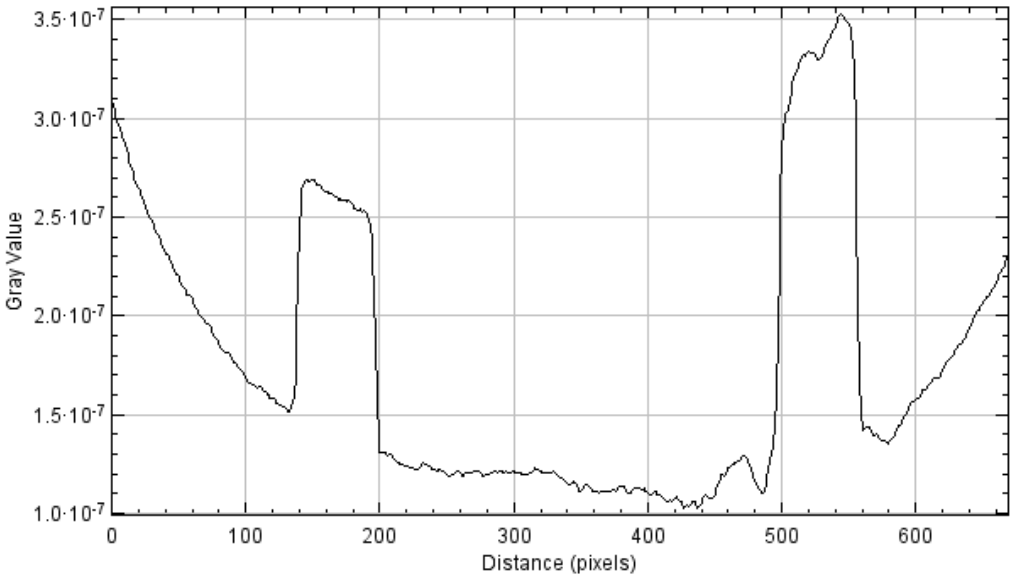

Figure 5.43: Plot of the yellow line ROI in the δ map shown in Figure 5.42. We can see the parabolic trend from the shading in the δ map, which results in errors in the measured δ values of media present in the phantom.

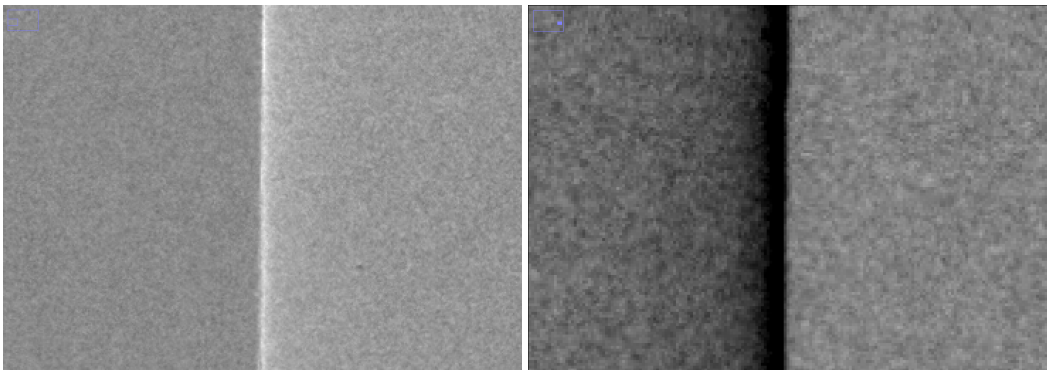

(a) $\Delta\theta$ map of the left edge of the perspex phantom.

(b) $\Delta\theta$ map of the right edge of the perspex phantom.

Figure 5.44: Contrast enhanced 640th projection $\Delta\theta$ map showing the left 5.44a and right 5.44b respective edges of the phantom. It can be seen the right edge (negative phase gradient) is clear and well defined with expected refraction profile over into the air and perspex. However, with the left edge (positive phase gradient) it appears to be ill defined with a peak refraction angle edge that seems to narrow, broaden and even split up into two along the edge of Figure 5.44a. This ill defined peak refraction angle for the positive phase gradient is what causes it to be underestimated and the two lines suggest that either the misalignment has occurred either between the two $\Delta\theta$ images or the diffracted and transmitted images.

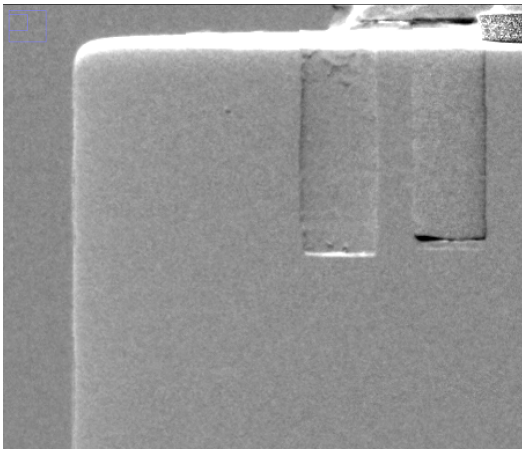

(a) Contrast enhanced $\Delta\theta$ map top left edge of the perspex phantom.

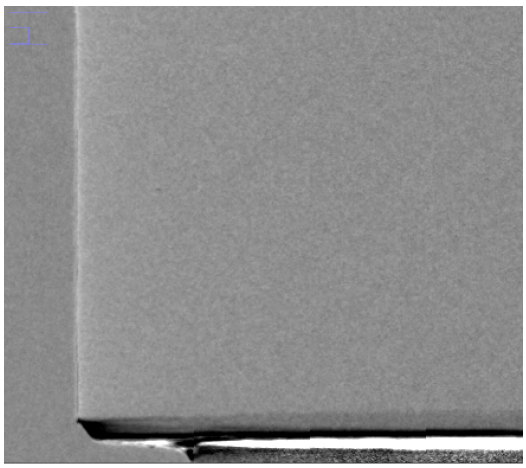

(b) Contrast enhanced $\Delta\theta$ map bottom left edge of the perspex phantom.

Figure 5.45: Contrast enhanced top and bottom left edge of the $\Delta\theta$ map highlighting the irregular behaviour of the left hand edge. We observe the irregular change in brightness and alignment of the vertical edge of the phantom, while noting that the alignment becomes significantly worse towards the bottom left edge of the perspex phantom.

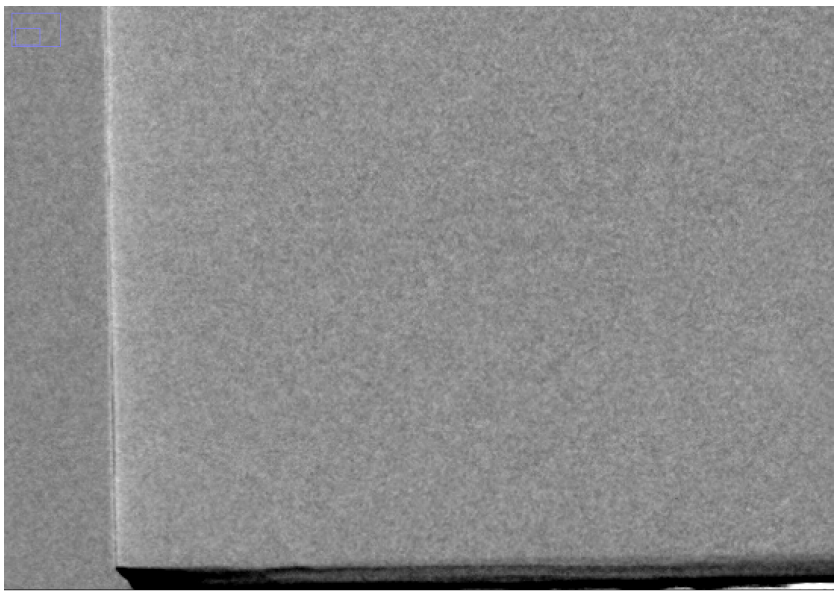

Figure 5.46: The irregular behaviour of the left hand edge in the $\Delta\theta$ map is still present even with the alignment of the diffracted and transmitted projections being improved.

5.5 New Results

We follow the same method corrections discussed in the analysis section (Section 5.4) relating to the phase information in the phase retrieval procedure and perform CT to obtain a δ map from this we measure the following results shown in Table 5.2. The measured values are confirmed by observing Figure

	β_{Theo}	β_{Mea}	δ_{Theo}	δ_{Mea}
AL	$1.7 \cdot 10^{-9}$	$1.6 \pm 0.1 \cdot 10^{-9}$	$8.0 \cdot 10^{-7}$	$4.3 \pm 0.1 \cdot 10^{-7}$
Perspex	$1.6 \cdot 10^{-10}$	$1.5 \pm 0.3 \cdot 10^{-10}$	$3.9 \cdot 10^{-7}$	$2.1 \pm 0.1 \cdot 10^{-7}$
PTFE	$2.5 \cdot 10^{-10}$	$4.0 \pm 0.3 \cdot 10^{-10}$	$6.5 \cdot 10^{-7}$	$3.6 \pm 0.1 \cdot 10^{-7}$

Table 5.2: Comparison between theoretical δ values and measured δ values for media in the phantom once the misalignment corrections (discussed in the Section 5.4.3) were applied to the phase retrieval process. The δ_{Mea} values for aluminium and perspex are closer to δ_{Theo}, while teflon is further away when compared to the results obtained in Table 5.1.

5.47 of the δ map with a ROI selected, which is plotted in Figure 5.48. For comparison purposes there is the phase map seen in Figure 5.49 with two ROIs, going through the materials in the phantom and one going through just the phantom, which are plotted in Figures 5.50 and 5.51, respectively.

For comparison purposes, let us take similar ROIs for the old δ and phase maps in Figures 5.52 and 5.54 with plots of these ROI in Figures 5.53 and 5.55, 5.56 for the two ROIs in the phase map (Figure 5.49), respectively.

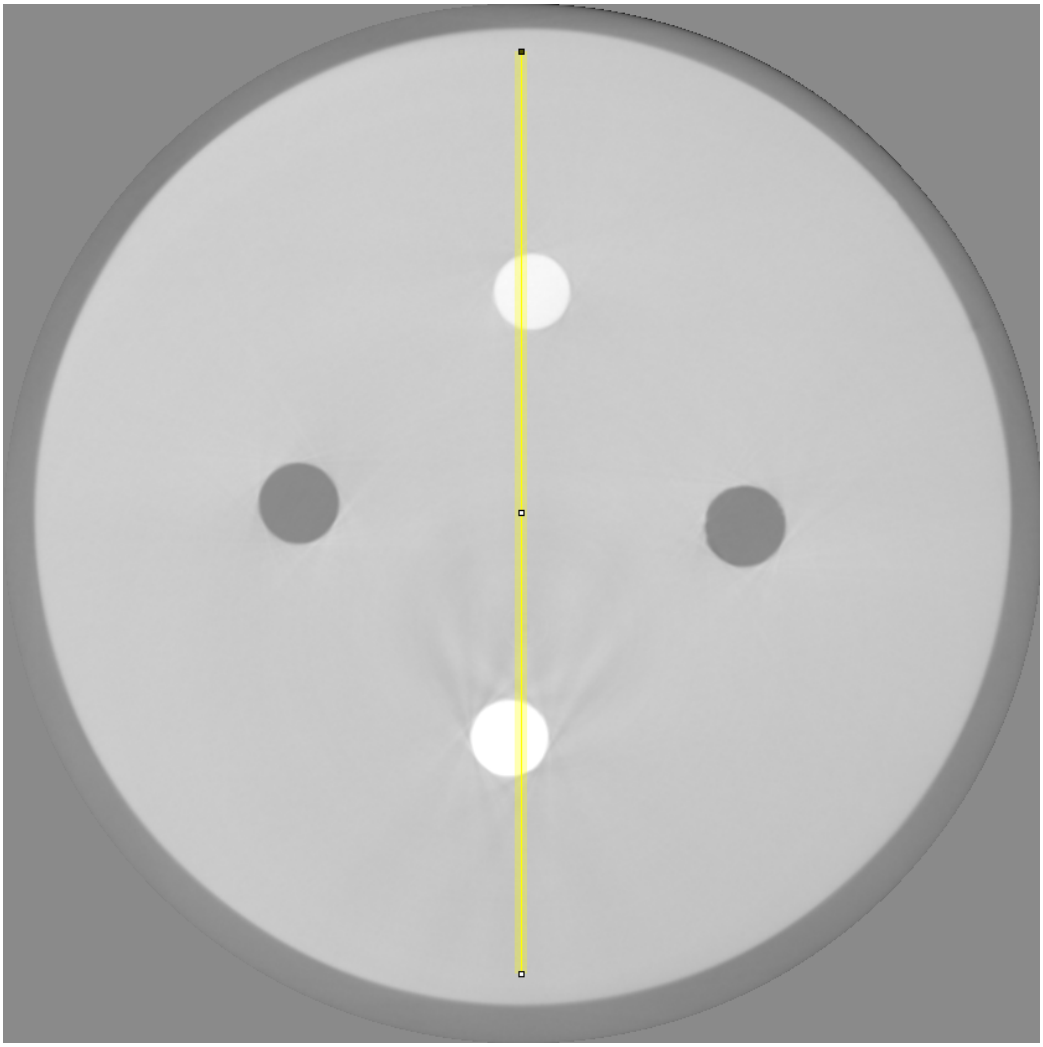

Figure 5.47: Slice of the new δ map with pixel dimension 840×840 and grayscale range $[-7.45 \cdot 10^{-8}, 4.50 \cdot 10^{-7}]$, with vertical line ROI going through centre calculated from 180° tomographic reconstruction of the phase maps with the misalignment corrections applied discussed in detail in the Analysis section. Comparing this map to the previous δ map in Figure 5.22 we see there is a lot less observable smearing in the form of random bright and dark regions in the perspex phantom. This helps confirm that the applied corrections have made a difference and this is further emphasised by looking at the greater contrast between the aluminium and teflon holes in this image compared to the later.

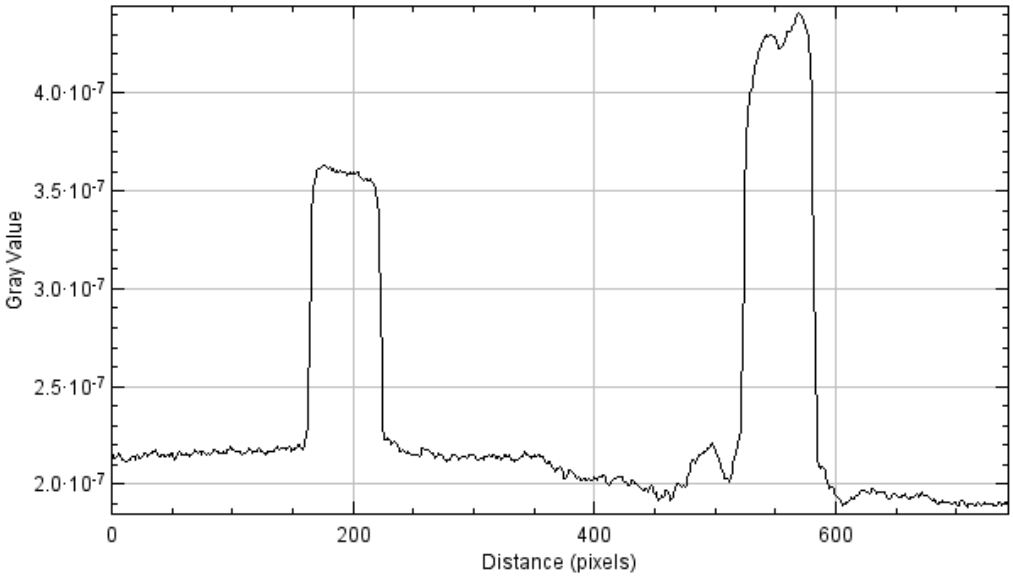

Figure 5.48: Plot of the vertical line going through the centre of the new δ map Figure 5.47. We can see the large jump in the measured refractive index from approximately $2.1 \cdot 10^{-7}$ to $4.3 \cdot 10^{-7}$ and $3.6 \cdot 10^{-7}$ as the ROI passes through the aluminium and teflon holes, respectively. This supports our results displayed in Table 5.2.

Figure 5.49: Heavily truncated image with pixel dimension 840×176 and grayscale range $[-430.60,1.13]$ radians, of the corrected new phase map to speed up the phase retrieval process. The two yellow lines pass horizontally through the phantom with the top passing through the four holes in the phantom, while the bottom does not. Plots of these yellow lines are shown in Figures 5.50 and 5.51, respectively. Note the darkness of the phase map compared to Figure 5.21 of the previous phase map. This is because of the lower positive and negative values present in this image increasing the relevant contrast.

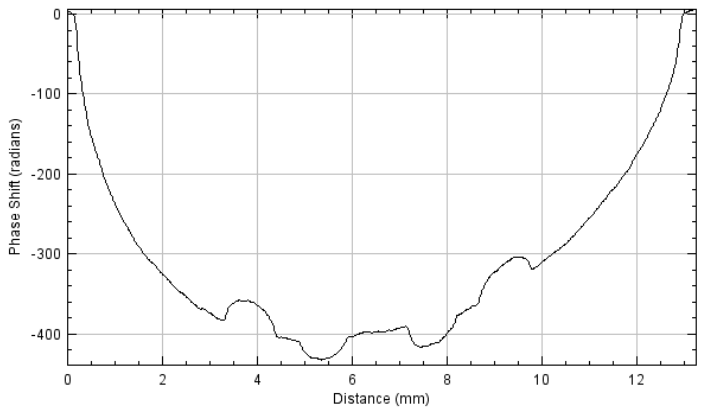

Figure 5.50: Plot of the upper horizontal line in Figure 5.49 going through all of the holes in the phantom as seen by the four small bumps corresponding to the aluminium, air and teflon. The evenness of the parabola suggests that the phase map is accurate and the linear trend was corrected for precisely.

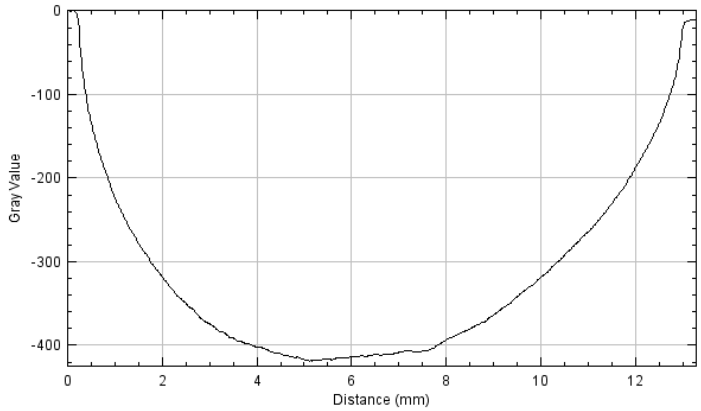

Figure 5.51: Plot of the lower horizontal line in Figure 5.49 missing all of the holes the phantom. It should be noted that the values in the air on either side of the phantom are not equivalent like in Figure 5.50. This means that the process to correct for this did not completely fix this behaviour along that line or it could be because the yellow lines are 10 pixels wide and take an average of the values. However, this difference is negligible and we do not take any measurements from that slice.

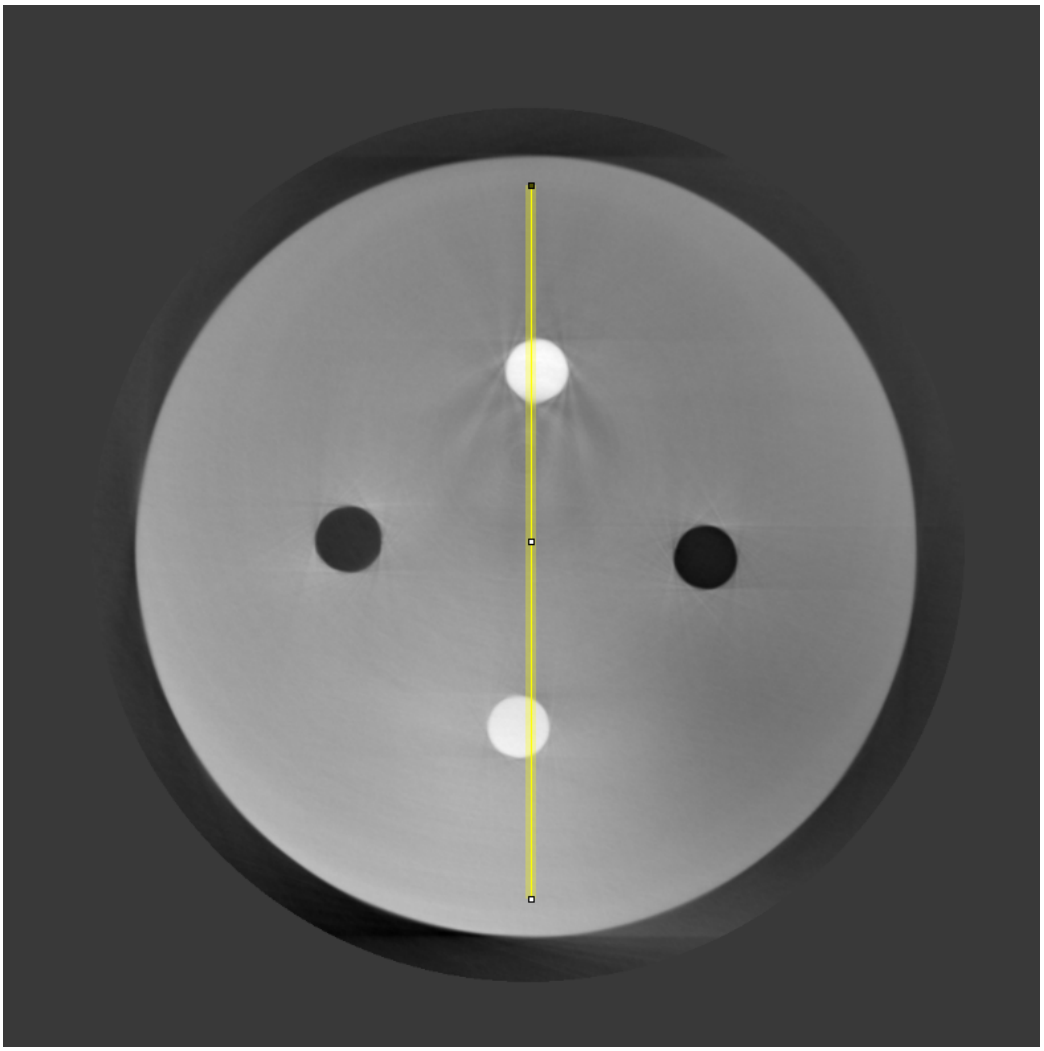

Figure 5.52: δ map with pixel dimension 840×840 and grayscale range $[-3.84 \cdot 10^{-7}, 4.50 \cdot 10^{-7}]$ identical to Figure 5.22 with vertical line ROI down the centre through the aluminium and teflon holes to compare values/trends with the corrected δ map in Figure 5.47. The plot of this line is displayed in Figure 5.53.

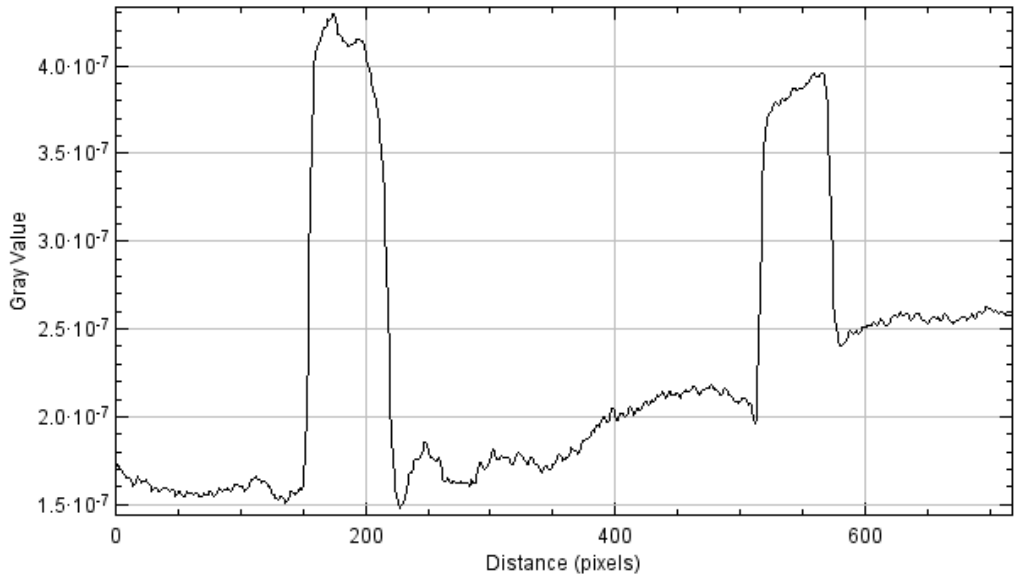

Figure 5.53: Plot of the vertical line going through the centre of the δ map Figure 5.52. We can see the large spikes in the measured refractive index as it passes through the aluminium and teflon holes approximately equal to their values in Table 5.1. The key difference to highlight between this plot and the plot of the corrected δ map (Figure 5.48) is the significant upward trend and overall instability that is present in this uncorrected δ map. This is from the bright and dark spot around the δ map in Figure 5.52 caused by bleeding or other uncertainties discussed in the Analysis section, Section 5.4.

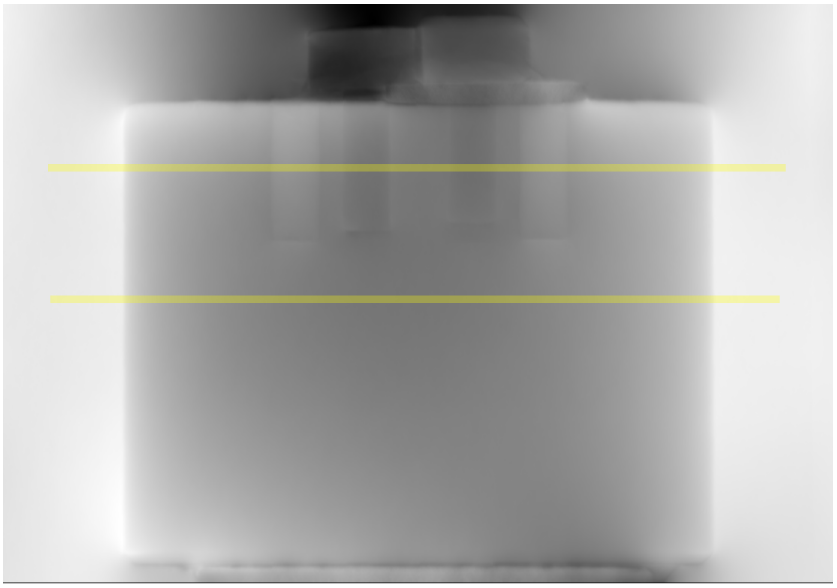

Figure 5.54: Phase map with pixel dimension 1108×771 and grayscale range $[-314.78,31.80]$ radians, which is identical to Figure 5.21 with ROI similar to Figure 5.49 for adequate comparison. Plots for the upper and lower lines are found in Figure 5.55 and 5.56, respectively.

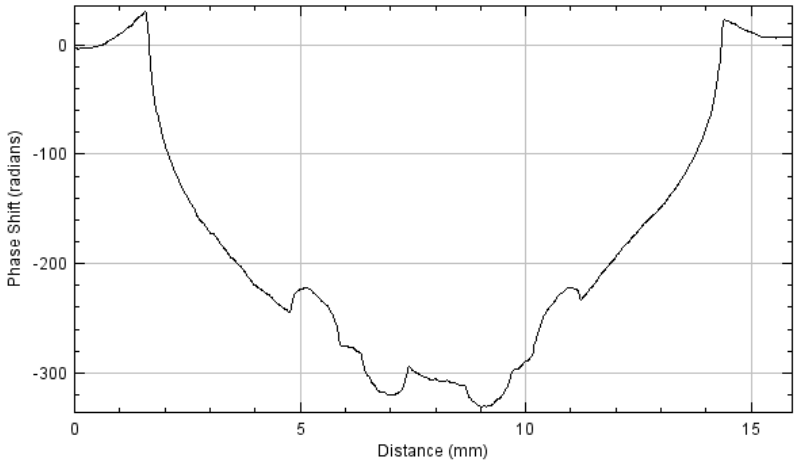

Figure 5.55: Plot of the upper horizontal line going through all of the holes in the phantom as seen by the four small bumps corresponding to the aluminium, air and teflon. The key difference to note is that the magnitude of the phase values is a lot lower in the uncorrected phase map than in the corrected phase map. Another concerning thing is that both the edges of the phantom are not equal to 0, which could cause errors in the δ map e.g. underestimation of the measured δ values in the phantom.

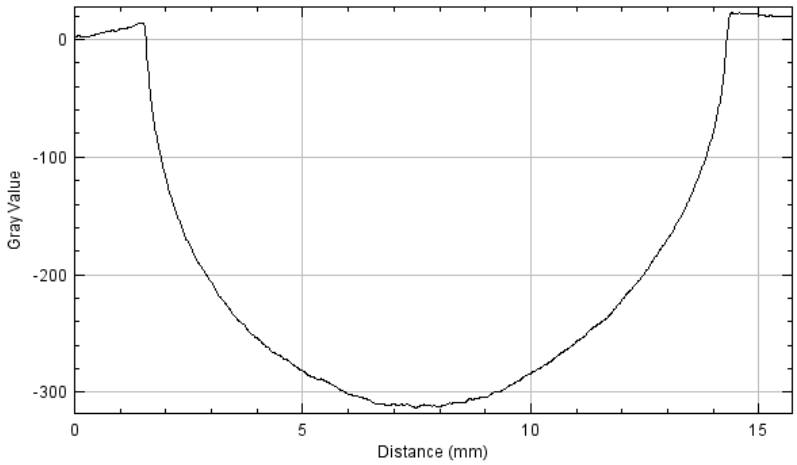

Figure 5.56: Plot of the lower horizontal line missing all of the holes the phantom. No smearing is observed as it is taken further away from the four holes and we still have the same problem as in Figure 5.51 of the two side of the phantom not being equal.

5.6 Theoretical values

We know that the theoretical values obtained for media can vary between databases. This variation is due to the differing experimental setup and methodology to calculate theoretical values of media as well as differences in the media. For media such as aluminium impurities in the form of alloys such as iron or copper can be found, which will alter the density and composition. Plastics and other composite media such as perspex and teflon consist of multiple elements causing their composition and density to vary more than metals like aluminium. It is therefore desirable to compare our results with multiple theoretical values from different sources, which is done in Tables 5.3 and 5.4. We see from comparing the theoretical δ and β values in Tables

	β_{Theo}	β_{Mea}	δ_{Theo}	δ_{Mea}
AL	$1.5 \cdot 10^{-9}$	$1.6 \pm 0.1 \cdot 10^{-9}$	$8.0 \cdot 10^{-7}$	$4.3 \pm 0.1 \cdot 10^{-7}$
Perspex	$1.4 \cdot 10^{-10}$	$1.5 \pm 0.3 \cdot 10^{-10}$	$3.9 \cdot 10^{-7}$	$2.1 \pm 0.1 \cdot 10^{-7}$
PTFE	$3.7 \cdot 10^{-10}$	$4.0 \pm 0.3 \cdot 10^{-10}$	$6.5 \cdot 10^{-7}$	$3.6 \pm 0.1 \cdot 10^{-7}$

Table 5.3: Table of theoretical δ and β values of media in the phantom obtained from `http://henke.lbl.gov/optical_constants/getdb2.html` (accessed 15 Feb 2020).

	β_{Theo}	β_{Mea}	δ_{Theo}	δ_{Mea}
AL	$1.7 \cdot 10^{-9}$	$1.6 \pm 0.1 \cdot 10^{-9}$	$8.0 \cdot 10^{-7}$	$4.3 \pm 0.1 \cdot 10^{-7}$
Perspex	$1.6 \cdot 10^{-10}$	$1.5 \pm 0.3 \cdot 10^{-10}$	$3.9 \cdot 10^{-7}$	$2.1 \pm 0.1 \cdot 10^{-7}$
PTFE	$5.0 \cdot 10^{-10}$	$4.0 \pm 0.3 \cdot 10^{-10}$	$6.6 \cdot 10^{-7}$	$3.6 \pm 0.1 \cdot 10^{-7}$

Table 5.4: Table of theoretical δ and β values of media in the phantom obtained from X-ray lib (accessed 17 Feb 2020).

5.2, 5.3 and 5.4, that there is slight variation. However, this variation is not large enough to justify differences in the measured and theoretical δ values. We do have a better match for the measured and theoretical β values for

Teflon in Table 5.3, while maintaining good agreement with the measured and theoretical β values for aluminium and perspex.

Chapter 6

Discussion

In this chapter we will give an overview on why our results for the function δ were off by approximately a factor of two, including suggestions for future experiments to test our speculations and obtain better results.

6.1 Errors

The Laue geometry method used in our phase retrieval process applies the GOA, which only holds for small deviations in the x-ray wavefield as it propagates through the phantom. There is a large discrepancy between the refractive properties of air and perspex applied in our images, which could break the GOA. This would result in the magnitude of the phase gradients being underestimated. We can compare our results to those obtained by Rutishauser et al [2] to see if there are similar discrepancies between the theoretical and measured refractive properties of perspex. From applying an inclined geometry GI method Rutishauser to a cylindrical perspex phantom in [2] [101] obtained δ for perspex to be around $0.4 \cdot 10^{-7}$, which is $10\times$ lower than the theoretical value of $3.9 \cdot 10^{-7}$. One interesting thing is that in the same papers a rat cerebellum was also imaged, but this was submerged in paraffin in order to hold the sample in place. The paraffin also meant that there was no strong change in refractive index between materials. The δ for rat cerebellum in these papers was measured to be $[3, 4]\cdot 10^{-7}$, which is in good agreement with the theoretical value of $3.53 \cdot 10^{-7}$. This supports the case of the GOA condition breaking in this experiment due to the high magnitude of the phase gradients in our sample as mentioned previously. We could check this by submerging the phantom in a media with similar refractive properties as perspex, such as parafin and repeating the experiment. In this case the GOA should hold better therefore enabling results that are closer to the

theoretical values. The application of the inclined geometry makes precisely aligning the transmitted and diffracted projections more challenging as they have to be precisely aligned in both the vertical and horizontal directions. Previous work by Kitchen et al [79] using a similar Laue geometry setup with the GOA without applying inclination achieved good results for the projected thickness of two cavities in an unsubmerged perspex phantom one was empty and the other contained glass microspheres in an unsubmerged perspex phantom. This contradicts GOA breaking and emphasises that the source of error is from imperfect alignment of the transmitted and diffracted projections. It may be a combination of these sources of errors that are added together and are then integrated, which amplifies low frequency noise that results in the phase gradients being underestimated.

6.2 Speculations

One thing to consider is to not use both the transmitted and diffracted images and instead to use only the the diffracted images at two angular positions. This could be implemented with a Bragg crystal and looking at only the diffracted wavefield following a method such as Menk et al [102] with much simpler image and phase retrieval processes. Importantly it does not require the two images to be aligned, where our underestimation of the phase gradient and other issues seem to arise. From this logic, it would be quite interesting to apply an inclined geometry to a Bragg geometry method such as Menk et al [102] to compare results. If there is major underestimation of the phase gradient then it could be the GOA is applied in the phase retrieval process for this method and its condition is not holding.

In our application of inclined geometry to ABPCI the detector and sample is only rotated 8° following the x-ray wavefield propagation direction. This means that approximately 90% of our phase information comes from the vertical direction rather than an ideal 50/50 split using a 45° inclined geometry applied by Rutishauser [2]. It is possible that missing phase information from the horizontal direction contributed or caused the phase gradients to be underestimated. Moreover if we observe Eqns (2.66) and (2.67) we note that g_x, our primary source of information, is divided by $2\cos(8) = 1.98$. This could explain why our results are approximately off by a factor of two. This might not be compensated by g_y as it is divided by $2\sin(8) = 0.278$, which amplifies the noise and could cause the image to be ill defined due to blurring. However, as discussed earlier the poor results of the perspex phantom obtained by Rutishauser contradicts this argument but it is worthwhile confirming.

It is important to note that we are using a phantom, which can be assumed to be a quasihomogeneous medium, meaning USAXS should be negligible. This is crucial as our method using two simultaneous images to calculate the phase gradient does not take USAXS into account. Another ABI technique, MIR (discussed in Section 2.9.9), uses data sets from multiple points on the rocking curve to reconstruct the δ maps and takes the USAXS into consideration. However, MIR needs to use at least three, and ideally around 11 data sets [103], which is more time consuming than reconstructing the phase using two simultaneous images. It would be interesting once work has been done to ensure errors are removed to try reconstructing the phase maps of an inhomogeneous medium using two simultaneous projections as this is where the method traditionally falls short. It would be good to do the experiments with MIR using only the diffracted beam to hopefully get a highly quantitative measure of δ for direct comparison with the results obtained here.

ABPCI still has lots of hurdles before clinical implementation such as generating phase contrast images using a conventional x-ray source, which has been done by [104] [105] [106] and with all components spaced much closer together. This would make it possible to see ABPCI applied to conventional CT scanners such as traditional radiography. However, more issues would arise with stability of the analyser crystal as it rotates around in the CT scanner at high velocity due to the microradian Bragg window. Hence, the sample is usually rotated during CT. Even in our experiment the stability of the analyser crystal was brought into question when it was stationary and fixed on a high precision stage. Furthermore, the progression of ABPCI seems to be a lot slower than other phase contrast methods as ABI is highly sensitive to energy bandwidth, so you have to monochromate the source for it to work well. This requiremnt makes clinical applications of ABPCI challenging. There is no such restriction for grating interferometry, hence it can be applied with a conventional polychromatic x-ray source [107] [108] [109] [110].

Chapter 7

Future work

Compared to the previous work undertaken by Kitchen et al [77], we had the additional complexity of having to align the 0° and 180° data to sub pixel accuracy across millions of pixels. With the addition of detector distortion, crystal distortion and alignment of opposing views this was a lot to align to subpixel accuracy. We should try repeating the experiment with the perspex phantom submerged in parafin as this should allow the GOA to hold throughout the experiment. If the GOA holds we should obtain measured values of δ that are much closer to the theoretical. If this does not give better results then we may need to develop more precise ways of measuring the distortions and better software in order to correct the problems and better achieve the required subpixel alignment. It would also be interesting to repeat the experiment with a larger angulation (30° or 40°) applied to the detector and phantom to test if this is a source of the underestimation of the phase gradients.

Chapter 8

Conclusion

In conclusion, we applied the inclined geometry method proposed by Rutishauer et al [2] through rotation of the detector and sample by 8° clockwise following the x-ray wavefield. This allows us to achieve 2-D phase sensitivity in a Laue geometry ABPCI setup. This calculated the phase contrast using two simultaneous (θ, $\theta + 180$) projections of the object through flipping and alignment of the $\theta + 180$ projection, so it overlaped the θ projection. We then splitted the phase gradient into its horizontal and vertical components. From here we performed 2-D Fourier integration of the phase gradients to calculate the phase map. Finally, we performed tomographic reconstruction to produce the δ and β maps, which provided the refraction and absorption properties of each material in the imaged phantom.

Measurements were taken the of the perspex, aluminium and teflon media in the phantom shown in Table 5.1. Their δ values were found to be $1.9 \pm 0.1 \cdot 10^{-7}$, $4.2 \pm 0.1 \cdot 10^{-7}$ and $4.0 \pm 0.1 \cdot 10^{-7}$, respectively, while the theoretical values were $3.9 \cdot 10^{-7}$, $8.0 \cdot 10^{-7}$ and $6.5 \cdot 10^{-7}$, respectively. The acquired β values were $1.6 \pm 0.1 \cdot 10^{-9}$, $1.5 \pm 0.3 \cdot 10^{-10}$ and $4.0 \pm 0.3 \cdot 10^{-10}$ while the theoretical were $1.5 \cdot 10^{-9}$, $1.4 \cdot 10^{-10}$ and $3.7 \cdot 10^{-10}$ for aluminium, perspex and teflon, respectively.

Analysis of the raw and processed data resulted in effects that were corrected for such as the ratio drift and linear trend, which result in an underestimation of the phase gradient, to give new results shown in Table 5.2 for δ of $2.1 \pm 0.1 \cdot 10^{-7}$, $4.3 \pm 0.1 \cdot 10^{-7}$ and $3.6 \pm 0.1 \cdot 10^{-7}$ for perspex, aluminium and teflon, respectively. These results are still off by approximately a factor of 2 as a result of the underestimation of the phase gradients. This underestimation of the phase gradients is likely due to the combination of errors from the applied GOA breaking from the large magnitude phase gradients as

well as misalignment of the transmitted and diffracted projections and the $\Delta\theta$ and $\Delta\theta_{180}$ maps being integrated, which amplifies low frequency noise. Furthermore, results from Rutishauser for perspex in air were also off by a large factor, with good results for submerged samples [2] [101]. MIR also applies the GOA but there are less alignment problems as only the diffracted data is used. The breaking of the GOA could be rectified by submerging the sample in a media with similar refractive properties to the perspex phantom such as parafin and repeating the experimental procedure. This should obtain results for the refractive properties of media in the phantom, which are closer to the reference values stated in Table 5.1.

Overall ABPCI is a promising imaging modality that is highly sensitive to small changes phase but requires a complex experimental setup and monochromatic x-ray wavefield. The complex experimental setup and monochromatic x-ray wavefield limits its current and future applications in to biomedical research and the clinical field.

Bibliography

[1] S. W. Wilkins, Ya I. Nesterets, T. E. Gureyev, S. C. Mayo, A. Pogany, and A. W. Stevenson. On the evolution and relative merits of hard x-ray phase-contrast imaging methods. *Philosophical transactions. Series A, Mathematical, physical, and engineering sciences*, 372(2010):20130021–20130021, 2014.

[2] Simon Rutishauser, Tilman Donath, Christian David, Franz Pfeiffer, Federica Marone, Peter Modregger, and Marco Stampanoni. A tilted grating interferometer for full vector field differential x-ray phase contrast tomography. *Optics express*, 19(25):24890, 2011.

[3] Marcus J. Kitchen, Konstantin M. Pavlov, Stuart B. Hooper, David J. Vine, Karen K. W. Siu, Megan J. Wallace, Melissa L. L. Siew, Naoto Yagi, Kentaro Uesugi, and Rob A. Lewis. Simultaneous acquisition of dual analyser-based phase contrast x-ray images for small animal imaging. *European Journal of Radiology*, 68(3):S49–S53, 2008.

[4] Jerrold T. Bushberg. *The essential physics of medical imaging*. Wolters Kluwer Health/Lippincott Williams Wilkins, Philadelphia, 3rd edition, 2012;2011;.

[5] R. Caciuffo, S. Melone, F. Rustichelli, and A. Boeuf. Monochromators for x-ray synchrotron radiation. *Physics Reports*, 152(1):1–71, 1987.

[6] Paolo Russo. *Handbook of X-ray Imaging: Physics and Technology*. CRC Press, 2017.

[7] Robert A Lewis, Keith D Rogers, Christopher J Hall, Alan P Hufton, S Evans, Ralf-Hendrik Menk, Giuliana Tromba, Fulvia Arfelli, Luigi Rigon, Alessandro Olivo, et al. Diffraction-enhanced imaging: improved contrast and lower dose x-ray imaging. In *Medical Imaging 2002: Physics of Medical Imaging*, volume 4682, pages 286–298. International Society for Optics and Photonics, 2002.

[8] Roger D Blandford and Kip S Thorne. Applications of classical physics. *lecture notes, California Institute of Technology*, page 12, 2008.

[9] Jani Keyriläinen, Alberto Bravin, Manuel Fernández, Mikko Tenhunen, Pekka Virkkunen, and Pekka Suortti. Phase-contrast x-ray imaging of breast. *Acta Radiologica*, 51(8):866–884, 2010.

[10] Alberto Bravin, Paola Coan, and Pekka Suortti. X-ray phase-contrast imaging: from pre-clinical applications towards clinics. *Physics in medicine and biology*, 58(1):R1–R35, 2013.

[11] Atsushi Momose and Jun Fukuda. Phase-contrast radiographs of non-stained rat cerebellar specimen. *Medical physics*, 22(4):375–379, 1995.

[12] P. C. Diemoz, M. Endrizzi, C. K. Hagen, C. Rau, A. Bravin, R. D. Speller, I. K. Robinson, and A. Olivo. Edge illumination x-ray phase-contrast imaging: nanoradian sensitivity at synchrotrons and translation to conventional sources. *Journal of Physics: Conference Series*, 499:12006, 2014.

[13] M. J. Kitchen, D. Paganin, R. A. Lewis, N. Yagi, K. Uesugi, and S. T. Mudie. On the origin of speckle in x-ray phase contrast images of lung tissue. *Physics in Medicine and Biology*, 49(18):4335–4348, 2004.

[14] Kaye S. Morgan, David M. Paganin, and Karen K. W. Siu. X-ray phase imaging with a paper analyzer. *Applied Physics Letters*, 100(12):124102–124102–4, 2012.

[15] David M. Paganin, Hélène Labriet, Emmanuel Brun, and Sebastien Berujon. Single-image geometric-flow x-ray speckle tracking. *Physical Review A*, 98(5), 2018.

[16] André Authier. Dynamical theory of x-ray diffraction. *International Tables for Crystallography*, pages 626–646, 2006.

[17] J. Als-Nielsen and Des McMorrow. *Elements of modern X-ray physics*. Wiley, Hoboken, 2nd;2. aufl.; edition, 2011.

[18] Kavitha Srinivasan, Mohammad Mohammadi, and Justin C. Shepherd. Investigation of effect of reconstruction filters on cone-beam computed tomography image quality. *Australasian Physical Engineering Sciences in Medicine*, 37:607–614, 2014.

[19] P. C. Diemoz, A. Bravin, and P. Coan. Theoretical comparison of three x-ray phase-contrast imaging techniques: propagation-based imaging, analyzer-based imaging and grating interferometry. *Optics express*, 20(3):2789, 2012.

[20] Christian David, B Nöhammer, H_H Solak, and E Ziegler. Differential x-ray phase contrast imaging using a shearing interferometer. *Applied physics letters*, 81(17):3287–3289, 2002.

[21] Rolf Behling. *Modern diagnostic X-ray sources: technology, manufacturing, reliability*. CRC Press/Taylor Francis, Boca Raton, 2015;2016;.

[22] Conyers Herring and MH Nichols. Thermionic emission. *Reviews of Modern Physics*, 21(2):185, 1949.

[23] LA Harris. Analysis of materials by electron-excited auger electrons. *Journal of Applied Physics*, 39(3):1419–1427, 1968.

[24] Phil Willmott. *An introduction to synchrotron radiation: techniques and applications*. John Wiley, Chichester, West Sussex, UK, 1. aufl. edition, 2011.

[25] FR Elder, AM Gurewitsch, RV Langmuir, and HC Pollock. Radiation from electrons in a synchrotron. *Physical Review*, 71(11):829, 1947.

[26] Yuanbo Deng and Daping Chu. Coherence properties of different light sources and their effect on the image sharpness and speckle of holographic displays. *Scientific Reports*, 7(1):1–12, 2017.

[27] R. Lewis. Medical applications of synchrotron radiation x-rays. *Physics in Medicine and Biology*, 42(7):1213–1243, 1997.

[28] Raymond A. Serway, Clement J. Moses, and Curt A. Moyer. *Modern physics*. Thomson Brooks/Cole, Belmont, CA, 3rd edition, 2005.

[29] K. K. Sharma and Inc ebrary. *Optics: principles and applications*. Academic Press, Amsterdam;Boston;, 2006.

[30] C Kottler, Christian David, Franz Pfeiffer, and Oliver Bunk. A two-directional approach for grating based differential phase contrast imaging using hard x-rays. *Optics express*, 15:1175–81, 03 2007.

[31] Jack D Gaskill. *Linear systems, Fourier transforms, and optics*, volume 576. Wiley New York, 1978.

[32] Ronald Newbold Bracewell and Ronald N Bracewell. *The Fourier transform and its applications*, volume 31999. McGraw-Hill New York, 1986.

[33] Harold Thayer Davis. *Introduction to nonlinear differential and integral equations*. US Atomic Energy Commission, 1960.

[34] David Paganin. *Coherent X-ray optics*. Number 6. Oxford University Press on Demand, 2006.

[35] Malvin Carl Teich. *Fundamentals of photonics [electronic resource]*. Wiley, 1991.

[36] Orazio Svelto and David C Hanna. *Principles of lasers*, volume 1. Springer, 2010.

[37] K. S. Morgan, K. K. W. Siu, and D. M. Paganin. The projection approximation and edge contrast for x-ray propagation-based phase contrast imaging of a cylindrical edge. *Opt. Express*, 18(10):9865–9878, May 2010.

[38] John E Greivenkamp. *Field guide to geometrical optics*, volume 1. SPIE press Bellingham, WA, 2004.

[39] Michael Reed Teague. Deterministic phase retrieval: a green's function solution. *J. Opt. Soc. Am.*, 73(11):1434–1441, Nov 1983.

[40] Wilhelm Conrad Röntgen. On a new kind of rays. *Science*, 3(59):227–231, 1896.

[41] Marco Endrizzi. X-ray phase-contrast imaging. *Nuclear Inst. and Methods in Physics Research, A*, 878:88–98, 2018.

[42] Reginald William James. The optical principles of the diffraction of x-rays. 1954.

[43] Faiz M. Khan and Jr Gibbons, John P. *Khan's the physics of radiation therapy*. Lippincott Williams Wilkins/Wolters Kluwer, Philadelphia, PA, fifth edition, 2014.

[44] Ervin B Podgoršak et al. *Radiation physics for medical physicists*. Springer, 2006.

[45] TJ Davis, D Gao, TE Gureyev, AW Stevenson, and SW Wilkins. Phase-contrast imaging of weakly absorbing materials using hard x-rays. *Nature*, 373(6515):595, 1995.

[46] Paul C. Diemoz, Alberto Bravin, Anikó Sztrókay-Gaul, Marie Ruat, Susanne Grandl, Doris Mayr, Sigrid Auweter, Alberto Mittone, Emmanuel Brun, Cyril Ponchut, Maximilian F. Reiser, Paola Coan, and Alessandro Olivo. A method for high-energy, low-dose mammography using edge illumination x-ray phase-contrast imaging. *Physics in medicine and biology*, 61(24):8750–8761, 2016.

[47] C Streffer. The icrp 2007 recommendations. *Radiation protection dosimetry*, 127(1-4):2–7, 2007.

[48] Raymond A. Serway, John W. Jewett, Kate Wilson, and Wayne Rowlands. *Physics*. Cengage Learning, South Melbourne, Vic, 2nd edition, 2016.

[49] K. M. Pavlov, T. E. Gureyev, D. Paganin, Ya I. Nesterets, M. J. Morgan, and R. A. Lewis. Linear systems with slowly varying transfer functions and their application to x-ray phase-contrast imaging. *Journal of Physics D: Applied Physics*, 37(19):2746–2750, 2004.

[50] D. Paganin, S. C. Mayo, T. E. Gureyev, P. R. Miller, and S. W. Wilkins. Simultaneous phase and amplitude extraction from a single defocused image of a homogeneous object. *Journal of Microscopy*, 206(1):33–40, 2002.

[51] S. W. Wilkins, T. E. Gureyev, T. J. Davis, A. W. Stevenson, and D. Gao. Phase-contrast imaging of weakly absorbing materials using hard x-rays. *Nature*, 373(6515):595–598, 1995.

[52] Ya. I. Nesterets and S. W. Wilkins. Phase-contrast imaging using a scanning-double-grating configuration. *Opt. Express*, 16(8):5849–5867, Apr 2008.

[53] David M. Paganin and Daniele Pelliccia. Tutorials on x-ray phase contrast imaging: Some fundamentals and some conjectures on future developments. 2019.

[54] Hart M. Bonse U. An x-ray interferometer with long separated interfering beam paths (e). appl. phys. lett. 7, 99–100. 1965.

[55] Hosoya S. Ando M. An attempt at x-ray phase-contrast microscopy. in 6th int. on xray optics and microanalysis (eds g shinoda, k kohra, t ichinokawa), pp. 63–68. tokyo, japan: University of tokyo press. 1972.

[56] A. Momose. Demonstration of phase-contrast x-ray computed tomography using an x-ray interferometer. *Nuclear Inst. and Methods in Physics Research, A*, 352(3):622–628, 1995.

[57] Atsushi Momose. Phase-contrast x-ray imaging based on interferometry. *Journal of Synchrotron Radiation*, 9(3):136–142, 2002.

[58] A Olivo, SE Bohndiek, JA Griffiths, A Konstantinidis, and RD Speller. A non-free-space propagation x-ray phase contrast imaging method sensitive to phase effects in two directions simultaneously. *Applied Physics Letters*, 94(4):044108, 2009.

[59] P. C. Diemoz, C. K. Hagen, M. Endrizzi, M. Minuti, R. Bellazzini, L. Urbani, P. De Coppi, and A. Olivo. Single-shot x-ray phase-contrast computed tomography with nonmicrofocal laboratory sources. *Physical Review Applied*, 7(4), 2017.

[60] A Olivo, Fulvia Arfelli, Giovanni Cantatore, Renata Longo, RH Menk, S Pani, M Prest, P Poropat, Luigi Rigon, G Tromba, et al. An innovative digital imaging set-up allowing a low-dose approach to phase contrast applications in the medical field. *Medical physics*, 28(8):1610–1619, 2001.

[61] Paul C. Diémoz, Fabio A. Vittoria, Charlotte K. Hagen, Marco Endrizzi, Paola Coan, Alberto Bravin, Ulrich H. Wagner, Christoph Rau, Ian K. Robinson, and Alessandro Olivo. A single-image retrieval method for edge illumination x-ray phase-contrast imaging: Application and noise analysis. *Physica Medica*, 32(12):1759–1764, 2016.

[62] Alessandro Olivo, Konstantin Ignatyev, Peter RT Munro, and Robert D Speller. Noninterferometric phase-contrast images obtained with incoherent x-ray sources. *Applied optics*, 50(12):1765–1769, 2011.

[63] A Olivo and E Castelli. X-ray phase contrast imaging: From synchrotrons to conventional sources. *Rivista del nuovo cimento*, 37(9):467–508, 2014.

[64] PC Diemoz, CK Hagen, M Endrizzi, and A Olivo. Sensitivity of laboratory based implementations of edge illumination x-ray phase-contrast imaging. *Applied Physics Letters*, 103(24):244104, 2013.

[65] Sebastien Berujon and Eric Ziegler. Near-field speckle-scanning-based x-ray imaging. *Physical Review A*, 92(1), 2015.

[66] I. Zanette, T. Zhou, A. Burvall, U. Lundström, D. H. Larsson, M. Zdora, P. Thibault, F. Pfeiffer, H. M. Hertz, Biomedicinsk fysik och röntgenfysik, Skolan för teknikvetenskap (SCI), Tillämpad fysik, and KTH. Speckle-based x-ray phase-contrast and dark-field imaging with a laboratory source. *Physical review letters*, 112(25):253903, 2014.

[67] Franz Pfeiffer, Martin Bech, Oliver Bunk, Philipp Kraft, Eric F Eikenberry, Ch Brönnimann, Christian Grünzweig, and Christian David. Hard-x-ray dark-field imaging using a grating interferometer. *Nature materials*, 7(2):134, 2008.

[68] Yi Yang and Xiangyang Tang. Complex dark-field contrast and its retrieval in x-ray phase contrast imaging implemented with talbot interferometry. *Medical Physics*, 41(10):101914–n/a, 2014.

[69] Henry Fox Talbot. Lxxvi. facts relating to optical science. no. iv. *The London, Edinburgh, and Dublin Philosophical Magazine and Journal of Science*, 9(56):401–407, 1836.

[70] Franz Pfeiffer, Timm Weitkamp, Oliver Bunk, and Christian David. Phase retrieval and differential phase-contrast imaging with low-brilliance x-ray sources. *Nature physics*, 2(4):258, 2006.

[71] D. Chapman, W. Thomlinson, R. E. Johnston, D. Washburn, E. Pisano, N. Gmür, Z. Zhong, R. Menk, F. Arfelli, and D. Sayers. Diffraction enhanced x-ray imaging. *Physics in Medicine and Biology*, 42(11):2015–2025, 1997.

[72] PP Ewald. Introduction to the dynamical theory of x-ray diffraction. *Acta Crystallographica Section A: Crystal Physics, Diffraction, Theoretical and General Crystallography*, 25(1):103–108, 1969.

[73] Vito Mocella. Negative refraction in photonic crystals: thickness dependence and pendellösung phenomenon. *Optics express*, 13(5):1361, 2005.

[74] Luigi Rigon, Fulvia Arfelli, and Ralf-Hendrik Menk. Generalized diffraction enhanced imaging to retrieve absorption, refraction and scattering effects. *Journal of Physics D: Applied Physics*, 40(10):3077, 2007.

[75] VA Bushuev, VN Ingal, and EA Belyaevskaya. Dynamical theory of images generated by noncrystalline objects for the method of phase-dispersive introscopy. *Crystallography Reports*, 41(5):766–774, 1996.

[76] V. N. Ingal and E. A. Beliaevskaya. X-ray plane-wave topography observation of the phase contrast from a non-crystalline object. *Journal of Physics D: Applied Physics*, 28(11):2314–2317, 1995.

[77] Marcus J. Kitchen, David M. Paganin, Kentaro Uesugi, Beth J. Allison, Robert A. Lewis, Stuart B. Hooper, and Konstantin M. Pavlov. Phase contrast image segmentation using a laue analyser crystal. *Physics in Medicine and Biology*, 56(3):515–534, 2011.

[78] Wei Zhou, Keivan Majidi, and Jovan G Brankov. Analyzer-based phase-contrast imaging system using a micro focus x-ray source. *The Review of scientific instruments*, 85(8):085114, August 2014.

[79] Marcus J. Kitchen, David M. Paganin, Kentaro Uesugi, Beth J. Allison, Robert A. Lewis, Stuart B. Hooper, and Konstantin M. Pavlov. X-ray phase, absorption and scatter retrieval using two or more phase contrast images. *Optics express*, 18(19):19994, 2010.

[80] M. J. Kitchen, K. M. Pavlov, K. K. W. Siu, R. H. Menk, G. Tromba, and R. A. Lewis. Analyser-based phase contrast image reconstruction using geometrical optics. *Physics in Medicine and Biology*, 52(14):4171–4187, 2007.

[81] Miles N Wernick, Oliver Wirjadi, Dean Chapman, Zhong Zhong, Nikolas P Galatsanos, Yongyi Yang, Jovan G Brankov, Oral Oltulu, Mark A Anastasio, and Carol Muehleman. Multiple-image radiography. *Physics in Medicine and Biology*, 48(23):3875, 2003.

[82] Zhili Wang, Dalin Liu, Jin Zhang, Wanxia Huang, Qingxi Yuan, Kun Gao, and Zhao Wu. Absorption, refraction and scattering retrieval in x-ray analyzer-based imaging. *Journal of Synchrotron Radiation*, 25(4):1206–1213, 2018.

[83] E Pagot, P Cloetens, S Fiedler, A Bravin, P Coan, J Baruchel, J Härtwig, and W Thomlinson. A method to extract quantitative information in analyzer-based x-ray phase contrast imaging. *Applied physics letters*, 82(20):3421–3423, 2003.

[84] Cheng-Ying Chou, Mark A Anastasio, Jovan G Brankov, Miles N Wernick, Eric M Brey, Dean M Connor Jr, and Zhong Zhong. An extended diffraction-enhanced imaging method for implementing multiple-image radiography. *Physics in Medicine & Biology*, 52(7):1923, 2007.

[85] Huang Zhifeng, Kang Kejun, and Yang Yigang. Extraction methods of phase information for x-ray diffraction enhanced imaging. *Nuclear Inst. and Methods in Physics Research, A*, 579(1):218–222, 2007.

[86] Chunhong Hu, Lu Zhang, Hui Li, and Shuqian Luo. Comparison of refraction information extraction methods in diffraction enhanced imaging. *Opt. Express*, 16(21):16704–16710, Oct 2008.

[87] Paul C. Diemoz, Paola Coan, Christian Glaser, and Alberto Bravin. Absorption, refraction and scattering in analyzer-based imaging: comparison of different algorithms. *Optics express*, 18(4):3494, 2010.

[88] Oral Oltulu, Zhong Zhong, Moumen Hasnah, Miles N Wernick, and Dean Chapman. Extraction of extinction, refraction and absorption properties in diffraction enhanced imaging. *Journal of Physics D: Applied Physics*, 36(17):2152, 2003.

[89] Ya I Nesterets, Paola Coan, TE Gureyev, Alberto Bravin, P Cloetens, and SW Wilkins. On qualitative and quantitative analysis in analyser-based imaging. *Acta Crystallographica Section A: Foundations of Crystallography*, 62(4):296–308, 2006.

[90] Pekka Suortti, Jani Keyriläinen, and William Thomlinson. Analyser-based x-ray imaging for biomedical research. *Journal of Physics D: Applied Physics*, 46(49):494002, nov 2013.

[91] Boris W Batterman and Henderson Cole. Dynamical diffraction of x rays by perfect crystals. *Reviews of modern physics*, 36(3):681, 1964.

[92] Heikki Suhonen, Manuel Fernández, Alberto Bravin, Jani Keyriläinen, and Pekka Suortti. Refraction and scattering of x-rays in analyzer-based imaging. *Journal of Synchrotron Radiation*, 14(6):512–521, 2007.

[93] MM Hall, VG Veeraraghavan, Herman Rubin, and PG Winchell. The approximation of symmetric x-ray peaks by pearson type vii distributions. *Journal of Applied Crystallography*, 10(1):66–68, 1977.

[94] Spring 8 Synchrotron. Spring 8, 2019. `http://www.spring8.or.jp/wkg/BL20B2/instrument/lang-en/INS-0000000314/instrument_summary_viewl`.

[95] S. stepanov, "x-ray server: an online resource for simulations of x-ray diffraction and scattering". in: "advances in computational methods for x-ray and neutron optics", ed. m.sanches del rio; proceedings spie, v.5536, p.16-26, (2004).

[96] M.A. Beltran, D.M. Paganin, K. Uesugi, and M.J. Kitchen. 2d and 3d x-ray phase retrieval of multi-material objects using a single defocus distance. *Opt. Express*, 18(7):6423–6436, Mar 2010.

[97] M. S. Islam, R. A. Lewis, K. Uesugi, and M. J. Kitchen. A high precision recipe for correcting images distorted by a tapered fiber optic. *Journal of Instrumentation*, 5(9):P09008–P09008, 2010.

[98] Caroline A Schneider, Wayne S Rasband, and Kevin W Eliceiri. Nih image to imagej: 25 years of image analysis. *Nature methods*, 9(7):671–675, 2012. `https://imagej.nih.gov/ij/download.html`. Accessed 10 November 2018.

[99] Stephan Saalfeld and Pavel Tomancak. Automatic landmark correspondence detection for imagej. 05 2013.

[100] Johannes Schindelin, Ignacio Arganda-Carreras, Erwin Frise, Verena Kaynig, Mark Longair, Tobias Pietzsch, Stephan Preibisch, Curtis Rueden, Stephan Saalfeld, Benjamin Schmid, et al. Fiji: an open-source platform for biological-image analysis. *Nature methods*, 9(7):676–682, 2012.

[101] Simon Rutishauser. *X-ray grating interferometry for imaging and metrology*. PhD thesis, ETH Zurich, 2013.

[102] R. H. Menk, L. Rigon, and F. Arfelli. Diffraction-enhanced x-ray medical imaging at the elettra synchrotron light source. *Nuclear Inst. and Methods in Physics Research, A*, 548(1):213–220, 2005.

[103] Keivan Majidi, Jun Li, Carol Muehleman, and Jovan G Brankov. Noise and analyzer-crystal angular position analysis for analyzer-based phase-contrast imaging. *Physics in Medicine & Biology*, 59(8):1877, 2014.

[104] D. J. Vine, D. M. Paganin, K. M. Pavlov, J. Kräußlich, O. Wehrhan, I. Uschmann, and E. Förster. Analyzer-based phase contrast imaging and phase retrieval using a rotating anode x-ray source. *Applied Physics Letters*, 91(25):254110, 2007.

[105] Christopher Parham, Zhong Zhong, Dean M. Connor, L. D. Chapman, and Etta D. Pisano. Design and implementation of a compact low-dose diffraction enhanced medical imaging system. *Academic radiology*, 16(8):911, 2009.

[106] Carol Muehleman, Jun Li, Dean Connor, Christopher Parham, Etta Pisano, and Zhong Zhong. Diffraction-enhanced imaging of musculoskeletal tissues using a conventional x-ray tube. *Academic radiology*, 16(8):918, 2009.

[107] M. ENGELHARDT, C. KOTTLER, O. BUNK, C. DAVID, C. SCHROER, J. BAUMANN, M. SCHUSTER, and F. PFEIFFER. The fractional talbot effect in differential x-ray phase-contrast imaging for extended and polychromatic x-ray sources. *Journal of Microscopy*, 232(1):145–157, 2008.

[108] Aimin Yan, Xizeng Wu, and Hong Liu. Beam hardening correction in polychromatic x-ray grating interferometry. *Optics express*, 25(20):24690, 2017.

[109] J. Meiser, M. Willner, T. Schröter, A. Hofmann, J. Rieger, F. Koch, L. Birnbacher, M. Schüttler, D. Kunka, P. Meyer, A. Faisal, M. Amberger, T. Duttenhofer, T. Weber, A. Hipp, S. Ehn, M. Walter, J. Herzen, J. Schulz, F. Pfeiffer, and J. Mohr. Increasing the field of view in grating based x-ray phase contrast imaging using stitched gratings. *Journal of X-ray science and technology*, 24(3):379–388, 2016.

[110] Adrian Sarapata, Marian Willner, Marco Walter, Thomas Duttenhofer, Konradin Kaiser, Pascal Meyer, Christian Braun, Alexander Fingerle, Peter B. Noël, Franz Pfeiffer, and Julia Herzen. Quantitative imaging using high-energy x-ray phase-contrast ct with a 70 kvp polychromatic x-ray spectrum. *Opt. Express*, 23(1):523–535, Jan 2015.

[111] The University of Melbourne. Ts imaging, 2019. `http://ts-imaging.science.unimelb.edu.au/Services/Simple/ICUtilXdata.aspx` Accessed 20 November 2019.

Chapter 9

Appendix

Here we include and explain code I made during this thesis. The code used to perform phase retrieval was that I significantly adapted hence it is the only code mentioned. Most code I made was just to plot trends to try and explain odd behaviours in images. Begining with correcting for the ratio drift, which was done by calculating the ratio drift as the diffracted flat field divided by the transmitted field field. Then applying the correction when calculating theta final as this is calculated using the ratio.
$flat_ratio = ID/IT$
...
$ThetaF = (IT*c/ID)*(1/(mean(flat_ratio(20:25, 750:760))/(mean(ID(20:25, 750:760))/mean(IT(20:25, 750:760)))))$
Later on in the same code we correct for the shifting and wobble effect . The shifitng is calculated by finding reversing and finding the side pixel location where the largest negative phase gradient occurs. Then shifitng the image by this difference divided by 2 munis the phantom length divided by 2. This is done for both $\Delta\theta$ maps individually. The wobble is corrected for by finding the coordinates along the side of the phantom along 20 pairs of horizontal lines. We use these line pairs to calculate the angle of rotation individually and then take the mean.
DeltaThetads = Reverse(DeltaThetad,1)
irrelevant7=min((DeltaThetad[*,400]),Lminds)
irrelevant8=max((DeltaThetad[*,400]),Lmaxs)
phantlength = Lmaxs - Lminds
irrelevant7=min((DeltaThetads[*,400]),Lminds)
irrelevant8=min((DeltaThetad[*,400]),Lmaxs)
diff = Round((Lminds-Lmaxs)/2)-phantlength/2;-550
DeltaThetad = shift(DeltaThetad,diff)
DeltaThetads = Reverse(DeltaTheta,1) irrelevant7=min((DeltaTheta[*,400]),Lminds)

```
irrelevant8=max((DeltaTheta[*,400]),Lmaxs)
phantlength = Lmaxs - Lminds
irrelevant7=min((DeltaThetads[*,400]),Lminds)
irrelevant8=min((DeltaTheta[*,400]),Lmaxs)
diff = Round((Lminds-Lmaxs)/2)-phantlength/2;-550v DeltaTheta = shift(DeltaTheta,diff)
;;;;;;;;;;;;;;;;;;;;; testsubject= congrid(Deltatheta,11000,7710,/INTERP)
topp = 2400;1800
botp =6400
irrelevant6=min(testsubject[0:2420,topp],Lmind1)
irrelevant5=min(testsubject[0:2420,botp],Lmind2)
;print, lmind1,lmind2
;stop
height = botp - topp
width = Lmind1-Lmind2
phis2 = []
for nn = 1,20 do begin
irr2 = min(testsubject[0:2420,topp-nn*11],Lmindd1)
irr3 = min(testsubject[0:2420,botp-nn*11],Lmindd2)
irr3 = min(testsubject[0:2420,topp+nn*11],Lmindd3)
irr4 = min(testsubject[0:2420,botp+nn*11],Lmindd4)
corphi1 = Deg(Atan(lmindd1-lmindd2,(botp-nn*11)-(topp-nn*11)))
corphi2 = Deg(Atan(lmindd3-lmindd4,(botp+nn*11)-(topp+nn*11)))
phis2 = append(phis2,[corphi1,corphi2])
endfor
phicorr = Deg(Atan(width,height))
phis2 = append(phis2,phicorr)
phis = phis2
meanphi = mean(phis2)
phicorr = meanphi
print, 'rotation', phicorr
DeltaTheta = Rot(DeltaTheta,phicorr)
DeltaThetad = Rot(DeltaThetad,phicorr)
DELVAR, testsubject
```

We then subtract the background from the two $\Delta\theta$ images before calculating the directional phase gradients g_x and g_y. We then call a function called 'fourierintegration' that integrates the directional phase gradients into a phase map. This phase map is then multiplied by the two times the wavenumber.

$DeltaTheta- = mean(DeltaTheta[10:40, 420]); 100:120, 100:120])$
$DeltaThetad- = mean(DeltaThetad[10:40, 420]); 100:120, 100:120])$

$gx = (DeltaTheta + DeltaThetad)/(2 * cos(deg(8)))$
$gy = (DeltaTheta - DeltaThetad)/(2 * sin(deg(8)))$
$Thetap = -fourierintegration(gy, gx); xgradientname = Filenamey, ygradientname = Filenamex)$
$; Thetap = fourierintegration(gx, gy)$
$wl = wavelength(26.)$
$k = 2.*!dpi/wl; m^(- 1)$
$phase = Thetap$
$phase* = 2 * k$

This part corrects for the horziontal linear trend in the phase map by fitting a linear slope between the vertical edges of the phantom and is repeated for every horizontal line going down the phase map.

```
dims = size(phase,/DIMENSIONS)
for abc = 0, Dims[1]-1 do begin
linxx = findgen(Dims[0])
hope1 = linfit([0,Dims[0]-1],[phase(0,abc),phase(Dims[0]-1,abc)])
line1 = hope1[0]+ hope1[1]*linxx
phase[*,abc]*=reverse(line1/min(line1))
minp = phase[0,abc]
phase[*,abc]-=minp
endfor
```